TELESCOPE ARRAY
TECHNICAL DESIGN REPORT

January 17, 2000

Contents

Chapter 1

Physics

1.1 Introduction

This proposal describes the Telescope Array project which will make a major advance in the study of the highest energy cosmic rays, γ-rays and neutrinos. The Telescope Array will explore the high energy phenomena in the universe, the acceleration of high energy particles, non-thermal processes, and search for the relics of the Hot Big Bang. At present, we know that cosmic ray particles with extraordinary energies, 30J to 50J exist [1, 2, 3, 4]. These are macroscopic energies and this is the highest energy radiation in the universe so far experimentally studied by human beings. An efficient particle accelerator or particle factory in the universe is required as a source of these particles. These studies are strongly related not only to astrophysics, but also to elementally particle physics and cosmology.

The study of cosmic ray origins began with the initial discovery by Hess in 1912. The existence of natural radiation was known before this, but he showed that it comes from the sky. After the discovery, extensive efforts for the measurement of cosmic rays have been carried out with various methods. In particular, the discovery of the air shower phenomena (cascade showers which reach the ground, induced by very energetic cosmic rays) by P. Auger was very important. At present, we know their energy extends over more than 13 decades from 10^7 eV up to 10^{20} eV. Since the initial discovery, the study of their origin has been a most important issue. Their energy density in our Galaxy is ~ 1 eV/cm^3, which is comparable with energy densities of the photon field and magnetic field in our Galaxy. Ginzburg and Syrovatskii (1964) suggested Super Novas as the origin of galactic cosmic rays. At the present time, many observations, including the chemical abundance of cosmic rays and gamma ray observations, appear to support this hypothesis. The production of cosmic rays below 10^{15} eV is likely to be explained with the first order Fermi shock acceleration at supernova remnants.

At present, the most interesting topic in the cosmic ray physics is the study of the highest energy cosmic rays. Experimental data accumulated so far show increasing inconsistency with the conventional models for cosmic ray origin based on acceleration of charged particles. We expect to see an end of the high energy cosmic ray spectrum at 6×10^{19} eV, due to the resonance production of hadrons with the cosmic microwave background radiation (CMBR), what is called the Greisen-Zatsepin-Kuzmin (GZK) cutoff [5]. Most striking, however, is the clear evidence for the extension of the cosmic ray energy spectrum above

the GZK cutoff discovered by AGASA and the Fly's Eye experiment, and recently confirmed by preliminary data from HiRes. Furthermore, the propagation length of cosmic ray particles above the GZK cutoff energy is limited to within 50 Mpc from our Galaxy. The magnetic field of the Galaxy and of inter-galactic space is not strong enough to bend the trajectory of these particles more than a few degrees. Sources for particles with energies above the GZK cutoff energy should thus be relatively close by and particles will point back to these sources. However, no possible astrophysical sources (accelerators) at the arrival direction of these particles within 50 Mpc of the Earth were found.

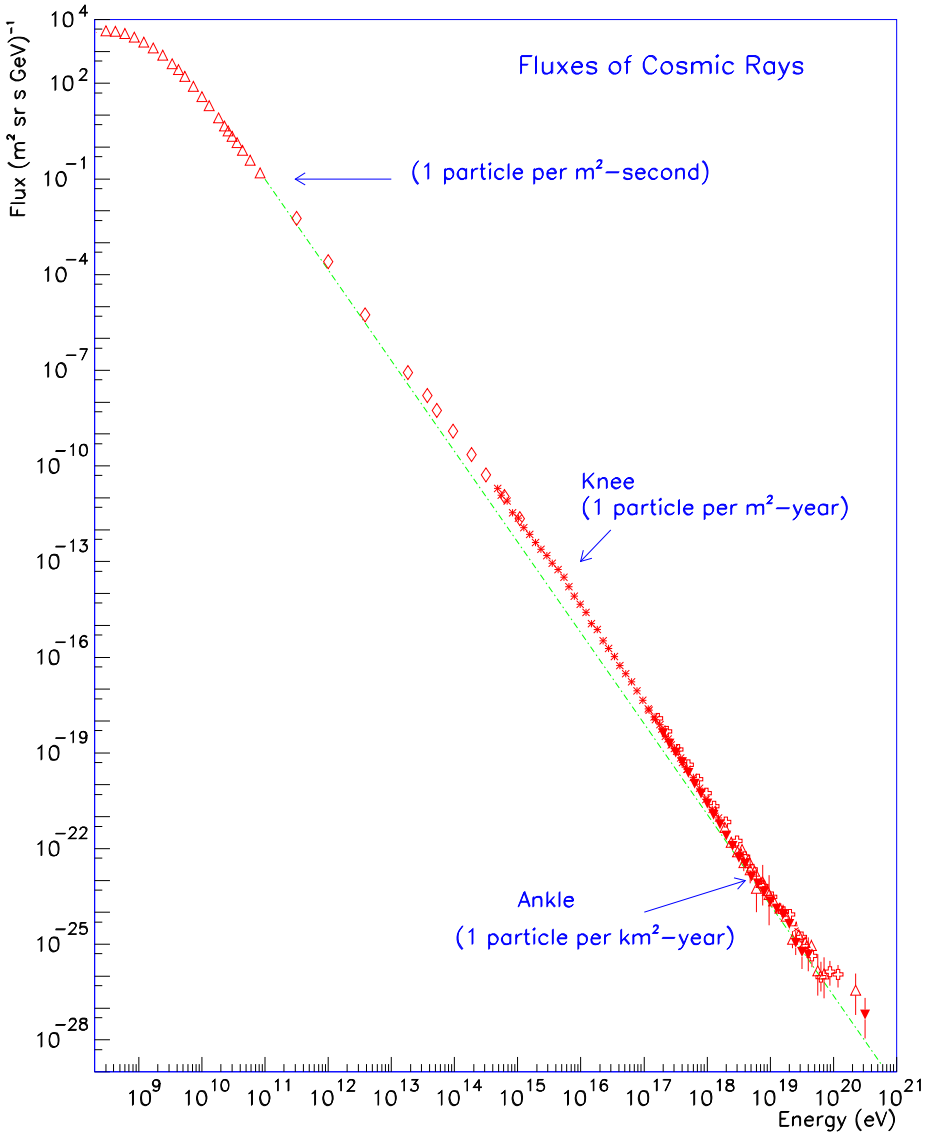

FIG. 1.1: The energy spectrum of cosmic ray [6].

1.2 Experimental Status

In Fig. 1.1, we show the cosmic ray energy spectrum over a very wide energy range. The spectrum can be roughly represented by a single power law with exponent of -2.8. However, we can see small kinks at 10^{16} eV (knee) and 10^{19} eV (ankle).

At the knee, the galactic cosmic ray leakage from our Galaxy may increase and the energy dependence of the cosmic ray life time becomes stronger. The Larmor radius of particles with 10^{16} eV in our Galaxy is expected to be $\sim 3(1/Z)$ pc for the particle with charge Z. The scale ~ 1 pc corresponds to the typical size of a magnetic field turbulence in the disk of our Galaxy. We also expect the maximum acceleration energy in a Super Nova Remnant to be $\sim 10^{14} \times Z$ eV [7]. Detailed studies of the knee region of the spectrum were carried out. So far, however, there are many possible interpretations of the knee, including leakage from the galactic disk, energy limits of the acceleration mechanism, or new additional components (this model interprets the knee as an additional bump). In all cases, we can say these cosmic rays must originate in our Galaxy.

The ankle is interpreted as the cross over energy from a galactic cosmic ray spectrum to an extragalactic one. The Larmor radius of cosmic rays in our Galaxy is calculated to be ~ 3 kpc $(E/10^{19}$ eV$)(1/Z)$, thus these cosmic rays propagate more freely than at lower energy. The deflection angle in the propagation of these particles is less than a radian. Therefore, if we assume galactic sources, we expect very strong cosmic ray anisotropy (the anisotropy amplitude could be $\sim 100\%$). However, the small measured anisotropy above ankle (only upper limits are obtained from experiments) naturally requires an extra galactic component. The depth of the shower maximum in the atmosphere (X_{max}) is sensitive to the chemical composition. The X_{max} study by Fly's Eye suggests a gradual change of chemical composition from heavy components to light components around $10^{18.5}$ eV [8]. If this is true, it is a strong evidence for the cross over from a galactic component to an extragalactic one.

1.2.1 Cosmic Rays above GZK energy

Figure 1.2 shows the energy spectrum above $10^{18.5}$ eV observed by AGASA experiment [4]. For reference, we have superposed the expected GZK energy spectrum assuming the uniform source distribution in the Universe. Eight events are observed above 10^{20} eV. The energy of giant air showers observed by AGASA is estimated by the particle density $S(600)$ at a distance of 600m from the shower axis. This is known to be a good energy estimator [9]. The conversion factor from S(600) [m^{-2}] to primary energy E_0 [eV] is derived from simulation [10] to be

$$E_0 = 2.0 \times 10^{17} \times S(600)^{1.0}.$$

In Fig. 1.3, the Fly's Eye stereo spectrum is shown [8]. There is no events above 10^{20} eV because the aperture for stereo data is too small. The result is statistically consistent with AGASA if we consider the exposure differences. The kink (ankle) at $10^{18.5}$ eV is seen clearly. In the stereo observation, the shower geometry is obtained as an intersection of two detector-shower planes. The energy is estimated by two eyes. The energy resolution is obtained experimentally to be 20%. The position of the ankle is slightly lower than AGASA. The cosmic ray intensity is lower than AGASA by factor of 1.4. These effects

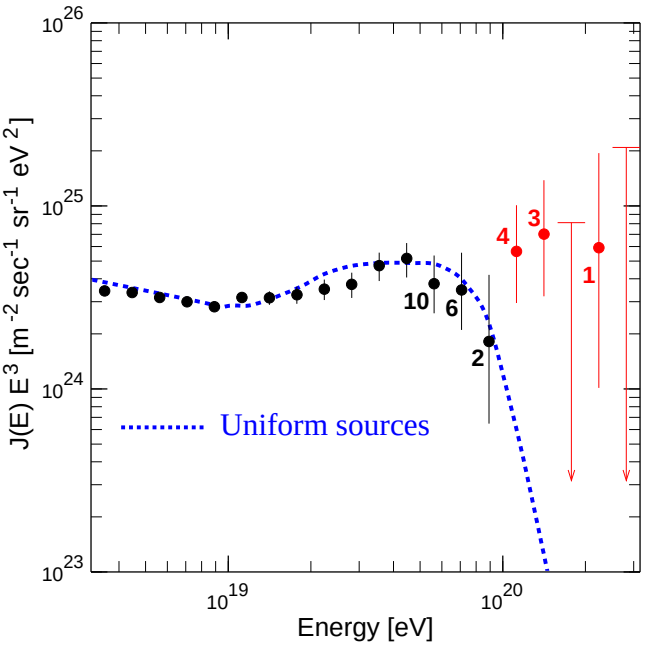

FIG. 1.2: The energy spectrum observed by AGASA. The vertical axis is multiplied by E^3. Error bars represent the Poisson upper and lower limits at 68% and arrows are 90% C.L. upper limits. Numbers attached to points show the number of events in each energy bin. The dashed curve represents the spectrum expected for extragalactic sources distributed uniformly in the Universe, taking account of the energy determination error. The primary spectrum is assumed $\propto E^{-2.3}$.

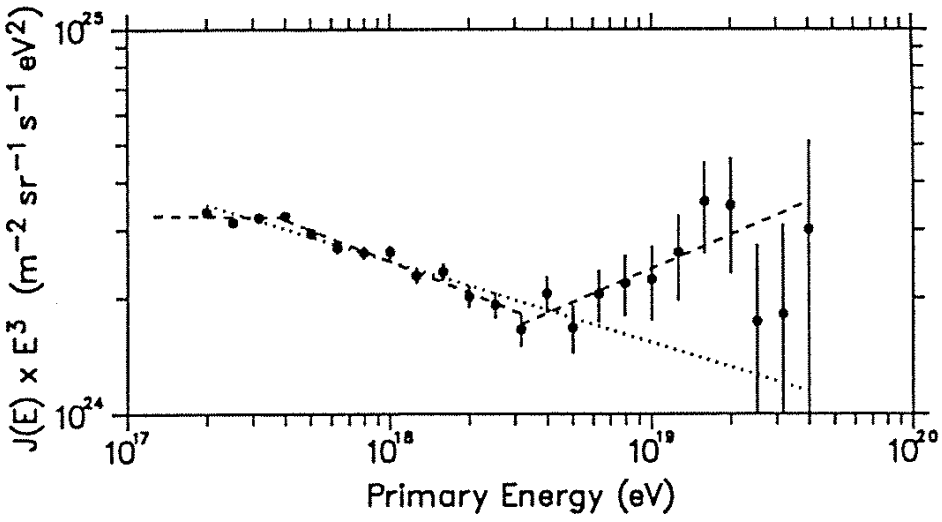

FIG. 1.3: The cosmic ray energy spectrum obtained by Fly's Eye stereo observation. The number of events above 10^{19} eV is 60. The exposure is about 1/5 of AGASA. The lack of events above 10^{20} eV is consistent with AGASA result, if we take the exposure into account. The clear kink (ankle) is seen around $10^{18.5}$ eV.

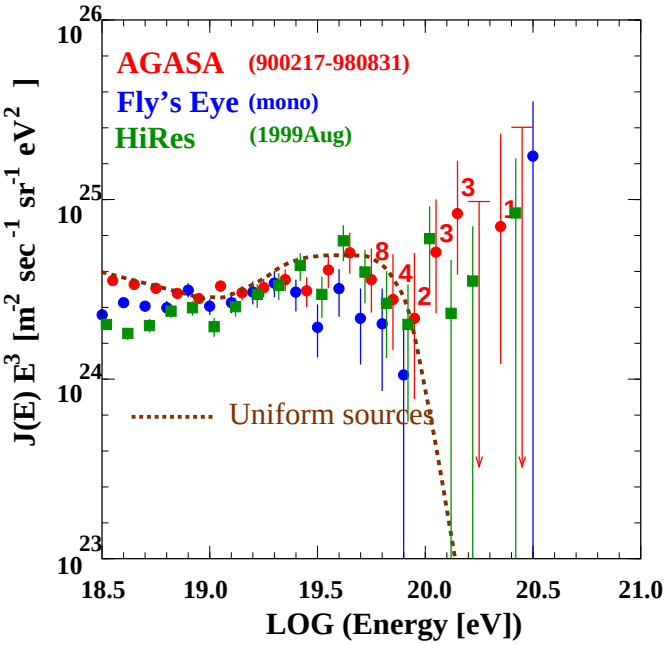

FIG. 1.4: The energy spectrum obtained by AGASA, original Fly's Eye and HiRes monocular observation (preliminary). Three data are consistent each other.

can be explained by the difference in energy resolution and systematics. For example, if we reduce the AGASA energy by 15 % or increase the FE stereo energy by 15 %, we obtain much better agreement between two experiments.

In Fig. 1.4, we have shown the energy spectra obtained by AGASA, Fly's Eye monocular experiment and HiRes monocular experiment(preliminary). The HiRes data has a similar aperture to AGASA. The three data sets are consistent each other within statistical errors above 10^{19} eV. Differences below 10^{19} eV reflect the different energy resolution and energy scale systematics between the three experiments. Differences in energy scale were magnified in this plot by E^3 weighting. In total, we have observed 16 events above 10^{20} eV. The number of events, one from monocular Fly's Eye, seven from HiRes and eight from AGASA are consistent, if we take into account the exposure of each experiment. The energy spectrum clearly extends beyond 10^{20} eV with no GZK cutoff. It is not clear with present statistics whether there is any structure in the spectrum (for example, a small valley at 10^{20} eV).

The arrival direction distribution of the highest energy cosmic rays above 4×10^{19} eV is shown in Fig. 1.5 in the equatorial coordinates [11]. Small dots and squares show events between 4×10^{19} eV and 10^{20} eV and above 10^{20} eV, respectively. The events above 10^{20} eV corresponds to the pure super-GZK particles, and if they are hadrons their sources should be closer to the Earth than 50 Mpc. The energy 4×10^{19} eV is the lower threshold energy of the expected pile produced by the GZK effect up. Events above this energy may still come from the same sources as the super-GZK events. Their energies have been decreased by inelastic interactions. If we assume an $E^{-2.3}$ source energy spectrum, we expect 50 % or more of these event to originally have energies above the GZK cutoff. They appear to be distributed uniformly over the observable sky. We have carried out several tests for anisotropy but

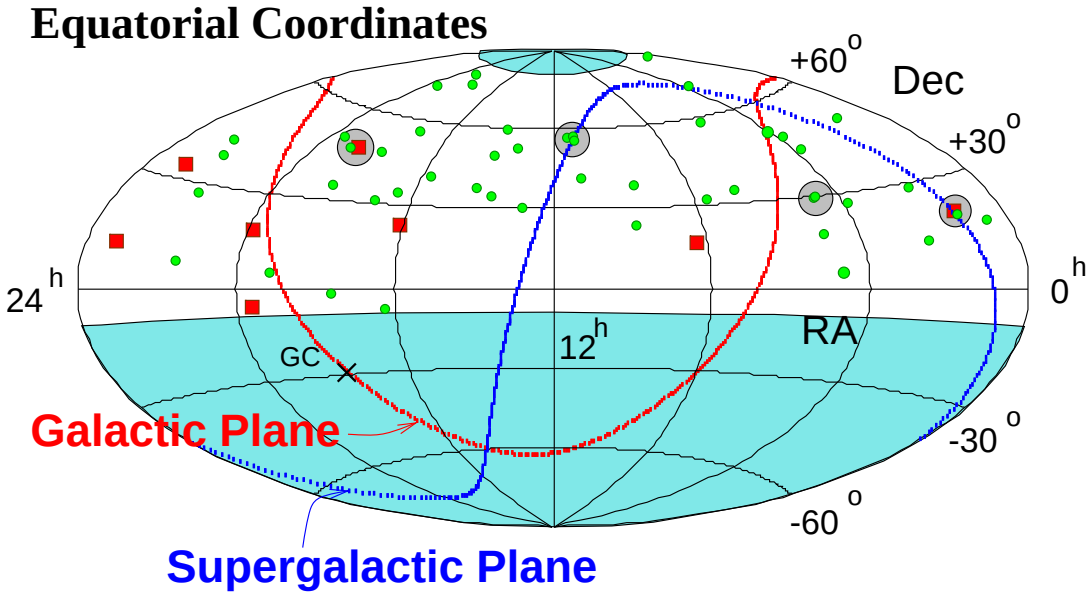

FIG. 1.5: The arrival direction of the highest energy cosmic rays on the equatorial coordinates observed by AGASA.

could not find any large scale structures in this distribution. However, we found one triplet and three doublets of events clustering within an angular resolution (2.5° circle) as indicated shadowed circles. The chance probability for this clustering effect was evaluated by Monte Carlo simulation and found to be $P_{ch} = 0.0032$. No outstanding astronomical objects have been found in the directions of these clusters, although an interacting galaxy called VV141 was found to lie in the direction of the triplet at 100 Mpc away.

1.2.2 Cosmic Rays around 10^{18} eV

In order to explore the origin of galactic cosmic rays, a harmonic analysis in Right Ascension was carried out using about 216,000 events observed by AGASA [12]. This is a reliable method to search for global anisotropy of the cosmic-ray arrival direction distribution. The amplitude, the phase (peak direction in Right Ascension), and the Rayleigh power k were determined in each differential energy bin as shown in Table 1.1. A Rayleigh power $k \sim 14$ was found at energy bin E5. This is surprisingly high, corresponding to a chance probability of 2.5×10^{-6}.

Table 1.1: The first harmonic analysis in Right Ascension.

Bin	Energy Range [EeV]	#	Amplitude [%]	Phase [°]	k	P_{prob}
E4	1/2 – 1.0	56658	0.5	272	0.42	0.65
E5	1.0 – 2.0	29207	4.2	297	12.9	2.5×10^{-6}
E6	2.0 – 4.0	10129	2.0	256	1.10	0.33
E7	4.0 – 8.0	2769	3.3	256	0.76	0.46

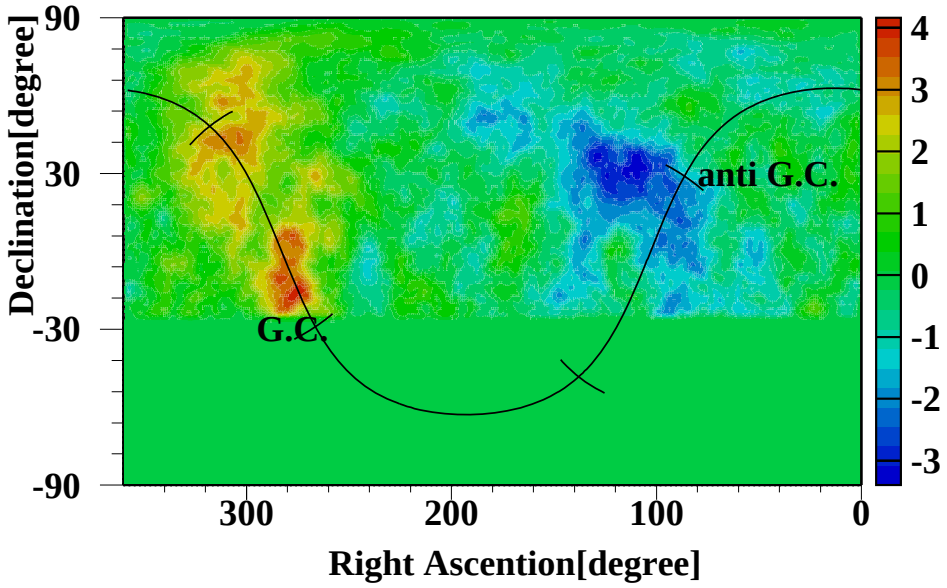

FIG. 1.6: The statistical significance of the deviations of the arrival direction distribution of the cosmic rays above 10^{18} eV on the equatorial coordinates (obtained by AGASA) [12].

In Fig. 1.6 the arrival direction distribution in the equatorial coordinates obtained by AGASA is shown. The figure shows the statistical significance of the deviations from isotropic expectation. Here, the energy region of 10^{18} eV $\sim 10^{18.4}$ eV is selected which corresponds to the maximum Rayleigh power k-value. Note that we cannot observe events with declination less than $-25°$, as long as we use showers with zenith angles less than $60°$. In this figure, we have chosen a circle of $20°$ radius to evaluate the excess. In the significance map, a 4.5 σ excess (obs./exp. = 506/413.6) near the Galactic Center region can be seen. In contrast, near the direction of anti-Galactic Center we can see a deficit in the cosmic ray intensity (-4.0σ). An event excess from the direction of the Cygnus region is also seen with 3.9σ (obs./exp. = 3401/3148). This anisotropy can be considered as clear evidence for the existence of galactic cosmic rays up to 10^{18} eV. Similar, though less statistically compelling results have recently been published by the Fly's Eye experiment. They show a 3 σ enhancement from the galactic plane in an energy bin near 10^{18} eV.

1.2.3 Chemical composition

Figure 1.7 shows the X_{max} distribution measured by the Fly's Eye experiment [8]. Recently, this result has been confirmed by the HiRes prototype and CASA, MIA hybrid experiments [13]. An unusually large elongation rate (energy dependence of X_{max}) is found. One expect 60 g/cm^2 increase per decade of energy from Monte Carlo simulation if one has an unchanging hadronic composition. However, the Fly's Eye experiment observed 80 g/cm^2 per decade between 10^{17} eV and 10^{19} eV. This can be interpreted as being due to a change in chemical composition from heavier to lighter. In the AGASA experiment, the muon component is measured by shielded detectors. Looking at the correlation of $\rho_\mu(600)$ and

$S(600)$, no significant evidence for a rapid composition change was found [14]. However, an analysis of both experiments using a the same hadronic model (Sybill) by B.Dawson and R.Meyhandan [15], suggests that a gradual chemical composition change from heavier to lighter between 10^{16} eV and 10^{19} eV is compatible with both experimental results.

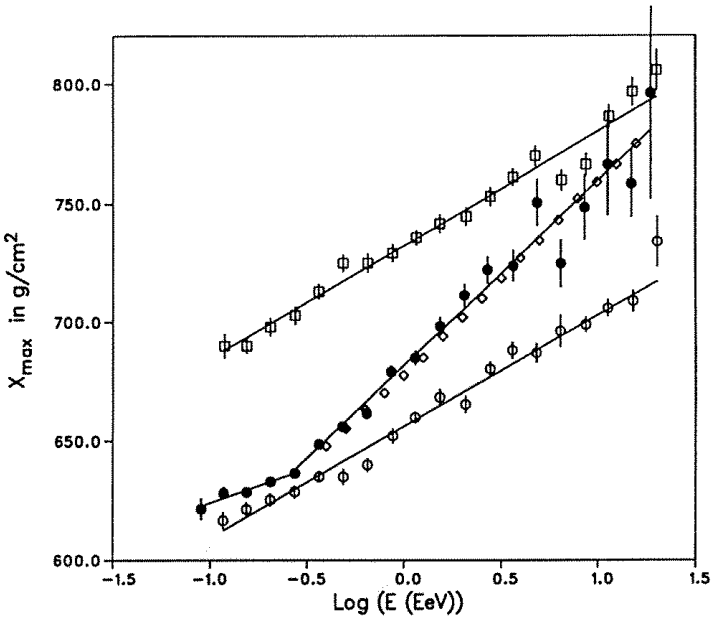

FIG. 1.7: The average X_{max} as a function of primary energy obtained by Fly's Eye. Two upper and lower lines correspond to pure proton and pure iron primaries. The energy dependence of X_{max} can be interpreted as a change in the chemical composition from heavier to lighter between 10^{17} eV and 10^{19} eV.

1.3 Physics of Extremely High Energy Cosmic Rays

The interesting features of the highest energy cosmic ray study can be summarized as follows.

- Astrophysical sources of the highest energy cosmic rays are limited. Only GRBs(Gamma Ray bursts), AGNs (Active Galactic Nucleuses), Colliding galaxies and Radio galaxy lobes are possible sources. However, AGNs and Radio galaxy lobes within 50 Mpc are almost ruled out by recent observations of super-GZK events since they do not point back to any such object.

- The propagation length of super-GZK particles is limited due to the interaction with CMBR. About 50 Mpc is a limiting value for the radius of the GZK horizon.

– The bending of protons due to the magnetic field in our Galaxy and inter galactic space should be small. There is thus the possibility to open the new astronomical window on the universe using hadronic particles above the GZK energy.

– Fundamental science. Cosmic rays with 10^{20} eV energy are the highest energy radiation so far observed. The current energy scale, 10^{20} eV, is beginning to approach the GUT scale energy 10^{24}–10^{25} eV. The observation of the highest energy cosmic rays may be of significant importance to elementally particle physics and cosmology.

1.3.1 Astrophysical sources of the highest energy cosmic ray

In Fig. 1.8, the possible cosmic ray sources are plotted on an object size versus magnetic field strength map [16]. In the Fermi acceleration or one shot acceleration models, we always meet with the minimum condition for the attainable maximum energy: $R_g < R_{obj}/2$, i.e., the Gyro radius of accelerated particle should be smaller than the object size. Since

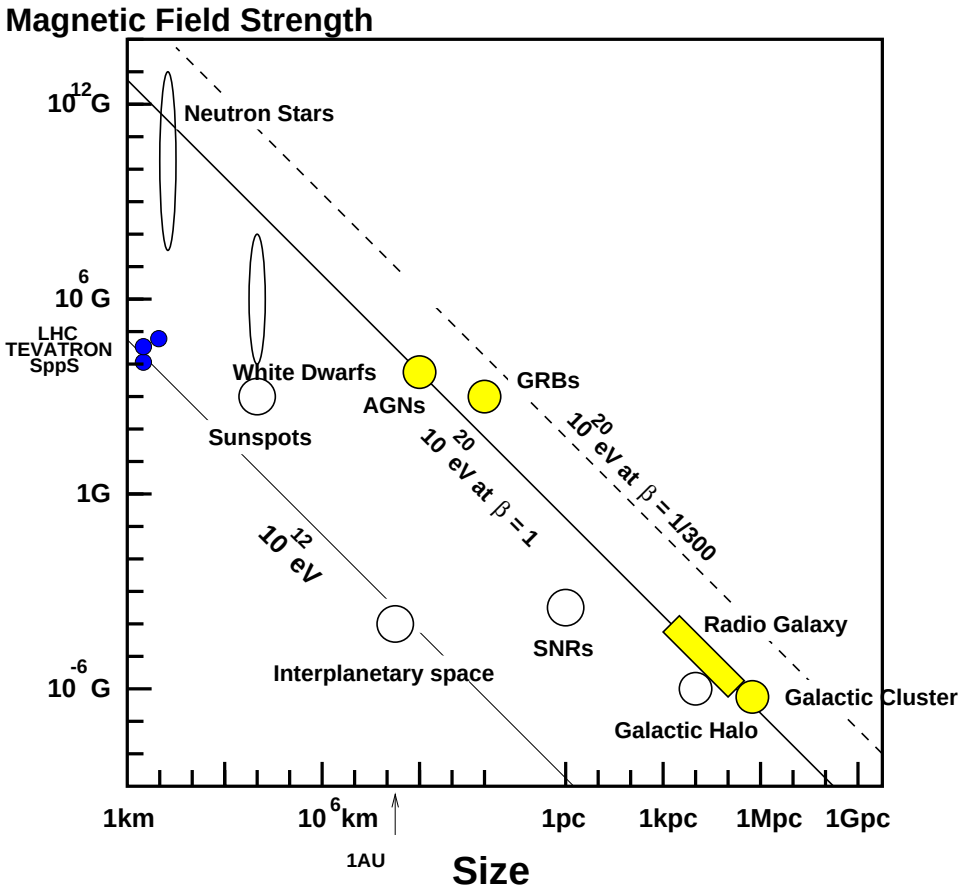

FIG. 1.8: The astronomical objects as cosmic ray sources. They are plotted on size and magnetic field strength map. The minimum requirement for the sources, Larmor radius should be smaller than accelerator size, is shown by the line. The most promising source for the highest energy cosmic ray is GRBs.

gyro radius is proportional to the particle momentum, this equation give us the maximum acceleration energy for each object. At the same time, we need to consider the cooling or energy loss process of cosmic ray particles in these objects, for example, synchrotron radiation, and photo-pion production. In compact sources (or in the strong magnetic field case), synchrotron radiation becomes important, because the energy loss rate is proportional to B^2. On the other hand, in large acceleration systems ($\geq$ Mpc), the acceleration time becomes relatively larger and we need to consider photo-pion production process with CMBR. Using these arguments, we can discard neutron stars (extremely high B condition), and galactic clusters (photo-pion cooling becomes dominant) as candidates for sources of the highest energy cosmic rays.

The GRBs, AGNs, and radio galaxy lobes alone remain as source candidates. Most promising are the GRBs, because AGNs and radio galaxy lobes are just on the acceleration boundary and no such candidates have been identified with the recent observation of super-GZK events. GRBs on the other hand, can solve this problem. There is a constraint on GRB models from the arrival direction distribution of super-GZK particles. The GRB rate in our Universe is estimated ~ 2/day from BATSE gamma ray detector observations. This value can be rewritten as 0.0013–0.0026/(100 Mpc)^3 yr. The typical propagation delay of charged cosmic ray with respect to light is 100–1000 yrs (this will be explained later) due to the scattering by the magnetic field in the inter-galactic space. Therefore, we will see the GRBs occurred in the last 100–1000 yrs within the GZK horizon (50–100 Mpc). The number of GRBs contributing to the cosmic ray flux is thus estimated to be at most, $5 \sim 10$ in this space-time volume and we expect only several independent GRBs (arrival direction) for cosmic rays. At present about 20 super-GZK events are recorded, and we see no clusters in their arrival direction distribution. This gives a constraint on GRBs source model. However, if we consider the beaming effect in the GRB fireball model, this problem may be resolved since we can increase the number of independent GRBs in the GZK horizon.

As mentioned above, we have constraints on the conventional astronomical source ("Bottom-up") models from observations. "Top-down" models can evade many of these constraints. They explain the super-GZK particles as decay products from heavy relics such as, monopole annihilation (monopolonium collapse), cosmic string decay, decay of necklaces, etc. In any such models, we expect a hard energy spectrum and gamma ray dominant chemical compositions. These scenarios can solve the current problem. They exhibit no GZK effect, uniform arrival direction distribution of super-GZK particles, and no identification of an astronomical counter part. The big bonus from these scenarios is the presence of a large neutrino flux. These models will be discussed in detail in the following sections.

1.3.2 Interaction with CMBR

An important feature of the highest energy cosmic rays is their interaction with CMBR [5]. In Fig. 1.9, we show the energy spectrum modified by the interaction with CMBR [17]. The left figure shows the spectrum expected from a one-source model. Several lines correspond to different propagation lengths. If one bright source dominates in the cosmic rays observed at the Earth, we expect such spectra. The right figure shows the expectation from a uniform source model, each line corresponds to the different evolution parameters

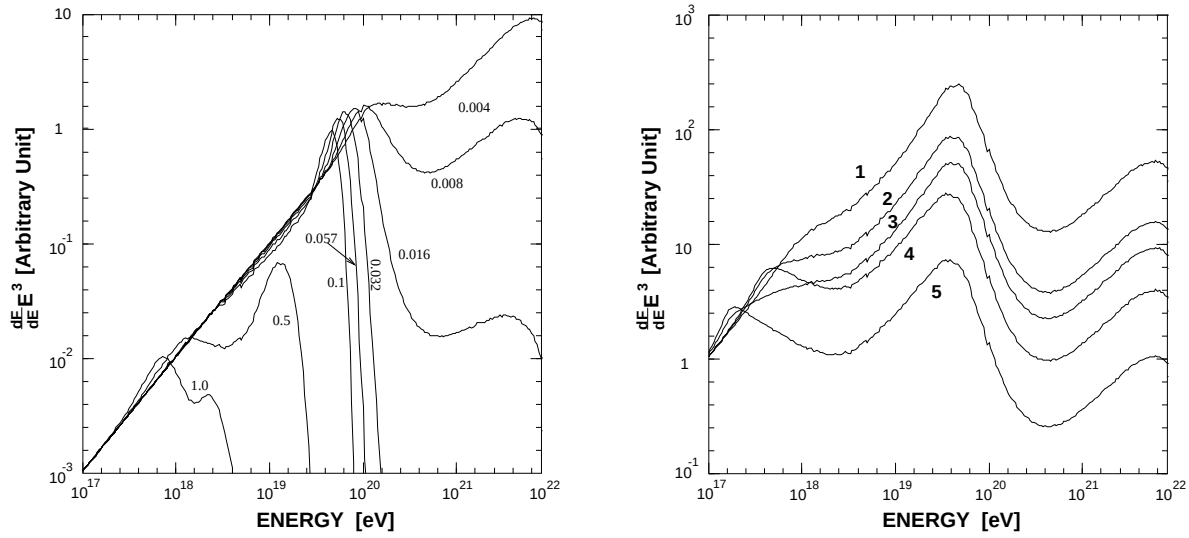

FIG. 1.9: The energy spectrum modification by the interaction with CMBR. The left figure shows the spectrum expected from one source model. Several lines correspond to different propagation lengths. The right figure shows the expectation from the uniform source model, each line corresponds to the different evolution parameter.

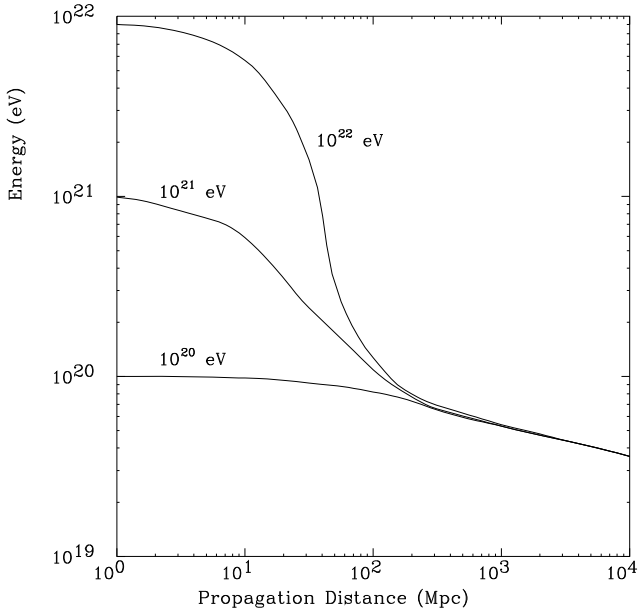

FIG. 1.10: The history of the energy of cosmic ray particle traveling the CMBR sea. It is worthy to note that the particle observed at the Earth with super-GZK energy has greater energy at the source. For example, if we observe cosmic rays of 3×10^{20} eV from the source with distance of 30 Mpc, it should have 10^{21} eV at the source.

of cosmic ray production. Except for a nearby one source model, in both cases, we expect a clear GZK cutoff below 10^{20} eV.

The evolution of the energy of a cosmic ray as it travels through the CMBR is shown in Fig. 1.10. This plot shows that the original cosmic ray energy at the source should be higher than that observed at the Earth, especially for the particles above 10^{20} eV. For example, 2×10^{20} eV or 3×10^{20} eV corresponds $\sim 10^{21}$ eV at the source, if we assume the propagation length of 30 Mpc. Of course, this evaluation depends on the source distance, and we require that the accelerator has a large enough E_{max} (maximum attainable energy).

1.3.3 Magnetic field

Another important feature of cosmic ray propagation is their interaction with the magnetic field in our Galaxy and inter-galactic space. Generally the knowledge for magnetic field is limited, especially in the inter-galactic space. The galactic magnetic field can be measured by the Faraday Rotation Measure of linearly polarized radio signals and by the Dispersion Measure of pulsar signals. The strength of magnetic field in the disk is estimated to be 2μG. The scale height of magnetic field strength of our Galaxy is obtained to be 1.0–1.4 kpc by recent observations [18, 19, 20]. Recently the magnetic field inside local clusters of galaxies is measured and their strengths are found to be a few μG [21, 22]. In the void region, only the upper limit for the magnetic field strength, 10^{-9} G is obtained so far.

Figure 1.11 shows the cosmic ray propagation in our Galaxy. In this calculation, an anti-proton is ejected from the Earth. At 10^{18} eV, the cosmic ray particles couple with magnetic field strongly. However, at higher energy, they travel more freely and the trajectories become linear.

Figure 1.12, left panel, shows the deflection angles of cosmic rays in the inter-galactic space and in the Galaxy, as a function of energy. The time delay relative to propagation time for light is shown in the right panel. Here, we assumed the magnetic field strength of 1 nG and the coherent scale of 1 Mpc in the inter-galactic space. Typical time delay for super-GZK particles is 100–1000 years in 30 Mpc propagation. Therefore, even if GRBs are sources of super-GZK particles, we may not see any clear temporal correlation between the GRBs and super-GZK particles with limited observation time.

With the knowledge of the propagation, we can discuss the GRBs model in more detail. Figure 1.13 shows the cosmic ray energy spectrum expected from GRBs source model [23]. Since the time delay is energy dependent, higher energy particles arrive earlier and thus we observe cosmic rays with limited energy range at a certain time. Older GRBs contribute in lower energy region, and closer GRBs contribute as larger flux. If we assume stronger magnetic field, we expect wider energy spectrum for each GRBs.

1.3.4 Beyond the Standard Model

Many conventional models, based on the acceleration of charged particles by the shock waves in magnetic fields, were developed. These include AGNs [24], hot-spots of type II radio galaxies [25, 26], colliding galaxies [27, 28], pulsars [29], supermassive blackholes [30], galactic wind termination shocks [31], gamma ray bursts [23, 32], and etc. However, there are serious problems for these models, insufficient acceleration, and significant energy losses

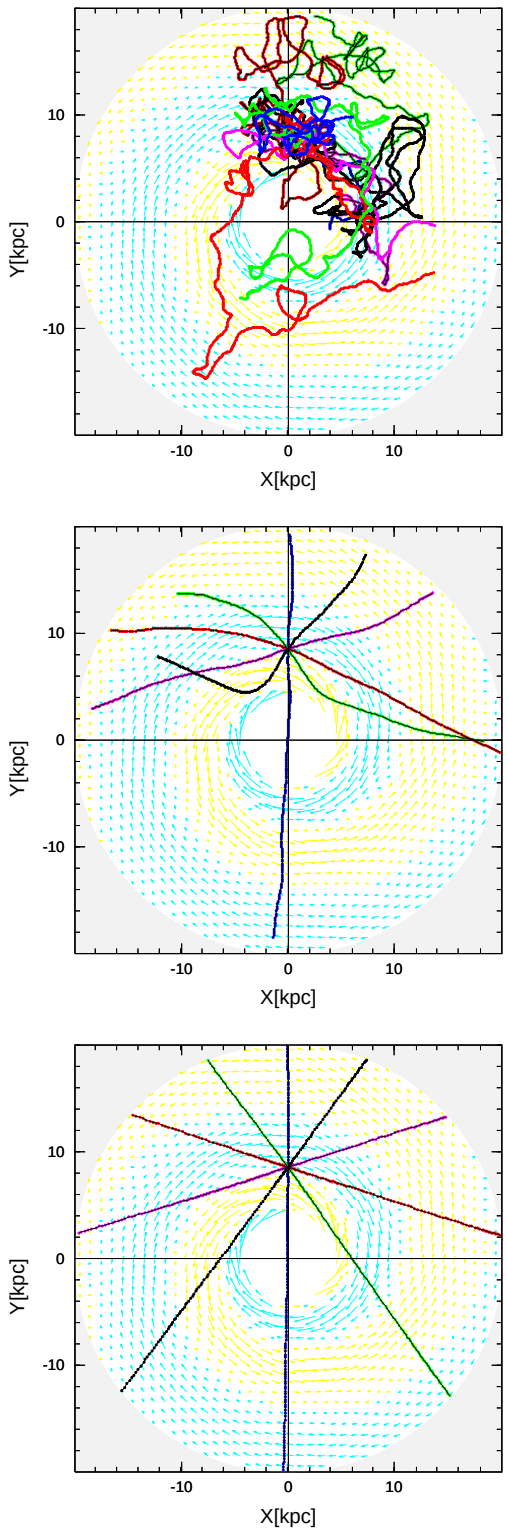

FIG. 1.11: The ray trace of proton particles in our Galaxy. In this calculation, the anti-proton is ejected from the Earth. At 10^{18} eV, the cosmic ray particles couple with magnetic field strongly. At higher energy, they travel more freely and the trajectories become linear.

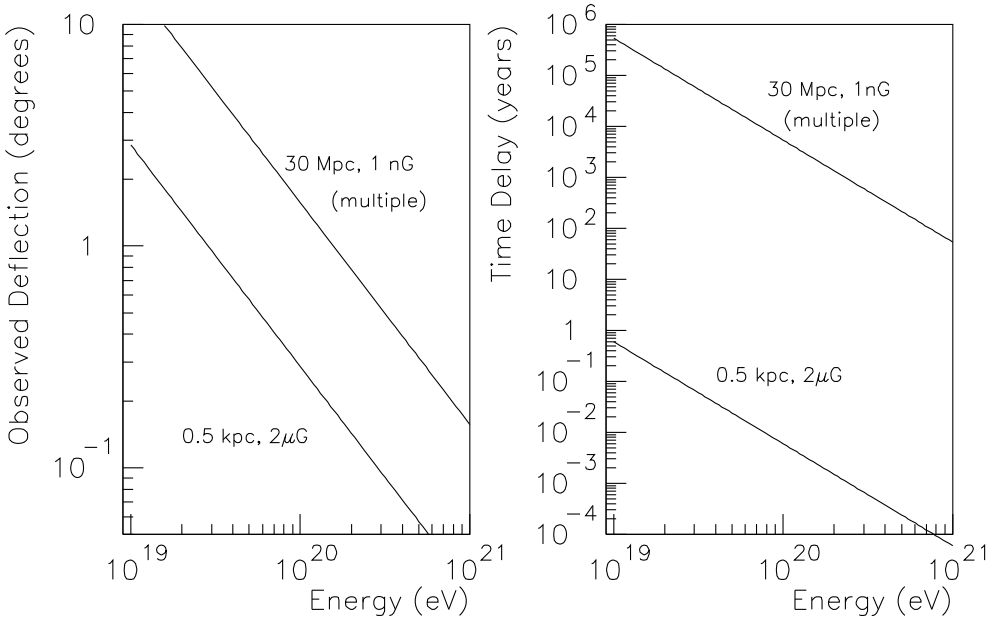

FIG. 1.12: Left: The deflection angle is shown as a function of primary cosmic ray energy. Upper and lower lines corresponds to propagation in the extra galactic space, and in our Galaxy, respectively. Here, we assumed magnetic field strength of 1 nG for the extra galactic space. Right: The time delay through the propagation relative to light.

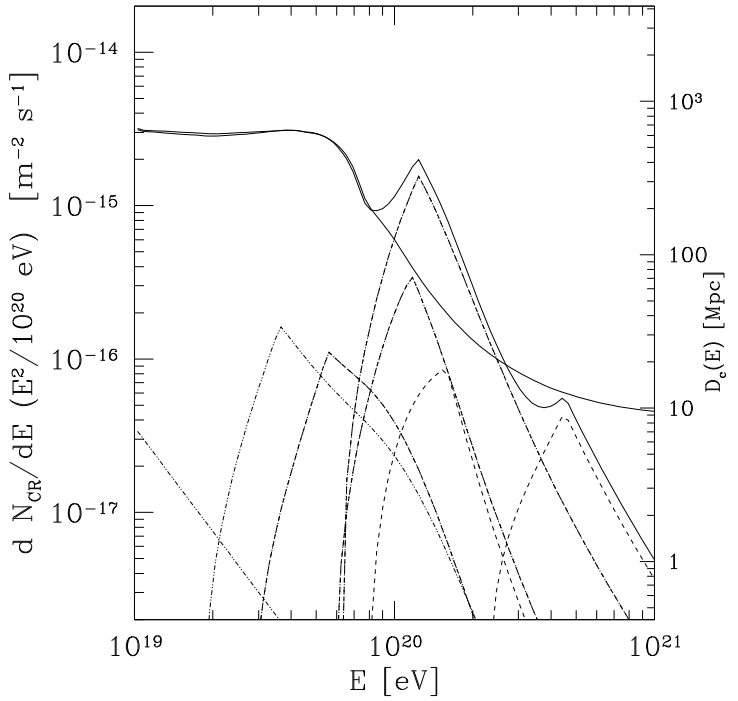

FIG. 1.13: The cosmic ray energy spectrum expected from GRBs source model. The cosmic ray observation period of 10 yrs is almost delta function if we consider the typical time delay of propagation, 100–1000 years. Since the time delay is energy dependent, we observe cosmic rays with limited energy range at certain time period. Realistic simulation predicts the spiky energy spectrum for each GRB. Older GRBs contribute in lower energy region, and closer GRBs have larger flux. If we assume stronger magnetic field, we expect wider energy spectrum for each GRBs.

by accelerated particles within the acceleration site as mentioned above. These models usually employ extreme values in parameters to explain the extension of the spectrum beyond 10^{20} eV.

There is another set of models with completely different approaches to explain the super-GZK particles. These are the so-called Top Down models in which EHE CR are produced in decays of superheavy particles (X-particles) [33, 34, 35, 36, 37, 38]. These new particles have to decay into ordinary particles during present era, and they have to be heavy enough and their number density and life time sufficient to explain the present EHE CR flux.

For example, the decay of cosmic strings may produce X particles (GUT gauge bosons), through the intersection of cosmic strings, cusp evaporation, self-intersection, or collapse of closed loops. Then X-particles decay into quarks and leptons while quarks give hadron jets. We expect a photon and neutrino dominant composition in the final products. Another possible source of X-particles is the annihilation of primordial monopole-antimonopole pairs (monopolonia) [39] or cosmic strings with monopoles (so-called necklace) [40, 37].

Another proposed concept is long-lived primordial X-particles. The X-particle must have a sufficient life time to survive until the present epoch and must decay at some finite rate in the present. These possibilities are discussed in the literatures [41, 42, 43].

Another possible scenario is that the primary particles are not ordinal particles. The possibility of neutrino [44, 38, 45] and supersymmetric hadrons S^0 [46] have been discussed.

A different approach is to assume that the special relativity is violated. This has been discussed by S.Coleman and S.L.Glashow [47]. In deriving the GZK cutoff, Lorentz invariance is assumed for $\gamma = 10^{11}$, however, there is no independent experimental confirmation that special relativity is valid at such high γ factor.

Hereafter, we will discuss in detail about some important scenarios.

- Superhigh energy neutrinos possibly emitted from powerful far-away sources could collide with nearby cosmological neutrinos with a mass of $0.1 \sim 1$ eV generating cosmic rays beyond the GZK cutoff energies [45, 48]. Extensive numerical calculation have shown this mechanism could explain the observed energy spectrum without violating the constraints obtained by high energy γ-rays, cosmic rays, and neutrino observations *if* the maximum neutrino energy reaches to $\sim 10^{22}$ eV and the relic neutrino dark matter is clustered on the supercluster scale (~ 5 Mpc) [44].

  · Positive Aspects
  This model relies on only well accepted physics. Observations of the highest energy cosmic rays could prove the massive cosmological neutrinos which are relics from the big bang.

  · Negative Aspects
  The sources must have a dense photon target to supply the required high neutrino luminosity and to absorb primary γ-rays and protons. The model is valid only if neutrinos have masses heavier than 0.1 eV.

  · This model predicts
  protons and γ-ray photons with energies beyond 10^{20} eV whose flux intensities

are comparable each other. High fluxes of neutrinos are expected (see the next section) whose arrival directions might have correlations with the γ-rays coming from directions of far-away astrophysical sources.

– Cold dark matter trapped in the Galactic halo might be origin of most energetic cosmic rays [49, 40]. An energy spectrum without cutoff is naturally expected because the particles are created inside our Galactic halo.

  · Positive Aspects
  If true, the study on extremely high energy astroparticles would probe the WIMPs, the most favored scenario in the dark matter hypothesis.

  · Negative Aspects
  There are too many free parameters to fit the observations.

  · This model predicts
  anisotropy associated with the Galactic center, but the AGASA data above 10^{19} eV does not support this [11]. More statistics is required to investigate anisotropy at 10^{20} eV, which would be a real test for this idea.

– If monopoles and/or cosmic strings (so called topological defects) were formed in symmetry-breaking phase transitions in the early universe, they may have produced EHE particles with energies up to the GUT scale (typically $\sim 10^{16}$ GeV) through their collapse or decay, with leptons and hadronic jets emitted from the supermassive "X" particles [33]. This Top Down models are attractive because they predict injection spectra which are considerably harder than shock acceleration spectra and which can extend to an energy of $\sim 10^{16}$ GeV, typical in GUTs [38].

  · Positive Aspects
  These models provide us with a way to probe the very early Universe when the GUT energies matched the thermal temperature of the Space. The absence of obviously identifiable astronomical objects is not a problem because the X particles need not be associated with any visible astrophysical sources.

  · Negative Aspects
  The model is exotic, relying on high energy physics notions that are far from proven.

  · This model predicts
  the comparable fluxes of protons and photons with energies beyond 10^{20} eV extending up to 10^{25} eV or even greater, and high fluxes of EHE neutrinos (see the next section). No astrophysical counterparts should be expected.

1.4 Physics of EHE Neutrinos and γ-rays

Neutrinos have uniquely advantageous characteristics in the Extremely High Energy (EHE) Astrophysics: they can penetrate cosmological distances in the Universe and their trajectories are not deflected because they have no electric charge. They carry information about extremely high energy production processes, even in the early Universe.

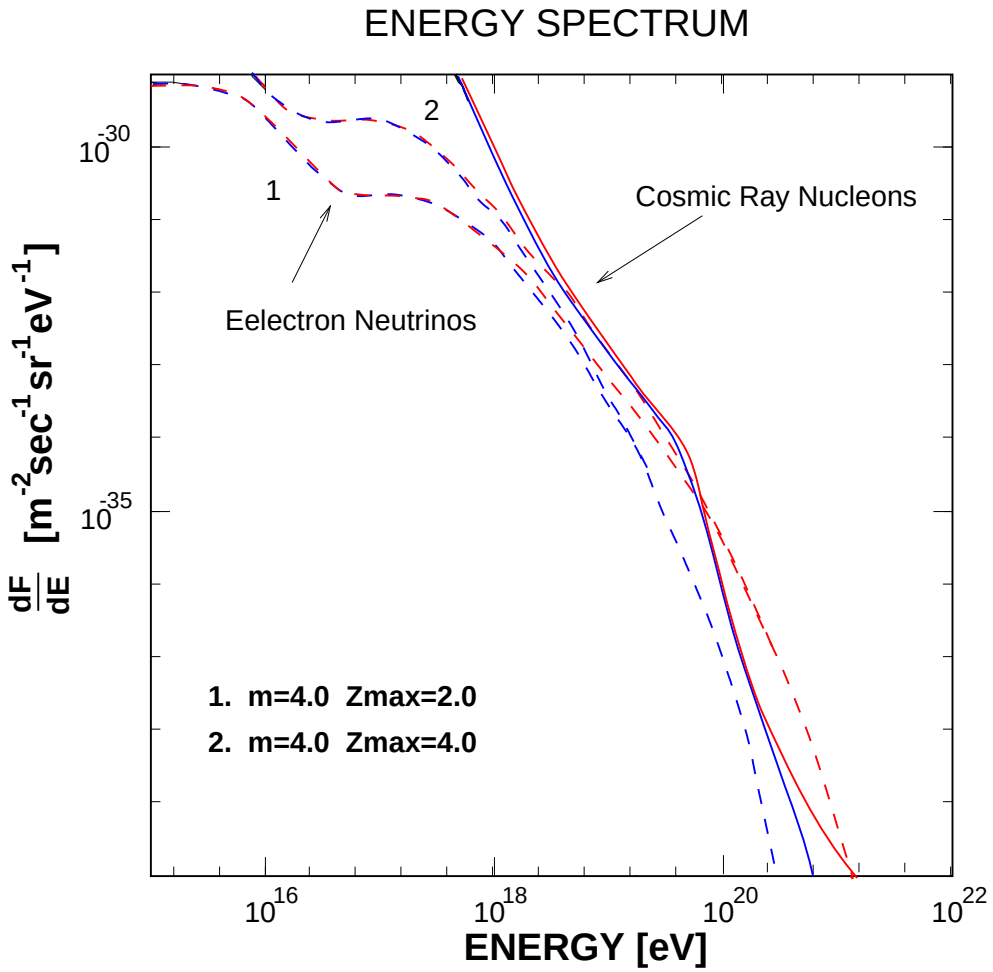

FIG. 1.14: Energy spectra of the EHE neutrinos produced by the GZK mechanism [17]. The maximum energies of cosmic ray protons at acceleration sites are assumed to be 10^{21} and 10^{22} eV respectively.

The most conventional process to create cosmic EHE neutrinos is a production by the GZK mechanism: the decay of photopions produced by EHE cosmic ray protons colliding with the cosmic thermal background photons [5, 50]. Figure 1.14 presents the GZK neutrino spectra under several assumptions concerning the EHE cosmic ray sources [17]. The neutrino flux below 10^{19} eV becomes higher as the parameter m characterizing source evolution and the "turn-on time" z_{max}, the boundary to which a spatial distribution of EHE cosmic ray emitters extends are increased. It is also seen that there is sensitivity to the value of maximum accelerated energy of EHE cosmic rays in the flux of neutrinos. The flux of neutrinos above 10^{19} eV depends strongly on the maximum energy of EHE cosmic rays, while the cosmic ray spectral shape itself does not depend strongly on the maximum energy. The flux of GZK neutrinos can be a good probe to estimate the turn-on time, evolution parameter, and the maximum energy of primary EHE cosmic rays.

The EHE neutrinos will also open up another interesting possibility: Astrophysical beams to search for cosmological relic neutrinos. Their energies may be high enough to collide with the 1.9 K cosmic background neutrinos to produce a significant neutrino cascade

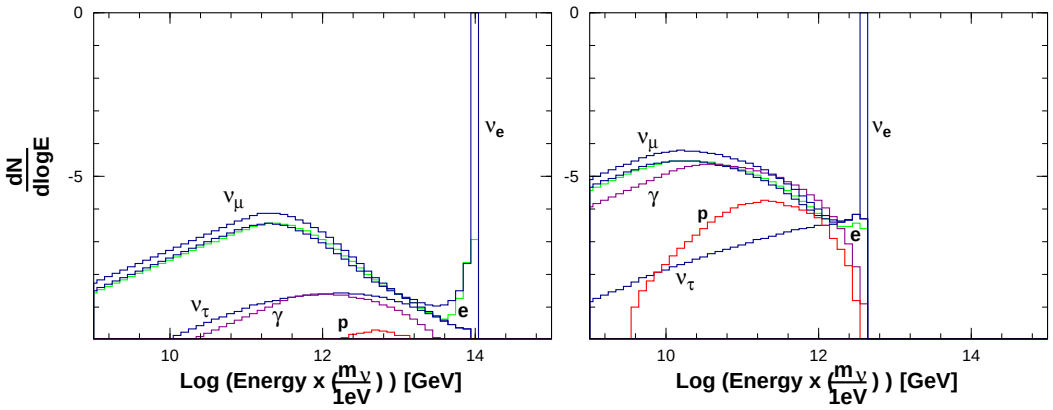

FIG. 1.15: Energy spectra of the particles in super-high energy neutrino induced cascades after the propagation of 1 Mpc. The left panel shows the case when primary electron neutrino energy is $10^{22} \times (m_\nu/1eV)$ eV and the right panel shows the case of $4 \times 10^{21} (m_\nu/1eV)$ eV, the energy at the Z boson resonance.

due to the enhanced interaction probability at Z-boson resonance [51, 52]. The cascading increases the total EHE neutrino flux because a single EHE neutrino can spawn multiple EHE neutrinos [52] as shown in Fig. 1.15. If neutrinos have a mass as suggested in the atmospheric neutrino observation by the Super-K, a dip structure with a slight enhancement of the flux at lower energies will appear in the EHE neutrino spectrum [53], which may provide the observational signature of relic neutrinos.

The neutrino cascading would provide the visible effects on the "Top Down" (TD) scenarios which supposes EHE cosmic rays are created directly as decay or interaction products of particles with masses much higher than the observed energies rather than being accelerated from lower energies. In the current versions of such (TD) scenarios, predominantly γ-rays and neutrinos are initially produced at extremely high energies by the decay of supermassive elementary "X" particles related to some grand unified theories (GUT). Such X particles could be released from topological defect relics of phase transitions which might have been caused by spontaneous breaking of GUT symmetries in the early Universe [33]. The EHE neutrinos with energies extending up to the GUT scale give rise to significant neutrino cascades.

Similar to neutrinos, the γ-rays and electrons produced by X particle decay initiate electromagnetic (EM) cascades on low energy radiation fields such as the CMB. The high energy photons undergo electron-positron pair production (PP; $\gamma\gamma_b \rightarrow e^- e^+$), and at energies below $\sim 10^{14}$ eV they interact mainly with the universal infrared and optical (IR/O) backgrounds, while above ~ 100 EeV they interact mainly with the universal radio background (URB). Electrons produced in this process transfer most of their energy to a background photon via inverse Compton scattering or sometimes via triplet pair production ($e\gamma_b \rightarrow ee^+e^-$). Since the EHE γ-ray attenuation length does not decrease with energy (as is the case for protons), there is no cutoff feature in the spectrum [54]. This leads to the prediction of a dominant γ-ray flux at energies above the GZK cutoff. Neutrinos and γ-rays driven by the cascades on the cosmological background fields are major players in EHE energy range.

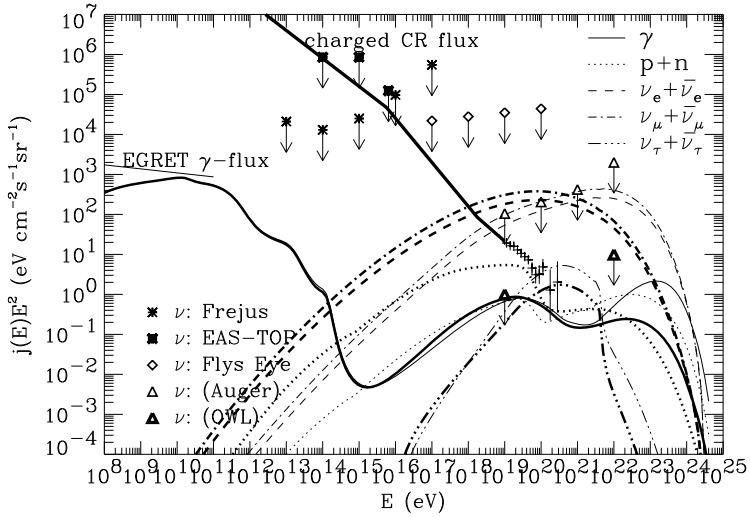

FIG. 1.16: Energy spectra of nucleons, γ-rays and neutrinos for the TD model with $m_X = 10^{16}$ GeV and the decay mode $X \to q + q$, assuming the high URB version and an EGMF of 10^{-10} G [38]. Thick and thin lines represent the SUSY and no-SUSY fragmentation function, respectively. 1 sigma error bars are the combined data from the Haverah Park [55], Fly's Eye [8] and the AGASA [4] experiments above 10^{19} eV. Also shown are piecewise power law fits to the observed charged CR flux below 10^{19} eV, the EGRET measurement of the diffuse γ-ray flux between 30 MeV and 100 GeV, and experimental neutrino flux limits from Frejus [56] and Fly's Eye [57], as well as projected neutrino sensitivities of the future Pierre Auger [58] and NASA's OWL [59] projects.

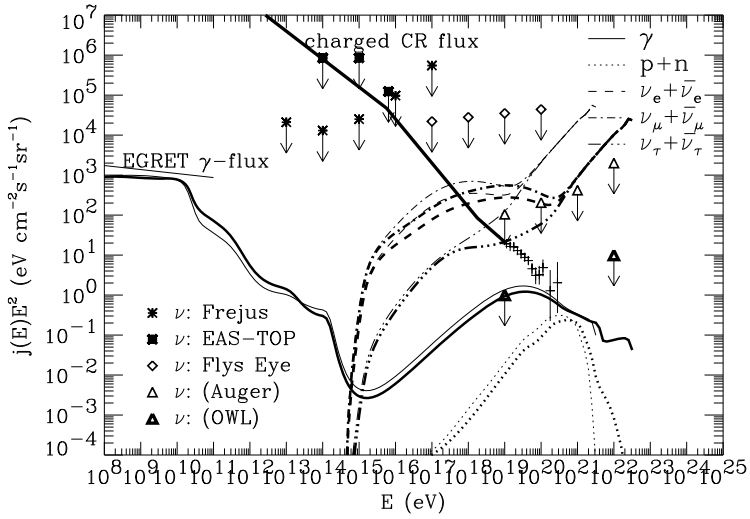

FIG. 1.17: Same as Fig. 1.16, but for the pure neutrino decay mode with no EGMF. Shown are the maximal EHE neutrino fluxes allowed by the EGRET limit for $m_X = 10^{14}$ GeV (thick lines) and $m_X = 10^{13}$ GeV (thin lines). A mass of neutrinos is assumed to be 1 eV here.

Figure 1.16 shows the fluxes of some TD scenarios along with current observational constraints on and projected sensitivities of some future experiments to γ-ray and neutrino fluxes [38]. The cosmic ray primaries with energies above 10^{20} eV can be γ-rays as shown in the figure. EHE neutrino flux is $\sim$ two orders of magnitude higher than that of cosmic ray hadrons at 10^{20} eV range.

Another interesting scenario involves the pure neutrino decay modes, also shown in Fig. 1.17 for $m_X \leq 10^{14}$ GeV [38]. Here, the γ-rays and nucleons are produced as secondaries from the interactions of these EHE neutrinos with the relic neutrinos. Because γ-rays and nucleons above 100 EeV must have been produced within a distance of $\lambda_a \simeq$ few Mpc from the observer, their flux is dominantly produced by interactions with the locally clustered neutrinos. The outstanding bumps in the neutrino spectra are created by the neutrino cascades discussed above. Their detection would be the observational evidence of the neutrino dark matter.

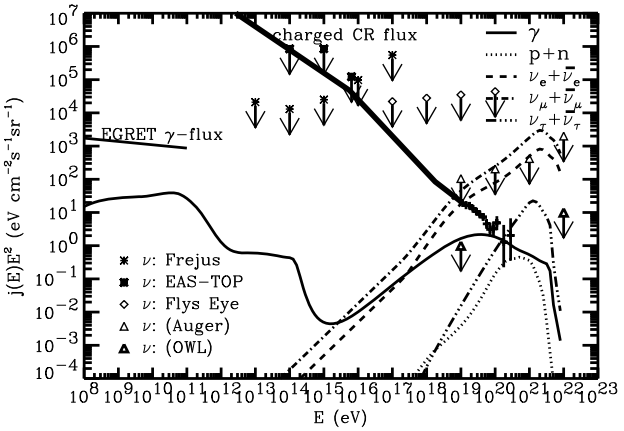

FIG. 1.18: Energy spectra of nucleons, γ-rays and neutrinos for the scenario of "Governor Neutrino" described in the text [44]. Neutrino sources are assumed to be distributed homogeneously up to $z = 3$.

It has been pointed out that collisions of EHE cosmic neutrino beams with $\sim$ eV mass neutrino dark matter themselves would explain the observed cosmic ray energy spectrum [45, 48], regardless of the nature of the neutrino sources if the maximum neutrino energy reaches to the Z boson pole region and the dark matter is clustered on the Supercluster scale by amounts consistent with expectations [44] because the secondary protons and γ-rays produced by the neutrino cascade as shown in Fig. 1.15 can constitute a hard component of the observed cosmic rays without a GZK cutoff. Powerful remote AGNs and/or cosmological gamma ray bursts (GRBs) can be the sites to radiate EHE neutrinos. In this model EHE neutrino could "govern" all the other EHE particle intensities. Figure 1.18 shows the spectra of the "secondary" cosmic ray protons and γ-rays with the "primary" neutrinos in this model [44]. A slight bump appears in the neutrino spectra because of the low energy secondary neutrinos in the cascade. It predicts γ-ray fluxes comparable or larger than nucleon fluxes above 10^{20} eV. Detection of neutrinos and primary γ-rays with arrival directions correlated each other associated with the remote astronomical objects will lead to indirect search for signatures of neutrino dark matter.

In summary, observations of EHE neutrinos and γ-ray photons at the EHE range would probe the astrophysics involving the phase transitions in the early Universe and/or the neutrino dark matter. Whether there are remarkable astronomical objects within their arrival directions is a key factor to distinguish the different models. Consequently the detector capability of reconstruction of neutrino and γ-ray events with excellent angular resolution would be crucial to this study. The resolutions expected in the Telescope Array will be discussed in Chapter 3.

1.5 Physics of Active Galactic Nuclei Neutrino

Active Galactic Nuclei (AGN) are a class of galaxies (Quasars, Blazars, Radio Galaxies, Seyferts, Optically Violent Variables, BL Lac's) which are characterized by large radio output and by large redshifts. They appear as star-like objects, indicating extremely high power output: 10^{42} to 10^{48}erg/s, many orders of magnitude greater than our own Galaxy and thus the most luminous objects known in the Universe. Their engines must not only be powerful, but extremely compact because their high energy luminosities are observed to flare by over an order of magnitude over time periods as short as a day [60]. They are assumed to consist of a super-massive black hole, having as much as 10^9solar masses surrounded by an accretion disk and a torus of hot gas. Jets are often seen along the axis of the disk. In a unified scheme of AGN, they correspond to Radio Loud AGN viewed from a position illuminated by the cone of a relativistic jet [61]. The 3rd EGRET catalog of high-energy γ-ray sources [62] contains 66 high confidence identifications of AGN and 27 lower confidence potential ones. All belong to the blazar subclass, mostly Flat Spectrum Radio Quasars, while the rest are BL-Lac objects [63]. Blazars appear also to be able to explain about 25% of the diffuse extragalactic γ-ray emission [64, 65]. TeV γ-ray emission has been observed from three blazars, the BL-Lac objects Mrk 421, Mrk 501, and 1ES2344+514 [66]. The data therefore strongly suggests that the highest energy photons originate in jets beamed to the observer [67, 68, 69].

Confronted with the challenge of explaining a relatively flat multi-wavelength photon emission spectrum which extends to TeV energy, models have converged on the blazar model shown in Fig. 1.19. Particles are accelerated by Fermi shocks in bunches of matter traveling along the jet with a bulk Lorentz factor of order $\gamma\sim10$. Ultra-relativistic beaming with this Lorentz factor provides the natural interpretation of the observed superluminal speeds of radio structures in the jet [70]. In order to accommodate bursts lasting a day in the observer's frame, the bunch size must be of order $\Gamma c\Delta t\sim10^{-2}$ pc, where Γ is the Doppler factor which for observation angles close to the jet direction is of the same order as the Lorentz factor [61]. These bunches are more like sheets thinner than the jet's width of $\sim$ 1 pc.

Most theoretical work on γ-ray emission in AGN jets involved electron acceleration and inverse Compton scattering, and these models will predict no neutrinos. In electron blazar models the multi-wavelength spectrum consists of three components: synchrotron radiation produced by the electron beam on the magnetic field in the jet, synchrotron photons Compton scattered to high energy by the electron beam to produce the highest energy photons in the spectrum [71]. The seed photon field can be either external, e.g., radiated

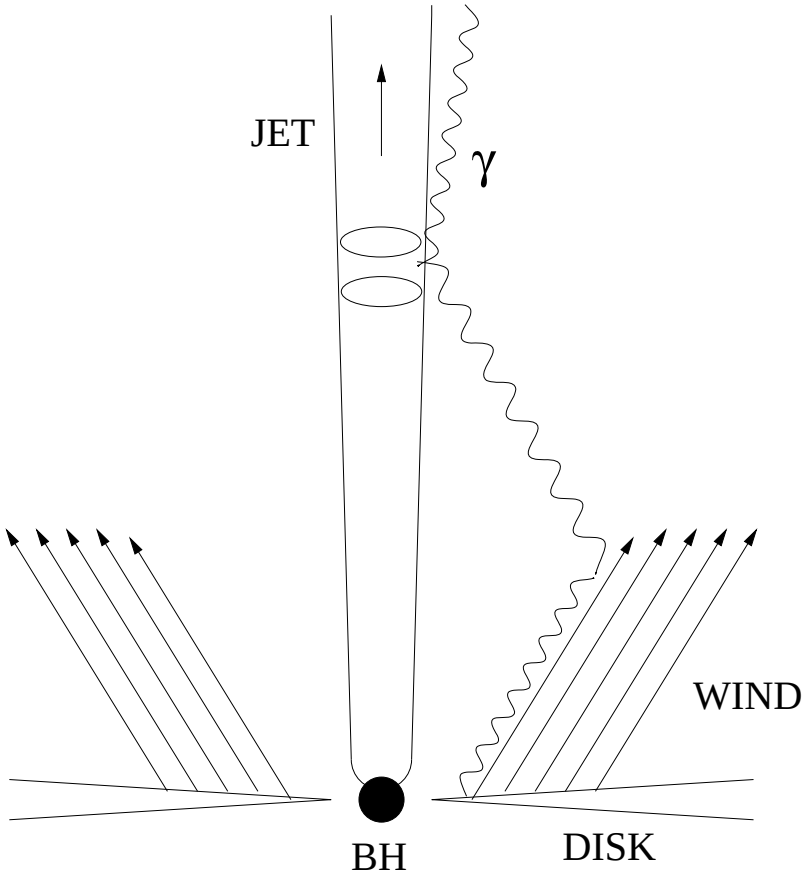

FIG. 1.19: Geometry of AGN.

off the accretion disk, or result from the synchrotron radiation of the electrons in the jet, synchrotron-self-Compton models. These models have problems. In order to reproduce the observed high energy luminosity, the accelerating bunches have to be positioned very close to the black hole. The photon target density is otherwise insufficient for inverse Compton scattering to produce the observed flux. The same dense target will efficiently absorb the high energy photons by $\gamma\gamma$ collisions. The natural cutoff therefore occurs in the 10–100 GeV region [71]. Finally, in order to prevent the electrons from losing too much energy before producing the high energy before producing the high energy photons, the magnetic field in the jet has to be artificially adjusted to less than 10% of what is expected from equipartition with the radiation density.

In some of the proton blazar models energetic protons interact with radiation via pion photoproduction [72]. Because of reduced energy loss, protons can produce the high energy radiation further from the black hole. The favorable production-absorption balance makes it relatively easy to extend the high energy photon spectrum above 10 TeV energy, even with bulk Lorentz factors that are significantly smaller than in the inverse Compton models. These models are turn out to describe the multi-wavelength spectrum of the AGN [73, 74]. Because the density of photons is still much higher than that of target protons, the high energy cascade is initiated by the photoproduction of neutral pions by accelerated protons on ambient light via the Δ resonance. The protons collide either with synchrotron photons

produced by electrons [73], or with the photons radiated off the accretion disk [74].

Model-independent evidence that AGN are indeed cosmic proton accelerators can be obtained by observing high energy neutrinos from the decay of charged pions, photoproduced on the Δ resonance along with the neutral ones. The neutrino spectrum can now be calculated from the observed gamma ray luminosity. We recall that approximately equal amounts of energy are carried by the four leptons (e^+,ν_μ, ν_e,$\overline{\nu}_\mu$) that result from the decay chaine, $\pi^+ \rightarrow \nu_\mu \mu^+ \rightarrow e^+ \nu_e \overline{\nu}_\mu$. The cross sections for the processes $p\gamma \rightarrow p\pi^0$ and $p\gamma \rightarrow n\pi^+$ at the Δ resonance are the approximate ratio of 2 : 1. Thus a ratio of neutrino to γ-ray luminosities (L_ν, L_γ) of 1 : 3. The ratio is reduced when taking into account that some of the energy of the accelerated protons is lost to direct pair production ($p\gamma \rightarrow pe^+e^-$) but the correction should be small ($\sim 10\%$).

We assume that the target photon density spectrum is described by a E^{-1}power low and the number of target photons above photoproduction threshold grows when the proton energy is increased. For a standard non-relativistic shock, protons are accelerated to a power low spectrum with spectral index 2, the threshold effect implies that the spectral index of the secondary neutrino flux is also a power low with an index flattened by 1 as a result of the increase in target photons at resonance when the proton energy is increased:

$$\frac{dN_\nu}{dE_\nu} = Norm \cdot \left(\frac{E_\nu}{E_\nu^{Max}} \right)^{-1},$$

here E_ν^{Max} is the maximum neutrino energy which can be derived by Fermi's shock acceleration theory assuming parameters around AGN. Therefore the normalization $Norm$ can be obtained by:

$$\int^{E_\nu^{Max}} dE_\nu \, E_\nu \frac{dN_\nu}{dE_\nu} \simeq Norm \cdot \left(E_\nu^{Max} \right)^2 \simeq L_\nu \simeq \frac{L_\gamma}{4}.$$

Assuming that the high energy γ-ray flux from Mrk 421 results from cascading of the gamma ray luminosity produced by Fermi Accelerated protons, we obtain the neutrino flux from the measured value of L_γ of 2×10^{-10} TeV cm^{-2}s^{-1} [67, 68, 69]:

$$E_\nu \frac{dN_\nu}{dE_\nu} \sim 5 \times 10^{-17} \mathrm{cm}^{-2}\mathrm{s}^{-1} \left(\frac{E_\nu^{Max}}{10^{18}\mathrm{eV}} \right)^{-1}.$$

This calculation reveals that the neutrino flux is essentially determined by the value for E_ν^{Max}.

In shock acceleration the gain in energy occurs gradually as a particle near the shock scatters back and forth across the front gaining energy with each transit. The proton energy is limited by the lifetime of the accelerator and the maximum size of the emitting region R [75]: $E_p < KeBRc$, where B is the magnitude of the ambient magnetic field which can be calculated from equipartition with the electrons whose energy density is measured experimentally yielding $B \sim 5$ Gauss, the size of accelerator R is determined by the duration, of order 1–2 day, over which the high energy radiation is emitted: $R = \Gamma tc \sim 0.01$–0.02 pc, and the constant K depends on the details of diffusion in the vicinity of the shock. In the case that the efficiency by which power in the shock is converted into acceleration

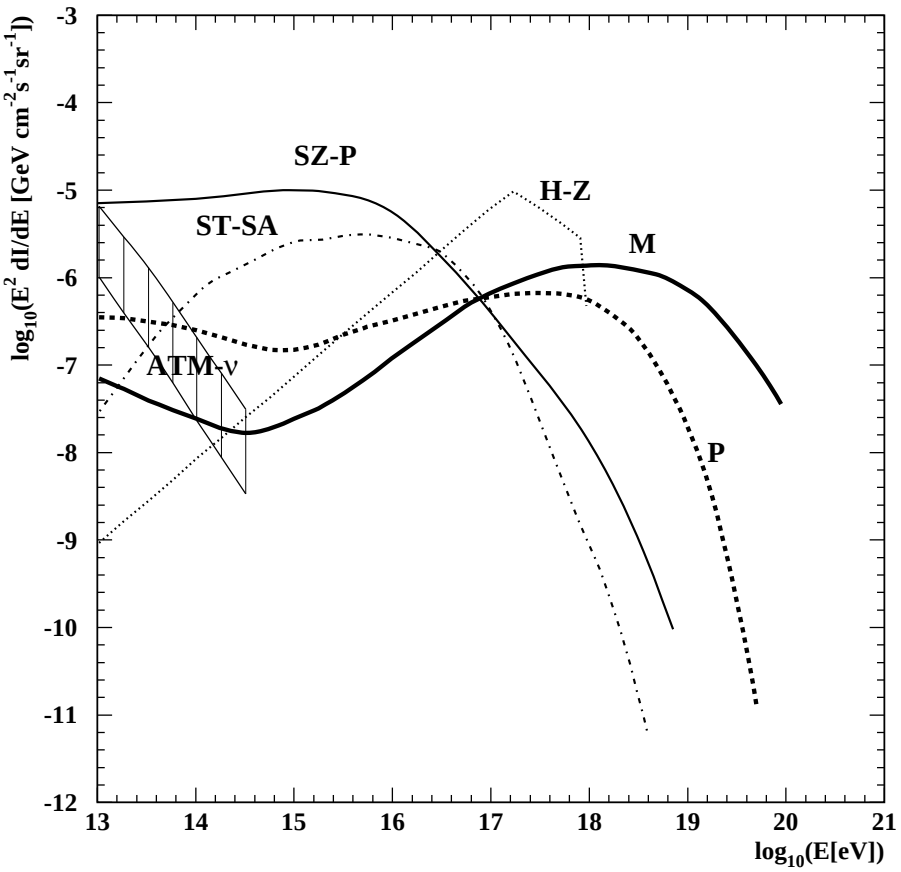

FIG. 1.20: Diffused neutrino flux predictions from AGN.

of particles reach values close to 1, the maximum proton energy reaches: $E_p^{Max} = eBRc = 5 \times 10^{19}$eV for $B \sim 5$ Gauss and $R \sim 0.02$ pc. The average energy carried by the neutrino in the photoproduction and decay chain, is roughly 1/20 of the parent proton energy. Finally the maximum neutrino energy is estimated to be $E_\nu^{Max} = \frac{1}{20} E_p^{Max} \sim 10^{18}$eV .

First models for neutrino production in AGN assumed shock acceleration in the AGN cores and predicted relatively flat fluxes up to energies of about 10^{15}eV [76, 77]. There is however recent evidence that the GeV to TeV γ-ray emission observed from AGN corresponds to the blazar class as described above [78, 74, 79]. In some proton blazar models [79], only interactions of protons with radiation via pion photoproduction ($p\gamma$) would lead to neutrino production as described above. The other models [77, 76, 78, 74] count contributions both from the processes of ($p\gamma$) and (pp) which makes a significant change of the spectrum in the lower energy region below 10^{15}eV. Diffuse neutrino flux predictions assuming the neutrino productions in the cores and in the jets are illustrated in Fig. 1.20 assuming Blazars appear to be able to explain about 25% of the diffuse γ-ray emission and the electron and muon neutrinos contribute to the flux but approximately the electron neutrino flux is a factor of two below the muon neutrino for all cases. From the assumptions

the fluxes have been corrected from the original estimates [77, 76, 78, 74, 79]. In Fig. 1.20, the range of atmospheric neutrino background as the zenith angle changes from 0° to 90° [80], which appears to have so large spectral index that it cannot largely contribute to neutrino detection in the higher energy region above 10^{15}eV in any proton blazar models.

Neutrino produce showers in most interactions with the atmosphere. In the interactions, the target nucleons break up and the debris behaves as a group of hadrons that results in a shower similar to those induced by hadronic cosmic rays in both neutral and charged current interactions. If the neutrino is of electron flavor the interactions with the electrons have in general much smaller cross sections and can be disregarded except for the resonant electron-antineutrino electron interaction which dominates just for neutrino energies around the resonant value of 6.4 PeV. The potential of TA to detect neutrinos of energies more than 10^{16}eV through deeply penetrating air showers will be described in the later section. Assuming some simple conservative trigger and selection requirements we obtain the acceptance for deeply penetrating air showers as induced by high energy neutrinos and we then give the expected event rates for a variety of AGN neutrino fluxes as predicted in different models with are used here.

In conclusion, using the great sensitivity for extremely high energy neutrinos with the TA detector, we can establish or reject the proton AGN model by detecting enough statistics of AGN neutrinos and confirming the coincidence with EGRET catalog of high confidence identifications for AGN. Furthermore, we can resolve the location of the proton acceleration near the core or in the jet of AGN by testing the spectrum slopes as predicted in Fig. 1.20.

Chapter 2

TA Detector

2.1 Conceptual Design

The Telescope Array (TA) detector has been planned in order to draw a decisive conclusion on the mysterious origin of the extremely high energy cosmic rays. For this purpose, the detector is required to have much larger aperture for super-GZK events than the present day detectors. Also it should provide a particle identification as well as an accurate determination of energy and arrival direction for primary cosmic rays.

The TA is a giant array of air fluorescence detectors to satisfy these requirements. It measures the UV fluorescence of molecular nitrogen generated by the air shower particles by large aperture telescopes. The observation of the whole shower development process in the atmosphere enables the unbiased determination of the energy by the total absorption calorimetry. A single air shower event will be observed simultaneously by 2 or more telescopes separated by more than 40 km, which allows an accurate determination of the event geometry by the stereo event reconstruction.

The particle identification of the primary particle is made by measuring the longitudinal development of the shower in the atmosphere. The depth of the shower maximum (X_{max}) is a good parameter for the identification. This technique has a great advantage to discriminate gamma rays and neutrinos from other primary cosmic rays, which is the essential feature of the experiment to identify the origin of EHE cosmic rays.

The effective aperture of TA is approximately 5,000 km^2 sr for 10^{20} eV particles assuming a 10 % duty factor. It is 30 times larger than the existing AGASA ground array, and is an order of magnitude larger than the new fluorescence telescope, HiRes. The future generation ground array, the southern hemisphere Pierre Auger in Argentina, will have about the same acceptance.

The Telescope Array consists of 10 measurement stations installed in the West Desert of USA, near Salt Lake City, Utah. Each station is separated by 30–40 km and is deployed as shown in Fig. 2.1. The Fly's Eye, HiRes and Utah Seven Telescopes group have been operating in the vicinity. Three out of 10 TA stations cover the planned northern hemisphere Auger detector, forming a large hybrid detector each having about the same effective acceptance for the EHE cosmic rays.

Each TA station is equipped with two rings of 20 imaging telescopes arranged in a circle of ϕ ~30 m. The upper ring covers the elevation angle of 3°–18.5° and the lower ring

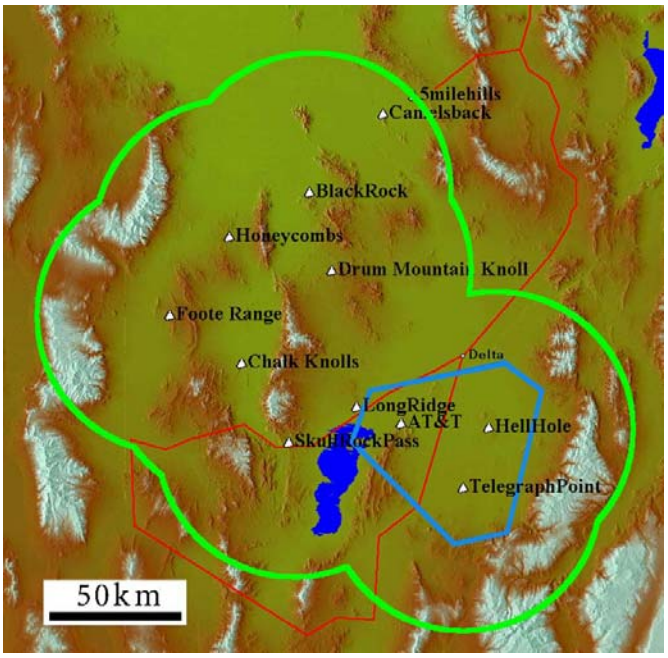

FIG. 2.1: Station deployment of Telescope Array.

covers 18.5°–34°. A total of 40 reflecting telescopes with 3 m ϕ mirror is installed in a station. It covers 360° in azimuth and is sensitive to the cosmic rays falling within $\sim$ 60 km of the station. The cosmic rays above $10^{18.5}$ eV will be measured simultaneously by 2 or more stations and the stereo reconstruction will be applied. The cosmic rays below this threshold will be measured by a single station down to 10^{16} eV. These low energy events are close to the station and a monocular reconstruction of the geometry will be applied.

The development of the shower in the atmosphere is recorded by the imaging camera placed on the focal plane of each telescope. It is composed of a 16 $\times$ 16 matrix of hexagonal photomultipliers (PMTs). The field of view covered by one PMT (pixel size) is approximately 1° $\times$ 1°. The signal from the PMT is digitized every 200 ns with a 12-bit resolution. The dynamic range of 16 bits is achieved by the 2-range (H/L) digitization scheme. Each channel is equipped with a digital signal processor (DSP) and a sophisticated signal finding algorithm will be executed for generating a trigger.

A steerable laser is placed at the center of each station. It will be used to determine the extinction coefficient of the fluorescence light along the transmission path to the telescope.

2.2 Site and Infrastructure

The Telescope Array requires a vast extent of land with good atmospheric transparency, good weather and dark night sky free from the light pollution by human activities. At the same time, contradictory conditions of good infrastructure such as the access road, power line, computer network and communication are desirable for the construction and operation of the experiment.

We have selected the West Desert of USA, 100–200 km south west of Salt Lake City in the state of Utah as the site of experiment. The annual precipitation of this region is approximately 250 mm and the rate of "good" weather is more than $\sim$ 60 % of the year. The original air fluorescence experiment, Fly's Eye, operated in the vicinity and recorded the measurement duty factor of 10 %. The second generation experiment, HiRes, has monitored the air clarity over one year, and concluded that the air clarity of this region in equivalent or better than the US standard desert model (see §3.3 for more details).

The deployment of TA measurement stations is shown in Fig. 2.1. A total of 10 stations form an approximate two-dimensional array with the distance to the nearest neighbors 30–45 km. A completely linear (one-dimensional) station deployment would give slightly larger acceptance but the 2-dimensional array offers a high level of redundancy by measuring the same events with multiple number of stations. A minimum of 2 stations will be required for the stereo reconstruction but more stations will give further information to check the internal consistency of the energy and direction measurement. The level of consistency is a good measure of the systematic uncertainty. The approximate sensitive area of the experiment is shown by a set of circles in the figure. The Monte Carlo simulation shows approximately 50,000 km str acceptance for 10^{20} eV protons.

The stations of HiRes experiment are located at the Camel's Back and Five Mile Hills in the Dugway Proving Ground (see Fig. 2.1). Its sensitive region overlaps with a northern edge of the TA's acceptance. The ground array of the northern Pierre Auger Observatory is indicated by the 'Superman Triangle' in the figure. Three stations of TA at Hell Hole, Telegraph Point and AT&T are expected to serve as the 'fluorescence eye' of the Auger detector.

Table 2.1: List of TA sites.

#	location	latitude	longitude
1	Black Rock	39.873 N	113.258 W
2	Honeycomb	39.724 N	113.583 W
3	Drum Mountain	39.610 N	113.167 W
4	Foote Range	39.460 N	113.822 W
5	Chalk Knolls	39.300 N	113.533 W
6	Skull Rock Pass	39.031 N	113.340 W
7	Long Ridge	39.151 N	113.070 W
8	AT&T	39.074 N	112.842 W
9	Hell Hole	39.081 N	112.536 W
10	Telegraph Point	38.880 N	112.639 W

The geographical locations of 10 candidate sites are listed in Table 2.1. All the stations are at the altitude of 1500–1600 m above the sea level. Most of the land for the sites are public lands owned by the Federal Government, and the permission of the use is to be applied to the Bureau of Land Management. Some details of the site attributes are given elsewhere [81]. The northern 5 stations (#1 – #5) and AT&T (#8) are located on a knoll or a small hill approximately 100 m above the surrounding land. It is favorable for having less obscuration in the field of view and for avoiding the coverage of the fog and the mist near

the ground level. Theses sites are remote and the construction of access road to the top of the knoll is required. The night sky is very dark for these stations. Other stations, mainly in the southern part of the TA acceptance, are on the small plateau and the elevation with respect to the surrounding land is not large. The access is easier but the road and farming land suggest a possible disturbance to the measurement by higher human activities. There is a large lake (Sevier Lake), a small town (Delta) and a power plant (Intermountain Power Plant) in this region. Although these are no essential obstacles to the first sight, we intend to carefully investigate the difference of the night sky background and the atmospheric clarity between the northern and southern sites.

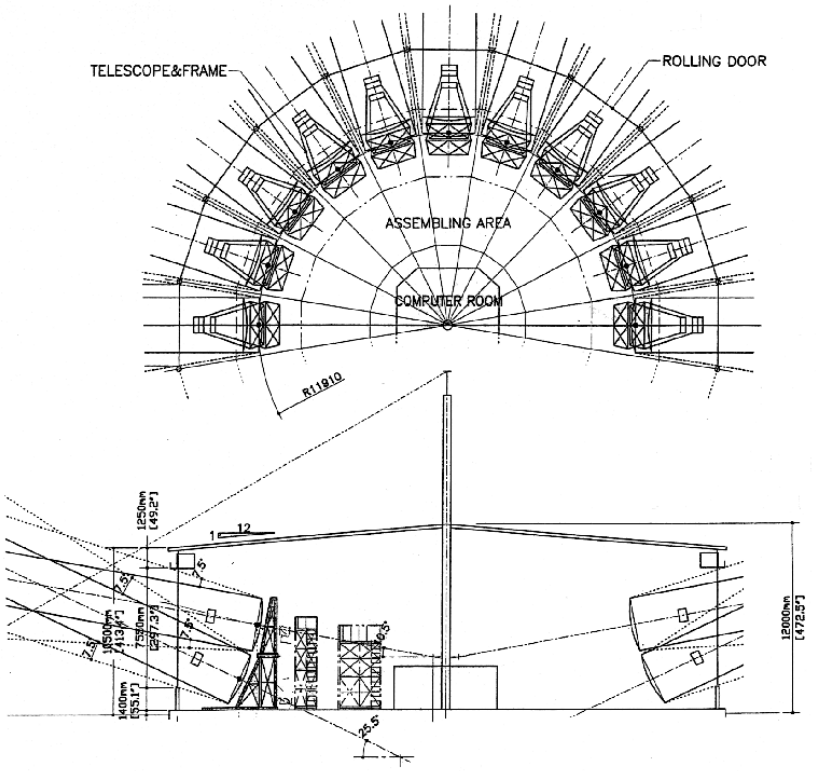

FIG. 2.2: Plan and cross sectional view of the telescope housing.

The site will be flattened to install a station building shown in Fig. 2.2. The building has a diameter of $\sim$ 30 m and the height of $\sim$ 10 m. A gravel road with the width of $\sim$ 15 feet will be made from the nearby public road to the site on top of the hill. The station requires approximately 70 kWatt of electricity for the electronics, computers and associated installations such as the air conditioning and the rolling door of the station building. It will be supplied from the nearest power line. In case the available power line is far away from the station, we intend to install a local power generator. A Uninterrupted Power Supply (UPS) system and a small generator with limited capability will be installed for the safety operation of the station for emergency cases when the power is interrupted.

The computer network connection to the TA site is indispensable; it will be used for the real time data exchange for the intersite trigger and laser shooting, remote control and monitoring of the data acquisition, collection of the acquired data from each station

to the central station and for the general communication between stations. We plan to install a private optical fiber line to all the stations for the network connection. For some of the remote stations, however, the network by the microwave communication may be the more convenient alternative, though it requires a straight line of sight and the speed of communication is slower. We are in the process of installing a microwave connection to one of the planned site (Black Rock Hills) to check its performance in the field use. A backup communication with limited capability may be supplied by the satellite telephone communication. The safety related operation of the station such as the power on/off and opening/closing the rolling door will be controllable both by the optical fiber connection and the satellite telephone connection.

2.3 The Telescope and Optics

A TA station consists of 40 units of fixed telescopes each covering a certain region of the sky. The field of view (FOV) of one telescope unit is 18.0° in azimuth and 15.5° in elevation. The upper ring composed of 20 telescope units covers the entire azimuthal angle and the elevation angle of 3° – 18.5°. The lower ring covers 18.5° – 34° in elevation.

We have employed a spherical mirror optics to obtain a wide FOV with reasonable focusing power. The support and adjustment mechanism for the segmented mirror is also simpler for the spherical mirror compared with the parabolic one. A ray tracing simulation is made for the spherical mirror telescope with a planar imaging plane located near the focal point. The result is shown in Fig. 2.3. Parallel light beam was injected every 4° in horizontal and vertical directions and its image on the camera is plotted. The obscuration by the PMT camera is taken into account. The spot size of 30 mm in FWHM is obtained in most of the FOV. It is sufficiently small compared with the PMT dimension (61 mm between two opposite edges of hexagon) and does not contribute much for determining the resolution of the telescope.

The telescope has a main dish with a diameter of 3.3 m which is composed of 18 hexagonal shape segment mirrors (see Fig.2.4). The attachment angle of each mirror is adjustable in two directions. The location of the central mirror is made empty and is reserved for the optical alignment system and PMT calibration system. The detailed design parameters of the telescope and the segment mirror is given in Table 2.2.

A design of the segment mirror is shown in Fig. 2.5. The mirror is made by 10.5 mm thick Tempax glass (Schott corp.). A support disk of 150 mm diameter made by the same material is glued behind the mirror by 3M Dymax 840 glue. The disk is used to support the segment mirror from the telescope frame.

The segment mirror is shaped by heating a planar glass on a ceramic mold plate in the temperature controlled electric oven (see Fig. 2.6). Including the annealing, the production process takes one day to make one mirror. We expect the specification of the mirror is achieved without significant polishing. The mirror surface is coated with 200 nm thick aluminum produced by the vacuum deposition. A hard protection surface of Al_2O_3 crystal with thickness of 50 nm is then produced in the solution containing ammonium hydroxide, tartaric acid and ethylene glycol. The reflectivity of the finished mirror is shown as a function of wavelength in Fig. 2.7. The reflectivity greater than 88% is obtained between

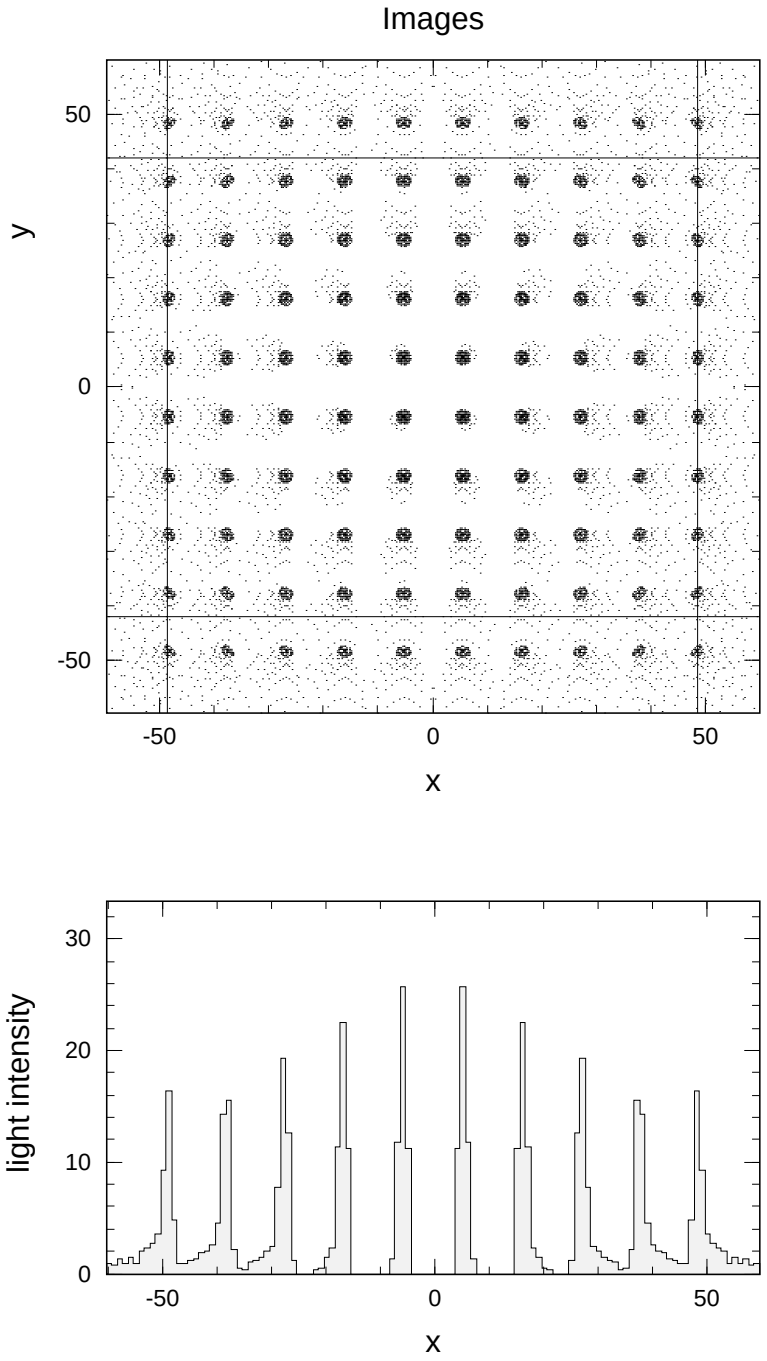

FIG. 2.3: Expected image of TA telescope unit.

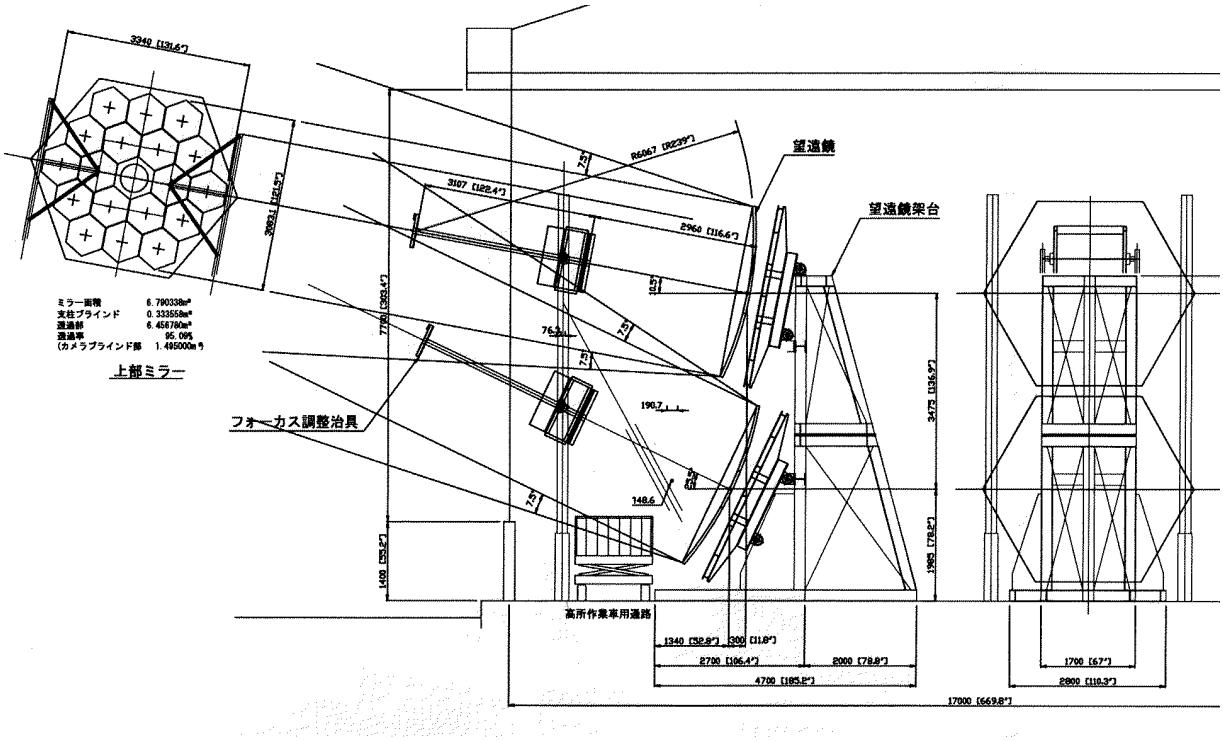

FIG. 2.4: Mechanical design of TA telescope.

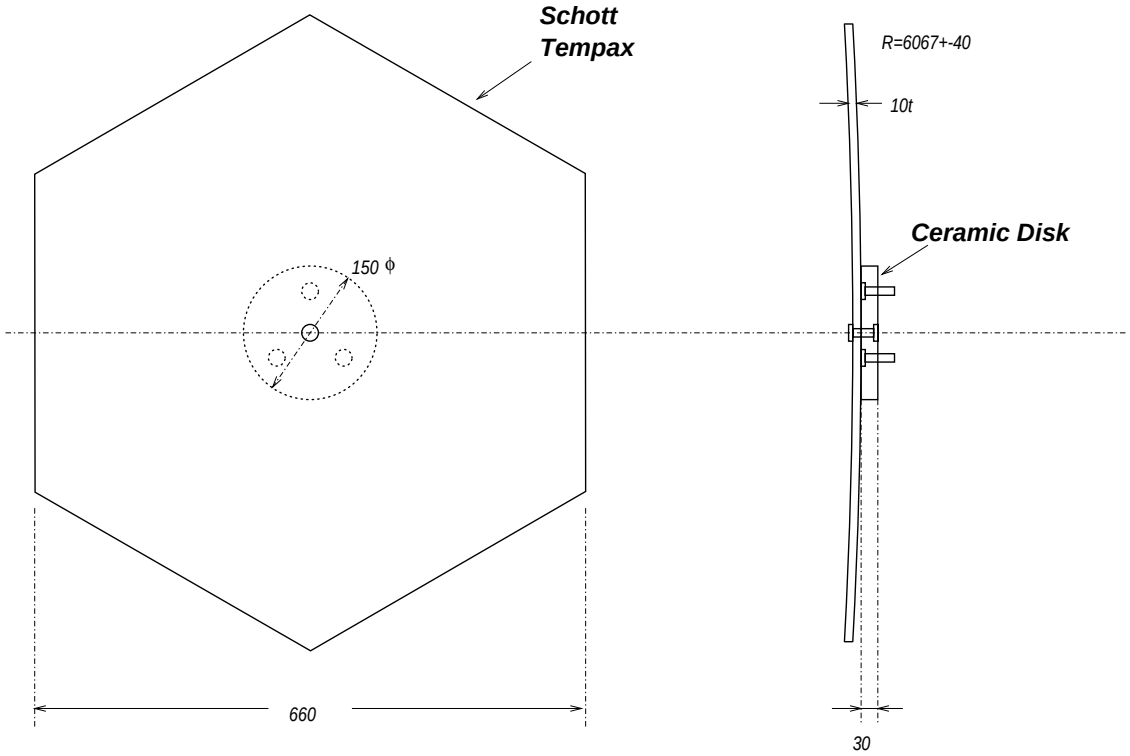

FIG. 2.5: Design of the segment mirror.

Table 2.2: Design parameters of TA telescope.

Telescope	
Diameter	3.3 m
Total Mirror Area	6.8 m^2
Focal Length	2960 mm
Mirror Optics	spherical
F.O.V.	18° horizontal × 15.5° vertical
Max. Wind velocity for Operation	15 m/sec
Number of Segmented Mirrors	18
Segment Mirror	
Shape and Dimension	hexagonal, 660 mm between opposing edges
Mirror Area	0.377 m^2
Radius of Curvature	6067 ± 40mm
Spot Size	$\leq$ 10mm in diameter
Base Material	Tempax glass, 10.5 mm thick
Mirror Coating	aluminum
Surface Protection	anodization; Al_2O_3, $\sim$ 50 nm
Reflectivity	$\geq$ 88 % at 350 nm
Weight	10.7 kg

330 nm and 450 nm. This curve can be adjusted to have a peak around 350 nm by tuning the thickness of anodization. The anodized surface is stable and the degradation of the reflectivity is $\sim$ 1 %/year from the experience of Fly's Eye and Utah Seven Telescopes groups. The mirror surface can be washed by pure water for the regular maintenance in the field.

We are simulating the distortion of the mirror system by the high velocity wind using the finite element analysis. The displacement of the mirror is to be less than a few mm under the wind velocity of 15 m/sec. Such a high speed wind occurs in less than 1 % of the observation time according to the weather monitoring at Dugway Proving Ground, where Fly's Eye and Utah Seven telescope groups had been operated. The temperature coefficient of the focal length was measured and found to be negligibly small (0.3 mm/degree).

Safety hazard tests were made for the prototype mirrors by destroying the mirror by applying the impulsive shock at the edge of the mirror. The present design stands for the shock applied with a momentum of 250 kg m/sec, which corresponds to a kick or a straight punch to the mirror by human adults.

FIG. 2.6: Electric oven (left) and ceramic mold (right) used for the production of segment mirror.

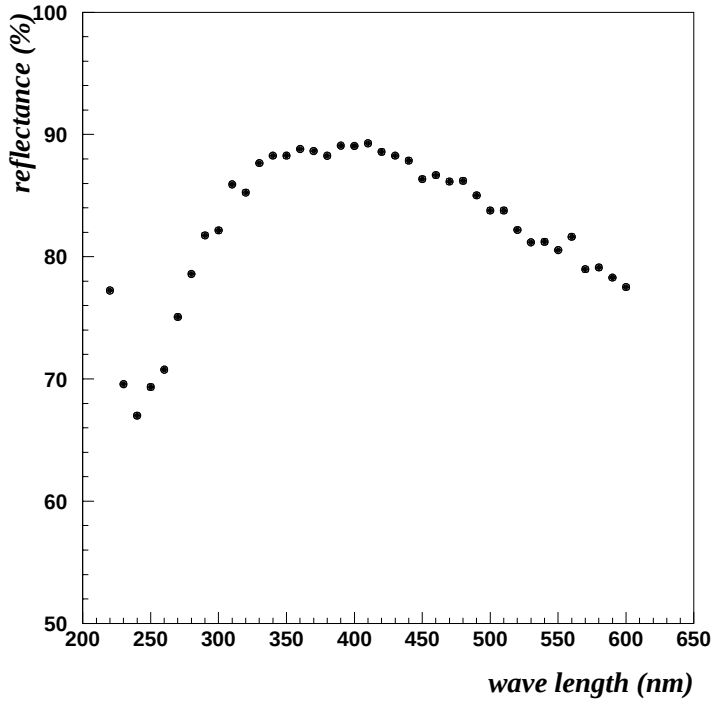

FIG. 2.7: Mirror reflectivity as a function of wavelength measured after the anodization.

2.4 Photomultiplier and Camera

A set of 256 hexagonal PMTs is arranged in 16×16 array to form an imaging plane of the camera. A single camera covers the sky of 18° in azimuth and 15.6° in elevation with a pixel acceptance of 1.1° × 1.0° for one PMT. A UV transparent filter (BG3) with a thickness of 6 mm is placed in front of the PMT to reduce the number of night sky background photons. A wedge-shaped reflector is installed at the edge of the photocathode to minimize the insensitive area between PMTs and to improve the uniformity of the imaging plane. The calibration and monitoring of the PMT gain will be made with a small light pulser of YAP scintillator mounted on a computer controlled X-Y stage in front of the camera. The electronic circuits including the digital processing units are installed inside the camera box, so that the number of cables to the central station are much reduced.

2.4.1 PMT

PMT: Hamamatsu R6234

The PMT planned to be used in the Telescope Array project is Hamamatsu R6234, which has a hexagonal bialkali photocathode and borosilicate glass window. The dimensions of the PMT and a typical quantum efficiency are shown in Fig. 2.8. The PMT has 8 dynodes of a box-line focus type and a typical gain of 2.7×10^5 at 1000V. Characteristics of the PMT are summarized in Table 2.3.

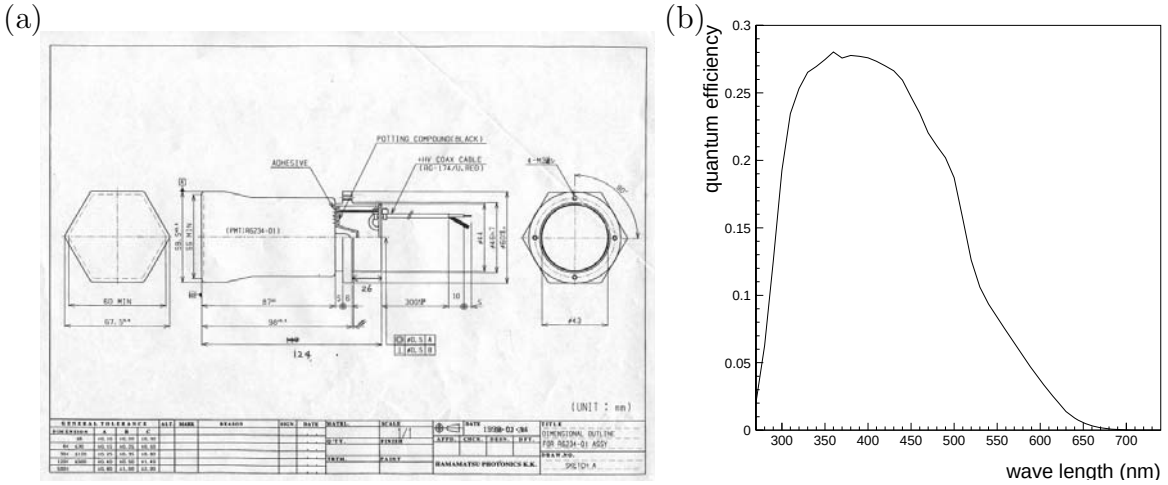

FIG. 2.8: (a) Dimensions of HamamatsuR6234. (b)Typical quantum efficiency of Hamamatsu R6234.

The bleeder circuits

The field of view of one PMT (pixel) is about 1°. The night sky background is approximately 30 photoelectrons in 200 ns and it is equivalent to the anode current of 1.9μA at the gain of 8×10^4 (see §2.5 for details). This is not completely negligible compared with

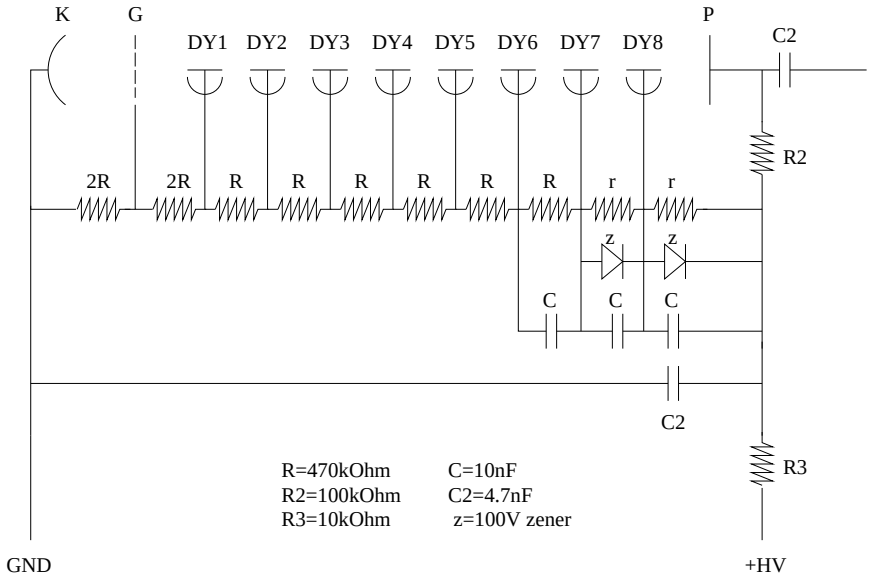

FIG. 2.9: Hybrid bleeder circuit with Zener diodes.

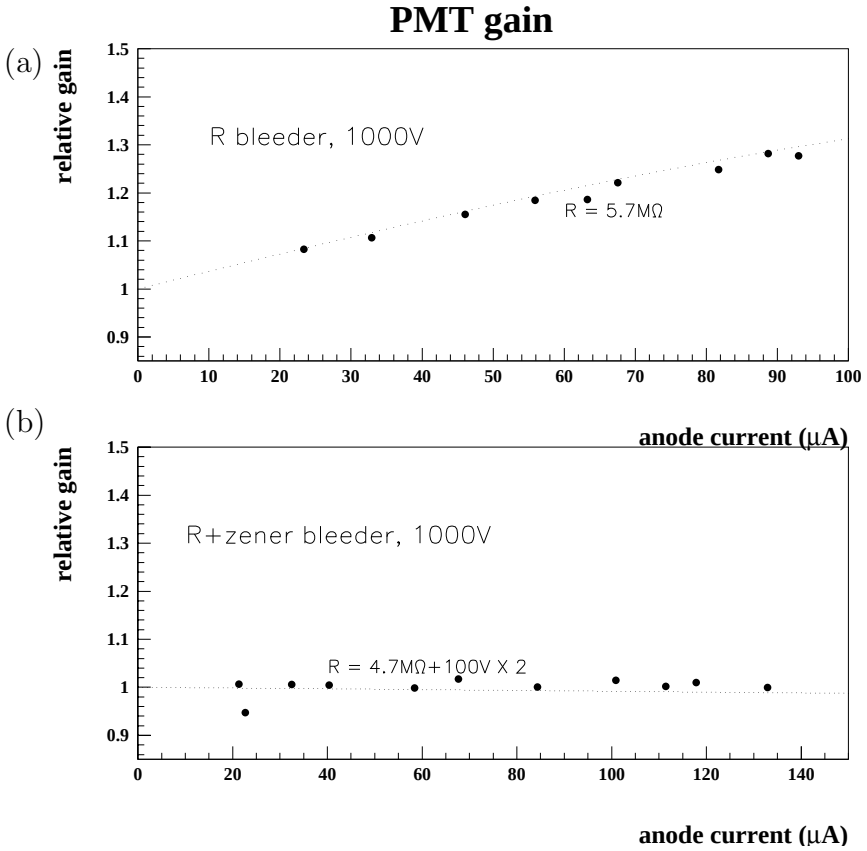

FIG. 2.10: Pulse gain variation against background anode current, with the ordinary bleeder circuit (a) and with the hybrid bleeder circuit (b).

Table 2.3: Characteristics of the Hamamatsu R6234

Shape and Dimension	hexagonal, 60 mm diagonal
Dynode Structure	box-line focus
Number of Dynodes	8
Quantum Efficiency (max.)	30 %
Gain (typ.)	2.7×10^5 (1000 V)
Anode Dark Current (typ.)	2 nA
Anode Dark Current (max.)	20 nA
Rise Time	6.0 ns
Transit Time	52 ns

the maximum bleeder current of ~ 0.2 mA. Moreover, the anode current fluctuates continuously during the observations. This fluctuation changes the PMT gain significantly when we use an ordinary bleeder circuit by the register chain. In order to avoid this problem, we developed a hybrid bleeder circuit using Zener diodes at the last 2 stages of the dynode chain (see Fig. 2.9).

The measured variation of the pulse gain against the background anode current is shown in Fig. 2.10. As shown in the figure, the pulse gain of the hybrid bleeder is almost constant in the wide range of anode currents.

Linearity

Following the simulation, the largest PMT signal to be detected is 6×10^4 photoelectrons in 200 ns time window (see §2.5 for detail). This corresponds to 4.2 mA anode current assuming the PMT gain of 8×10^4. The linearity of PMT depends on the relative voltages applied to the last few dynodes. In Fig. 2.11 we show the linearity measured for the various types of bleeder circuit. The hybrid bleeder with Zener diode shown in Fig. 2.9 (filled circle) gives the optimum result. The deviation from the linear response is ~ 1 % for the anode current of 4.2 mA, and is within 5 % up to 20 mA, which is sufficient for the TA's requirement.

Temperature dependence

The PMT camera is exposed to the ambient air during the observation. The gain of PMT may vary from hour to hour reflecting the temperature change of the PMT and bleeder circuit. It is necessary to measure the temperature dependence of the PMT pulse gain and correct its effect in the data analysis. We measured the PMT gain variation for the ordinary and the hybrid bleeder circuit for a temperature range from -20°C to 40°C. The results with the ordinary bleeder is shown in Fig. 2.12 (a). The temperature coefficient is -0.39 ± 0.02 %/K and it is consistent with the typical temperature coefficient of $-0.2 \sim -0.5$ %/K for the bialkali PMT. The result of the same PMT with the hybrid bleeder is shown in Fig. 2.12 (b), and the coefficient is -0.57 ± 0.03 %/K. This result is larger by 0.2 %/K than that of the ordinary bleeder, which can be explained by the temperature coefficient of Zener diodes (0.095 %/K in typical).

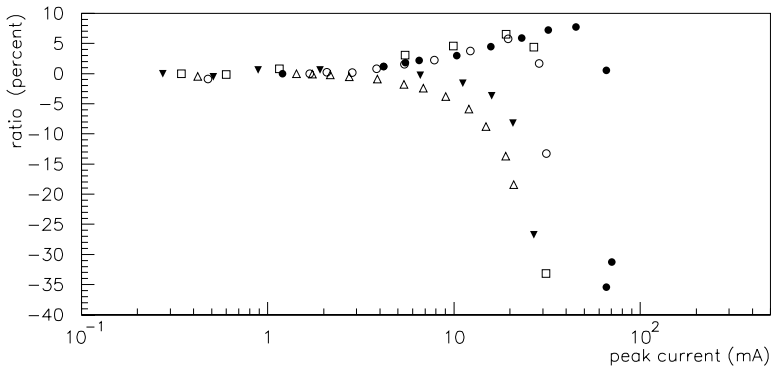

FIG. 2.11: Measured linearity of the pulse gain for various bleeder circuits. All the measurements are made under the conditions of same pulse gain $\sim 10^5$ (i.e., HV values are different). The light pulse width is 300ns. All the bleeders have the same registers until DY6, as same as shown in Fig. 2.9. The resistances of (DY6–DY7),(DY7–DY8) and (DY8–P) are; *open circle*: R,2R,1.5R, *open triangle*: 2R,2R,2R. And the voltages of Zener diodes of (DY6–DY7),(DY7–DY8) and (DY8–P) are; *filled triangle*: 75V,130V,95V, *open square*: 62V,130V,100V, *filled circle*: R,100V,100V.

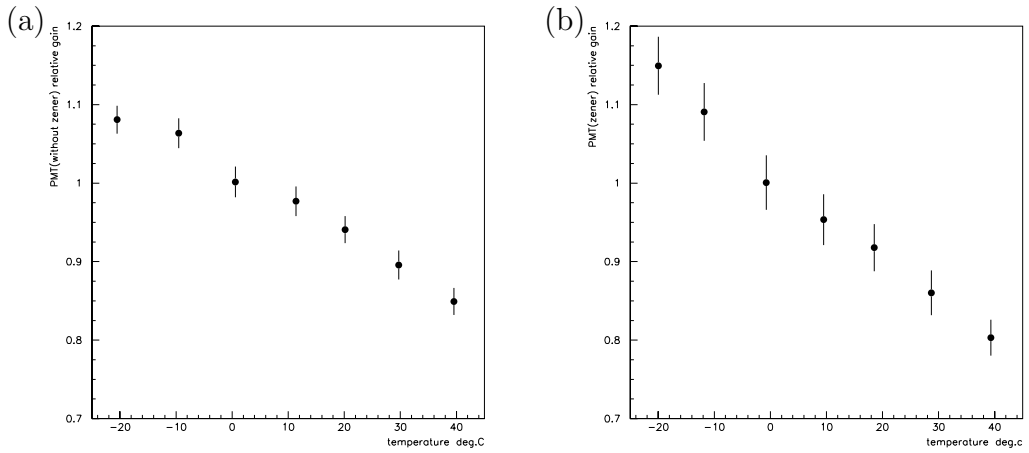

FIG. 2.12: (a) Measured temperature dependence of the relative PMT pulse gain for the ordinary bleeder (a) and for the hybrid bleeder (b).

Optimization of the filter thickness

We plan to use the optical filter, Schott BG3, passing photons only from 300 to 400 nm wave length (see Fig. 2.13 (a)). Since the transmittance of the filter depends on the thickness, we estimated its best thickness by referring to a signal to noise ratio (S/N).

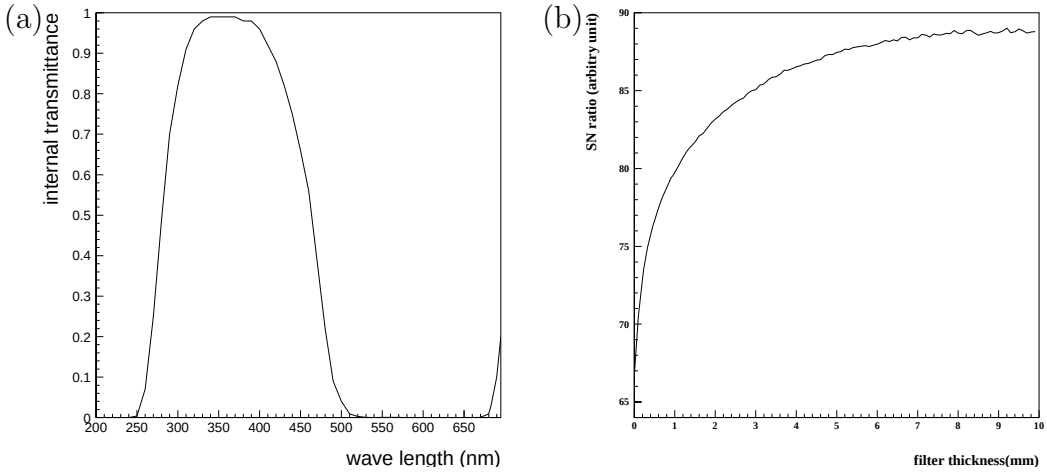

FIG. 2.13: (a) Internal transmittance of Schott BG3 filter of 1 mm thickness. (b) Signal to noise ratio as a function of the filter thickness.

The calculated S/N is shown as a function of the filter thickness in Fig. 2.13 (b). The S/N increases with the filter thickness, but is almost constant for the thickness more than 6 mm. We have chosen the filter thickness of 6 mm.

Uniformity of PMT cathode

The sensitivity of the PMT has a position dependence on its photocathode surface, reflecting the non-uniformity of the quantum efficiency and the amplification gain. Various factors such as the photocathode thickness, the irregularity of the focusing electric fields and the geometry of the first few dynodes affects the position dependence. We measured the 2-dimensional response of the PMT by scanning the pulsed LED source on the PMT window. The light source was mounted on a computer controlled XY stage. The spot size, as well as its relative positioning accuracy, was $\sim$ 1mm. The measured anode gain map is shown in Fig. 2.14.

As we observe from the sensitivity map, there is $\sim$ 3 mm insensitive region at the edge of the PMT glass envelope. Together with the physical gap between PMTs, it will form an insensitive band of 7–8 mm at the boundary of the PMTs. We are in the process of estimating the loss of fluorescence light and the effect on the event reconstruction by the simulation. At the same time, we are designing a wedge-shaped reflector to be placed at the PMT boundary such that the fluorescence light impinging on the insensitive band is reflected and guided to the central region of the photocathode. This minimizes the insensitive area and improves the uniformity of the imaging plane, thus minimizing the systematic error.

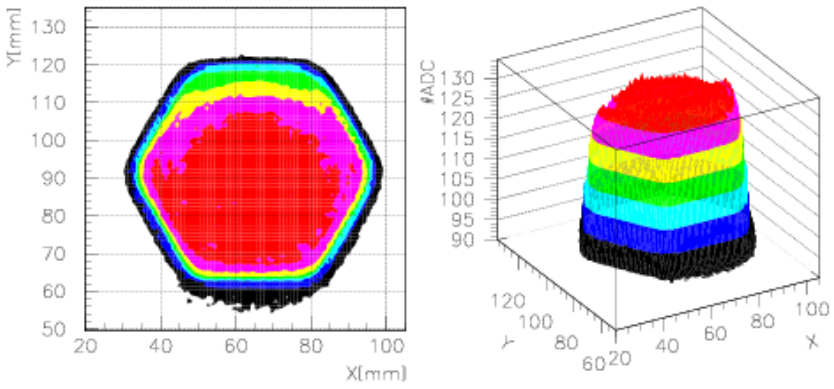

FIG. 2.14: Contour map of the measured anode gain (relative).

2.4.2 Calibration of PMT

YAP pulsar

We use YAP light pulsar ($YAlO_3 : Ce(YAP) + {}^{241}Am$) as the light sources for the PMT calibration. The details of this light pulser are described in references [82, 83, 84, 85]. Its luminous spectrum spans 300–400 nm (Fig. 2.15 (a)), and covers nicely the spectrum of air fluorescence. The structure and characteristics of the YAP pulsar (produced by Radiation Instruments and New Components Ltd.) is shown in Fig. 2.15 (b) and described in Table 2.4, respectively.

Table 2.4: Characteristics of YAP pulsar

Diameter	5.0 ± 0.2mm
Thickness	1.2 ± 0.2mm
Pulse Frequency	58Hz
Pulse Height Distribution	FWHM 5.5 %
Peak Wave Length	370nm

UV LED

The second light source is the UV LED (Nichia NSHU590E), whose characteristics are described in Table 2.5. This light source has been used as a simulator of the night sky background when we measured the characteristics of the PMT.

Table 2.5: Characteristics of UV LED (Nichia NSHU590E)

DC voltage	3.9 V
Emission Power	750μW
Peak Wave Length	370 nm
FWHM of the Spectrum	12 nm

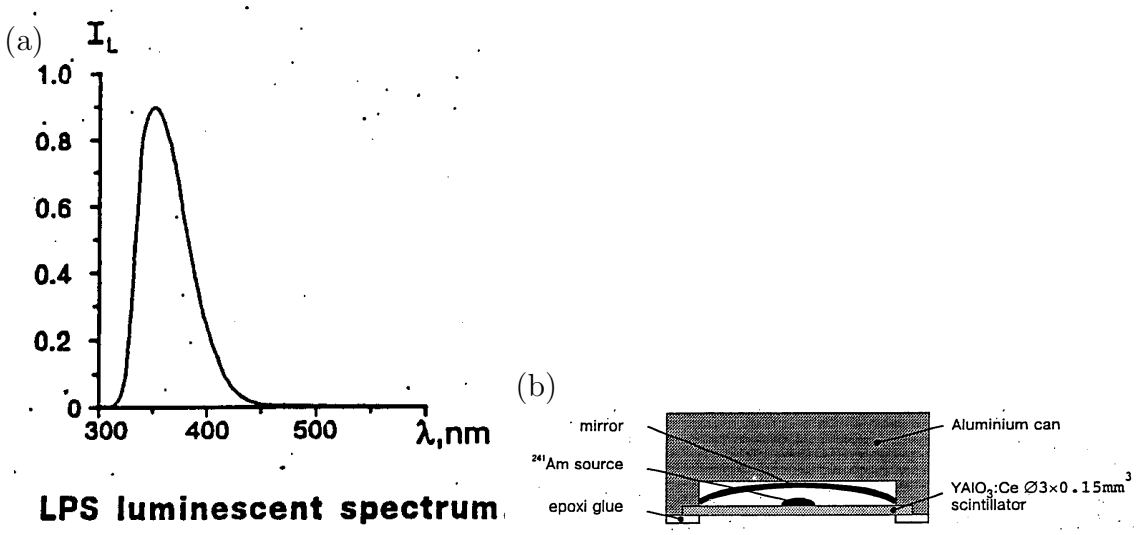

FIG. 2.15: Spectrum and structure of YAP pulser.

2.4.3 Design of PMT Camera

The PMT camera is to be made as a closed box to avoid the PMT and electronics be damages by the sand and dust of the environment. In addition, the ambient temperature varies from -10 to 40°C, and the electronics inside the camera box is a heat source of 1.7 kW (estimated with a safety factor of 2, see Table 2.6 for detail). To cope with this problem and guarantee a stable operation of the camera, it is imperative to equip the temperature control system inside the camera box.

Table 2.6: Power consumption in a PMT camera box. The values are measured for the prototype circuits.

parts	power	
CSI-hybrid	1.75	W/ch
ADC+DSP	0.75	W/ch
Main	5	W/16ch
Front-end circuit	720	W/256ch
HV distributor	120	W/256ch

The overall design of the PMT camera is shown in Fig. 2.16. Each PMT is inserted to an accurately machined hole of the aluminum support plate and fixed with 4 screws as shown in Fig. 2.17. The front of the camera is covered with an optical filter, Schott BG3, attached to the frame, which can be opened for the access to the PMT for the maintenance. A computer controlled XY scanning stage is attached to the filter frame carrying the YAP pulser for the calibration of PMT and electronics. The back of the PMT is covered by two doors, to which VME crates for the main digitizer/trigger board and HV distributors are installed. The inner wall of the box is covered with heat insulators.

A small air conditioning unit is installed inside the box for cooling the electronics. The outer dimension of the box is 1300 mm × 1150 mm × 905 mm and the total weight of the camera including the PMTs and the electronics circuits is about 250 kg. Since most of the digitizer and trigger electronics are installed inside the camera box, the number of cables coming out from the camera is much reduced, and only a few optical fiber cables and power supply cables are to be connected to the camera box.

(a)

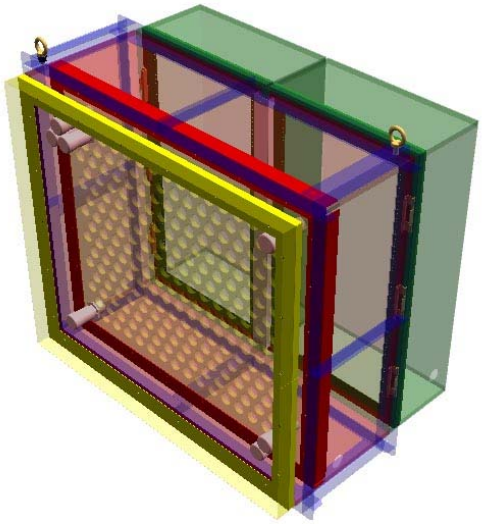

(b)

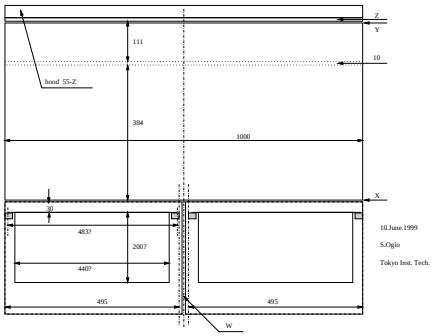

FIG. 2.16: (a) PMT camera. (b) Plan view of the camera box. The dimensions are in mm.

(a)

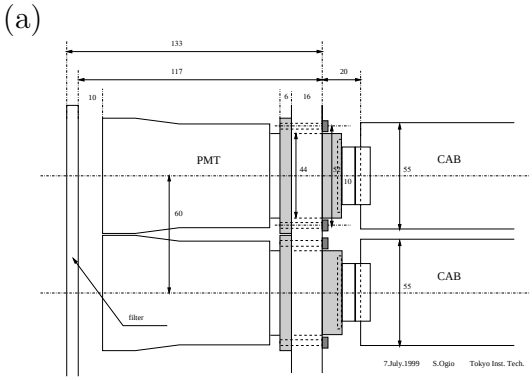

(b)

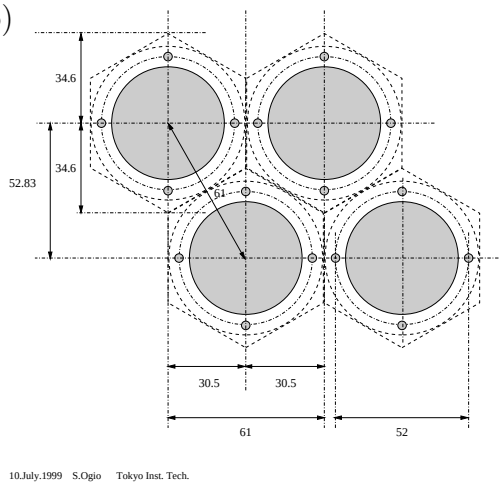

FIG. 2.17: (a) Side view of the PMT and the supporting plate. (b) Front view of the support plate.

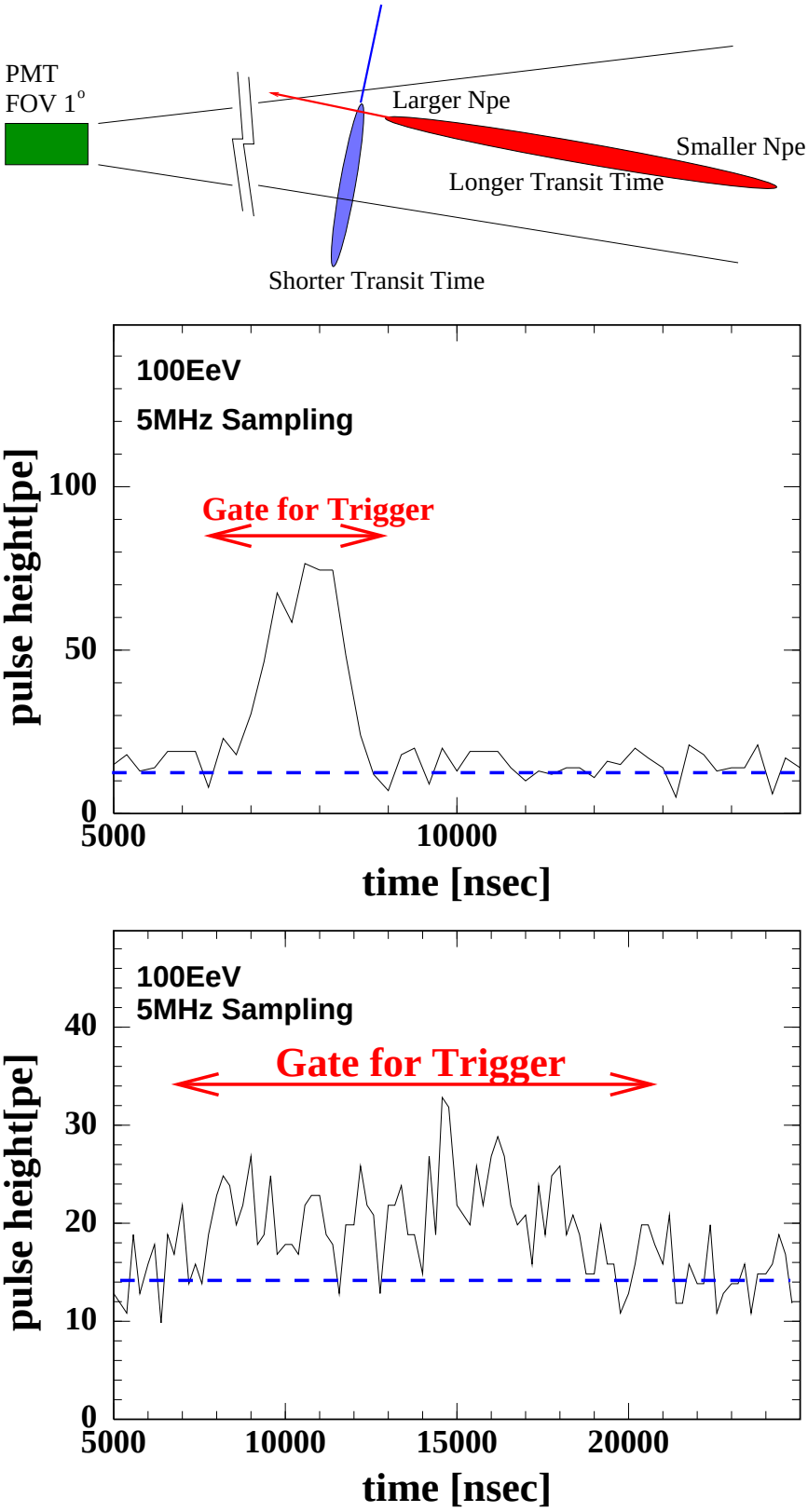

FIG. 2.18: Typical PMT signals for different event geometry.

2.5 Electronics and Trigger

2.5.1 System requirement and overview

The strength and duration of the air-fluorescence pulse depends largely on the geometry of the event, as illustrated in Fig. 2.18. A well defined short pulse with high amplitude will be produced by the nearby air shower traversing the telescope's line of sight perpendicularly. A signal from the distant event with running away configuration, on the other hand, will be widely spread and is difficult to be separated from the night sky background. The recording of the signal time profile becomes increasingly important for events with a long duration, for which most of the information to determine the geometry (particularly the direction) is included in the time information. Therefore the continuous digitization and recording of the signal wave form is much preferred compared to the analog integration of the signal with a fixed gate width, or a fixed time constant.

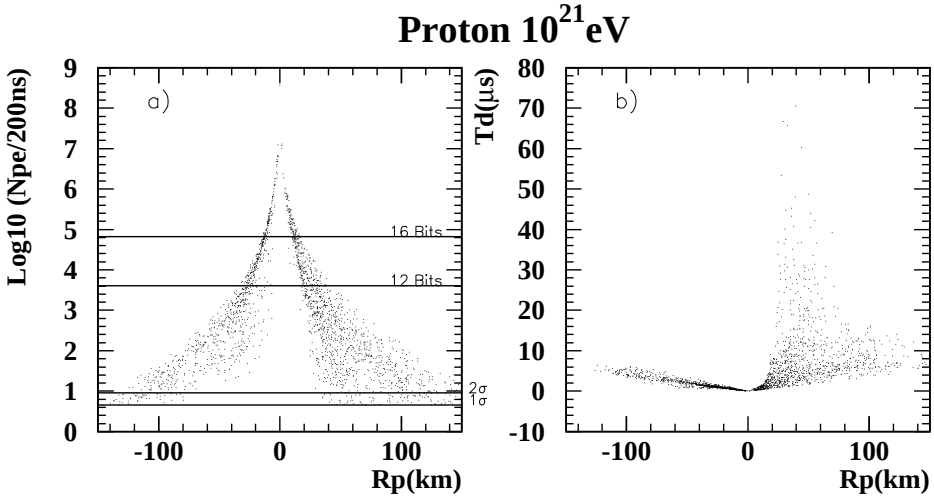

FIG. 2.19: Maximum number of photoelectrons per 200 ns time bin for one PMT versus impact parameter R_P of the event (left). Signal duration versus R_P for the same PMT (right).

We performed a Monte Carlo study to estimate a required dynamic range of the electronics. In Fig. 2.19, we show scatter plots of the maximum number of photoelectrons contained in 200 ns gate time v.s. its impact parameter for the 10^{21} eV proton air-shower events. The rate of events in which at least one of the PMTs exceeded the ADC dynamic range of 12 bits (16 bits) is roughly 30% (10%) assuming a LSB of digitization is taken equal to one photoelectron in 200 ns. The difference between 12 bits and 16 bits increases as we tighten the event selection cut. If we require more than 10 PMT hits with more than 2 σ significance level above the background, the overflow rates are 12% and 58% for 16-bit and 12-bit dynamic range respectively. This concludes the dynamic range of 16 bits is needed for the ADC system to be unsaturated up to 10^{21} eV event. The requirement can be alleviated if we take a LSB sensitivity to be at significantly lower level, say at the level of the night sky background ($\sim$30 photoelectrons in 200 ns). But the monitoring of

the background level will be unreliable for such a system, and a signal separation from the background will be much deteriorated for the online and offline analysis.

The duration of the signal for the PMT with the highest number of photoelectrons is plotted in Fig. 2.19 against the impact parameter of the event. It indicates some events can generate fluorescence signal as long as 70 μs. An elaborate and flexible algorithm will be required online and offline to identify a signal and maximize the signal to noise ratio (S/N). We checked that the 25.6 μs time window is practically sufficient for the signal finding for the triggering purpose. The necessary time depth for the event recording can be determined for each event by the DSP software.

A good S/N will allow us to trigger and analyzed lower energy events. Given D=1.6m, d=14cm, and S/N=4 for Fly's Eye and D=3m, d=6cm, and S/N=2 for TA, we will be able to decrease the threshold energy for detection down to 10^{16} eV, which is about an order of magnitude smaller than that of Fly's Eye. Here the D is a mirror diameter and d is a PMT diameter. This would allow us to study cosmic rays in this energy region and specifically opens up a possibility of detecting the neutrinos from AGN.

Monte Carlo studies indicate that many showers that trigger one station will also be seen by several neighboring stations. Even if the neighboring telescope does not see enough of the light to trigger on that shower, there will be information present useful for the stereo reconstruction of the event. The system of broadcasting triggers seen by one detector to its neighboring detectors will be thus important. When a trigger occurs in one detector, the data of its neighboring detectors will be examined and any hits found will be written into the data stream.

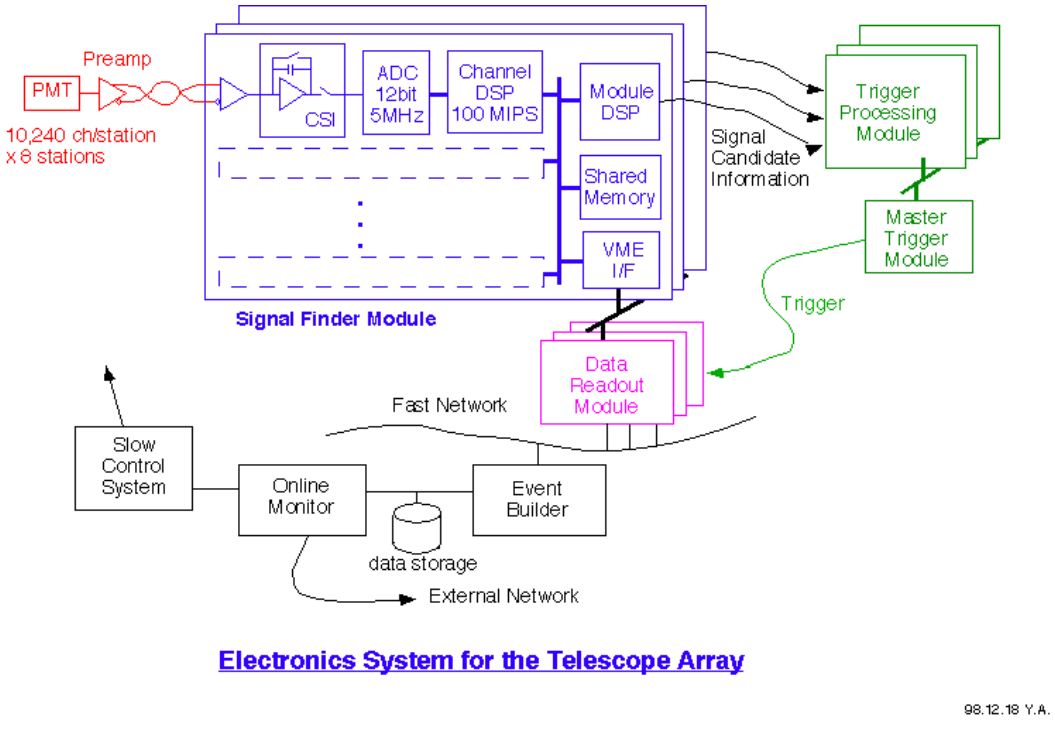

FIG. 2.20: Block diagram of the TA online system.

A baseline design of the TA signal digitization, trigger and data acquisition was drawn to satisfy above conditions (see Fig. 2.20). Its main features are summarized below;

(1) AD conversion with 12-bit resolution and 50 MHz continuous sampling using a pipelined ADC chip.

(2) 16-bit dynamic range using H/L 2-range scheme at the front-end charge sampling LSI (custom development). Here LSB sensitivity is taken equal to one photoelectron in 200 ns time window.

(3) on-flight software recognition of fluorescence signal by the DSP attached to each channel.

(4) generation of trigger in 3-dimensional space; XY (camera) coordinates and T (time) coordinate by software.

(5) exchange of trigger information between stations (intersite trigger).

In Chapter 4, we present the expected performance of TA obtained by the Monte Carlo simulation, and items (1)–(3) above have been taken into account in this simulation.

2.5.2 Front-end Electronics System

The front-end electronics for TA is one of the most critical elements to achieve a large aperture of the detector and lower threshold of cosmic ray primary energy. In the pioneering work of the Fly's Eye detector, analog sample-and-hold circuit with a slow AD converter [86] was adopted. In the subsequent HiRes detector, 8-bit flash ADC was introduced with additional analog sum measurements to circumvent the effect of over range [87].

A new pipelined ADC technology and a wide spread of digital video system enable us to use a fast and wide dynamic range ADC for all channels. The pipelined ADC is fabricated in a CMOS process, and it has superi or characteristics of low power, low cost and high speed. A 12-bit 5-MHz sample ADC is commercially available in less than $7.

While the fast ADC system could give us more information on air shower, it increases data size almost 100 times. Thus a large bandwidth is required in data acquisition system. Furthermore, to maximize the merit of the fast digitization, it is indispensable to process the data in real time to increase signal to noise ratio. This is particularly important in the fluorescence measurement since the signal wave form varies greatly depending on the zenith angle and the impact parameter.

To process the digital data in real time, a large processing power is required. Fortunately, recent progress in digital products introduces high-performance, low-cost Digital Signal Processors (DSPs). There are several DSPs, performances of which are more than 100 MIPS and the price is about $6. By using these DSPs we will be able to search optimal signal width for fluorescence signal in real time.

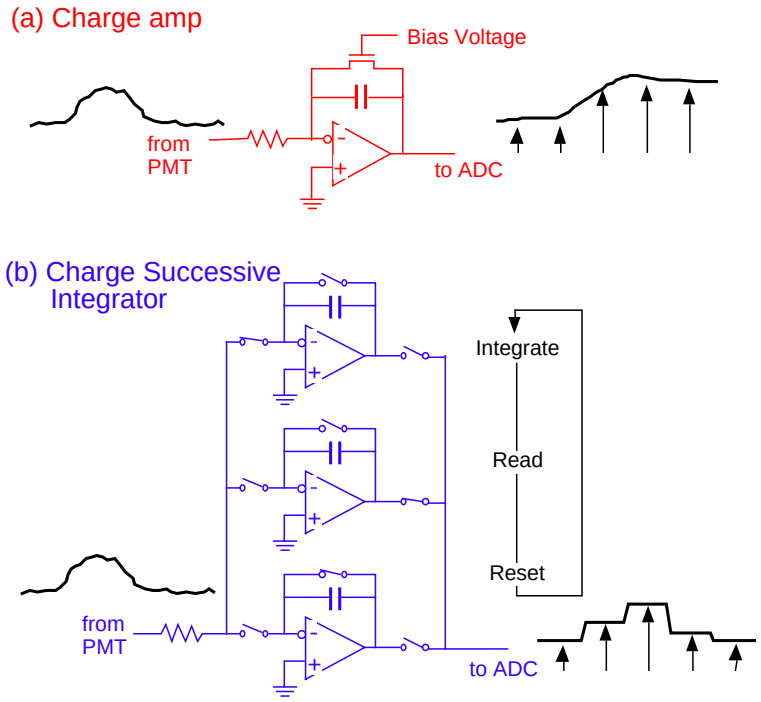

Charge Integration Methods

FIG. 2.21: Schematics of Charge Successive Integrator.

Charge Integration

A charge integration method is essential in designing a calorimetric measurement. To implement the baseline design, we are developing a Charge Successive Integrator (CSI) LSI. (Fig. 2.21). It has 3 rotating capacitances which serves for the integration, signal output to ADC, and reset successively for each 200 ns. Required signal range for the CSI (and PMT) is summarized in the following lists. Here we assume a PMT amplification of 8×10^4 and 20 pF storage capacitance for the CSI. The LSB in the low range (a unity gain before CSI) corresponds to 1 photoelectron in 200 ns. The maximum signal corresponds to 65,536 ($=2^{16}$) photoelectrons in 200 ns and is detected in the high range (a gain of 1/16 before CSI).

98.12.18 Y.A.

- **Least count sensitivity:** A 10 ns wide (square) pulse from PMT has a (peak) current of 1.28 μA and a total charge of 13 fC. This is equivalent to 0.6 mV of stored voltage on the CSI capacitance (low range used).

- **Full scale sensitivity:** 65,536 photoelectrons in 200 ns corresponds to 4.2 mA current from PMT for the same duration. The total charge from PMT is 840 pC and this becomes 2.6 V on the CSI capacitance (high range used).

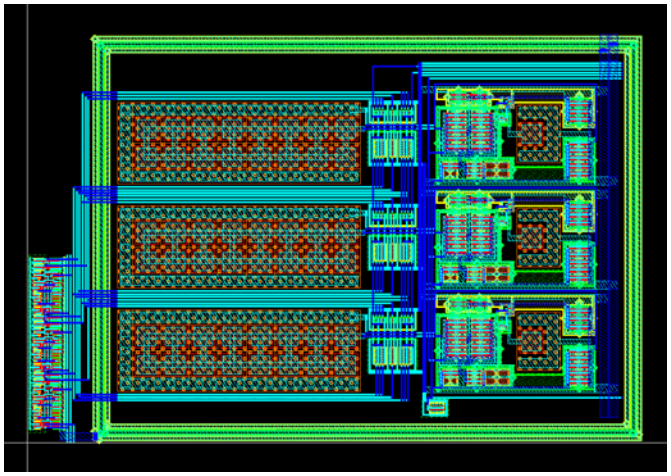

FIG. 2.22: Layout of the test CSI cell designed in 0.6 μm CMOS technology. In this particular cell, 12 pF integration capacitors were used.

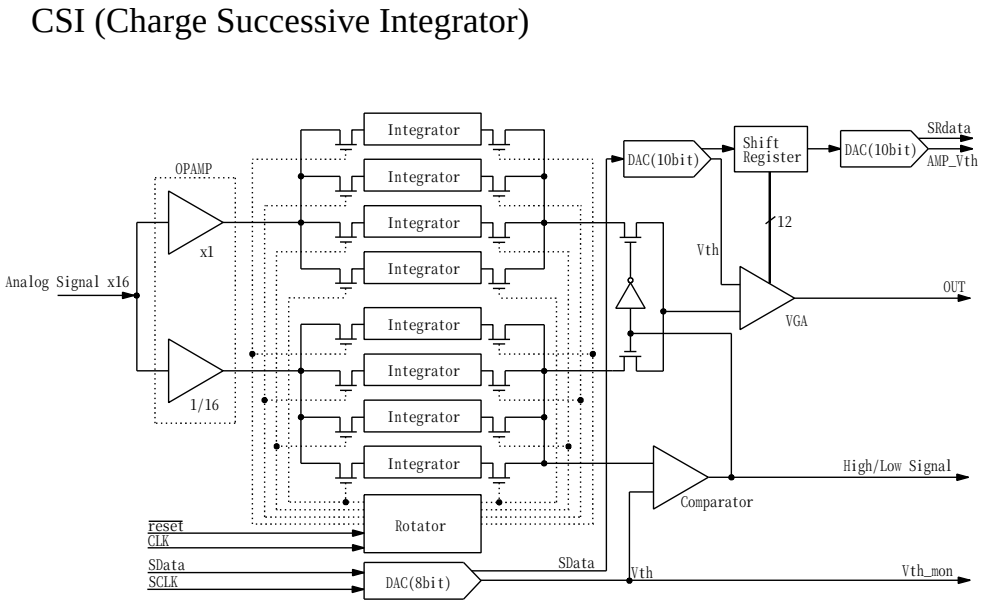

FIG. 2.23: Schematic of the CSI with two-range scheme.

– **Night sky background:** We assume 30 photoelectrons in 200 ns. This is equivalent to a continuous current of 1.9 μA from PMT and 19 mV stored on the CSI capacitance (low range used).

The CSI will be fabricated in a CMOS technology. In this technology the value of the capacitor matches in 0.1% level, and no correction will be necessary. But the area of CSI-VLSI limits the integration capacitance less than ∼200 pF. A test CSI chip using a 0.6 μm single-poly, triple-metal CMOS process was fabricated (Fig. 2.22) at Rohm Co. through VLSI Design and Education Center (VDEC, Univ. of Tokyo) multi project ware service. While the prototype CSI chip includes only one range of circuit, final chip will implement 2-range scheme as shown in Fig. 2.23.

Pipelined ADC

Recent progress in digital video system brings a new high-speed, large dynamic-range, low-power, low-cost ADC. Technique used here is called pipelined ADC (Fig. 2.24). The ADC has many pipelined stages, and digitization of only one or two bit is done at each stage. This ADC is fabricated in similar process used in CMOS digital LSIs and there are very little analog elements in the chip. A digital error correction technique is usually employed to achieve a high precision.

We are presently using Burr-Brown ADS803 and its power consumption is only 115 mW. The ADC has 12-bit dynamic range and 5 MHz-conversion rate.

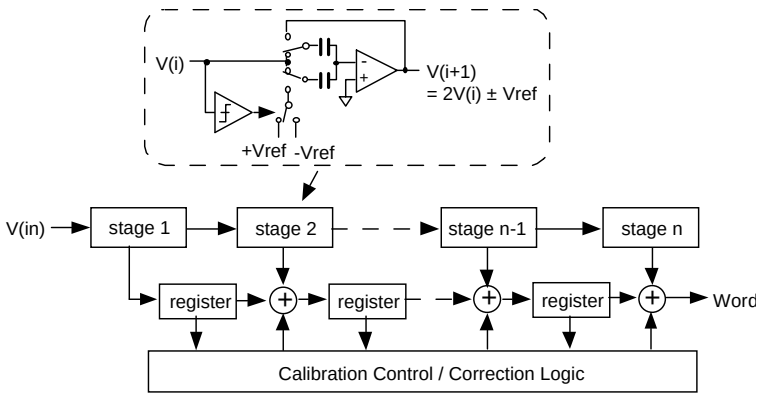

FIG. 2.24: Pipelined ADC.

DSP

The ADC converts a PMT signal continuously at 5 MHz frequency, and 12-bit data together with additional information such as a range and an overflow bit are successively stored into

the memory of dedicated DSP. A high-performance DSP is needed to run a signal finding algorithm in real time on the stored data. We are presently using a TMS320C549 DSP from Texas Instruments. This DSP runs at 100 MHz, and many operations can be performed in one cycle. The C549 has 3 internal data bus and one program bus, and consists of 6 stage pipelines. It contains 32k word internal memory that is enough for our application. The DSP consumes only 100 mW/chip. Since the ADC generates 12-bit data every 200 ns, there are 20 cycles for one data in average. We set 25.6 μs time window for finding a signal. Since this window has 8.5 μs overlap with the next window, a total of ~1,700 DSP cycles (17.1 μs) can be executed for 128 data words (25.6 μs) to identify the fluorescence signal.

An example of signal finding algorithm at DSP is illustrated in Fig. 2.25. The program looks for a set of signal edges T1 and T2 which maximize the S/N or $Q/\sqrt{BG}$. According to a Monte Carlo study, the charge resolution by this algorithm is 50 % for 10 photoelectrons (Q=10) and 20 % for 50 photoelectrons.

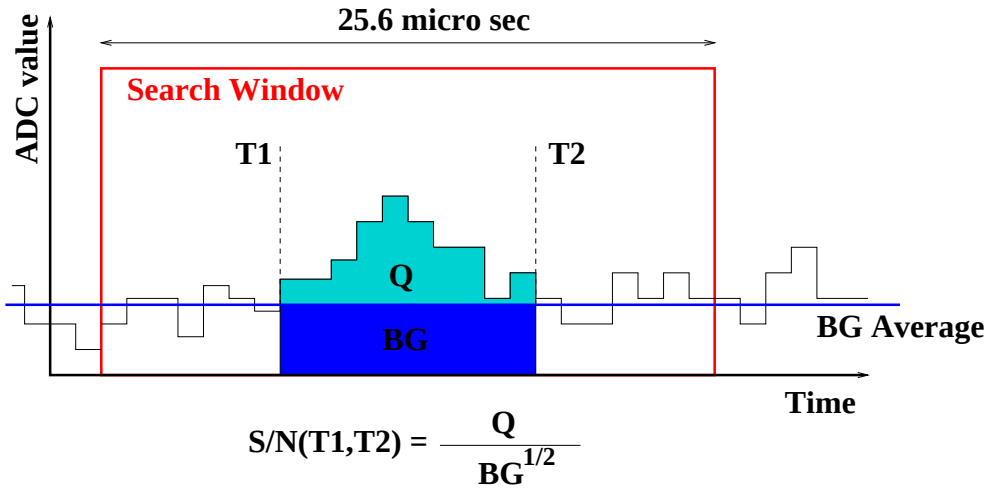

FIG. 2.25: Signal finding algorithm.

2.5.3 Signal Finder Module

A Signal Finder Module, which contains the front-end CSI, ADC and DSP, has been prototyped (see Fig. 2.26 and 2.27). The schematics of the module is shown in Fig. 2.28. The module is implemented in a 6U VME board and contains 16 channels. The gain and offset of each channel can be corrected before the CSI with 16-bit DAC. The single range hybrid version of CSI is used for the present prototype and it will be replaced by the 2-range LSI version in future.

Data transfer between the ADC and the DSP internal memory will be done through an 8-bit host port interface of the DSP with a maximum speed of 20MB/s. ADC data are automatically transferred to internal circular buffer without DSP intervention (see Fig. 2.29). The size of the circular memory is 2k words, thus the data can be stored in the memory up to 400 μs (200 ns $\times$2 kW). For the intersite trigger which requires a longer latency than 400 μs, a data copy operation is required to the external memory.

FIG. 2.26: Prototype signal finder sub-board for one channel.

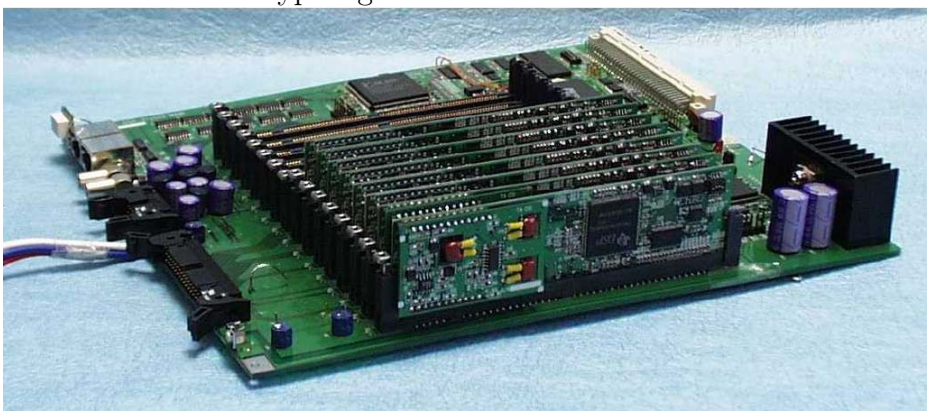

FIG. 2.27: Prototype for the main module of signal finder. The height of the module is 6U but the depth of the module is extended to 26 cm.

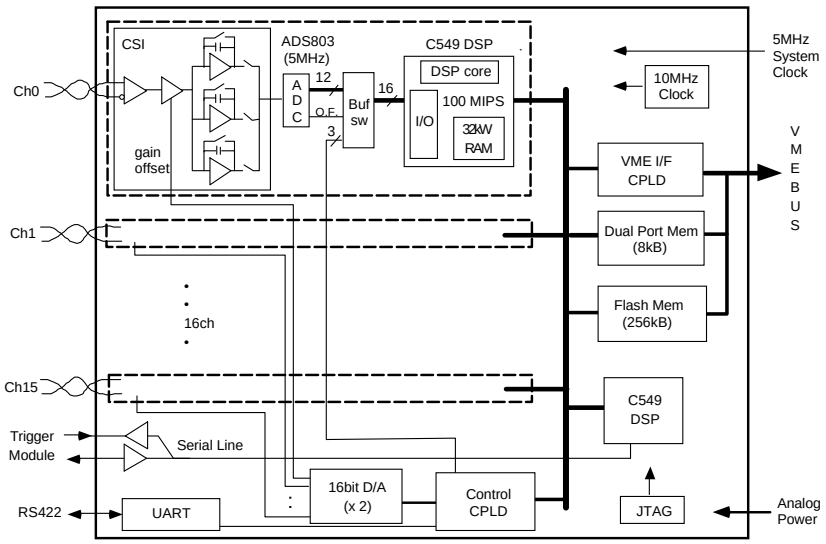

FIG. 2.28: Block diagram of the 16-ch prototype Signal Finder module. The module is implemented in a 6U VME board.

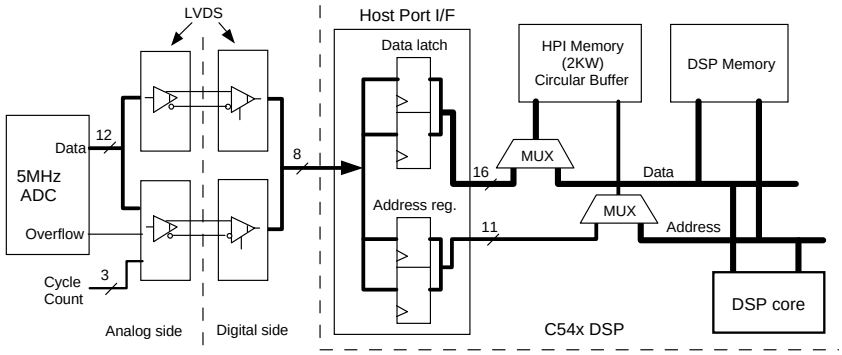

FIG. 2.29: ADC to DSP interface.

Between the ADC and the host port, 12-bit data and an overflow bit are transferred. In addition, 2 bits are transferred to a 2-bit counter, which is used to check the data sequence. Last one bit is reserved for data flow control which is used in DSP software. This is realized by two 8-bit data transfer cycles. In order to avoid the interference of the digital signal to the sensitive analog circuit, LVDS (Low Voltage Differential Signaling) drivers/receivers are used for the digital signal transfer.

All the individual DSPs are controlled by another DSP, which collects the processed information (T1, T2, Q and S/N, etc.), and send them to the trigger module through its serial lines at 50 Mbps. An easy-to-use commercial PC tool can be connected to the module via JTAG boundary scan port for debugging and monitoring of the DSPs. A dual port memory of 8 kB is used to exchange the data between the module and a VME master module. A Flash memory of 256 kB is included to store program and parameters. The whole system can be synchronized by using an external system clock of 5 MHz.

2.6 Intersite Trigger System

A schematics of the intersite trigger system, being implemented as the radio link between a pair of HiRes stations, is shown in Fig. 2.30. In this diagram information flows from left to right. After a trigger is formed, the information to be sent to neighboring detectors is encoded in an interface card, passed to the radio transmitter, and sent to the mountain where the neighboring detector is located. At that site the information is decoded by a second interface card and passed to the flash ADC readout system so the data there can be examined for hits from the triggering shower. This figure shows a single, one-way radio

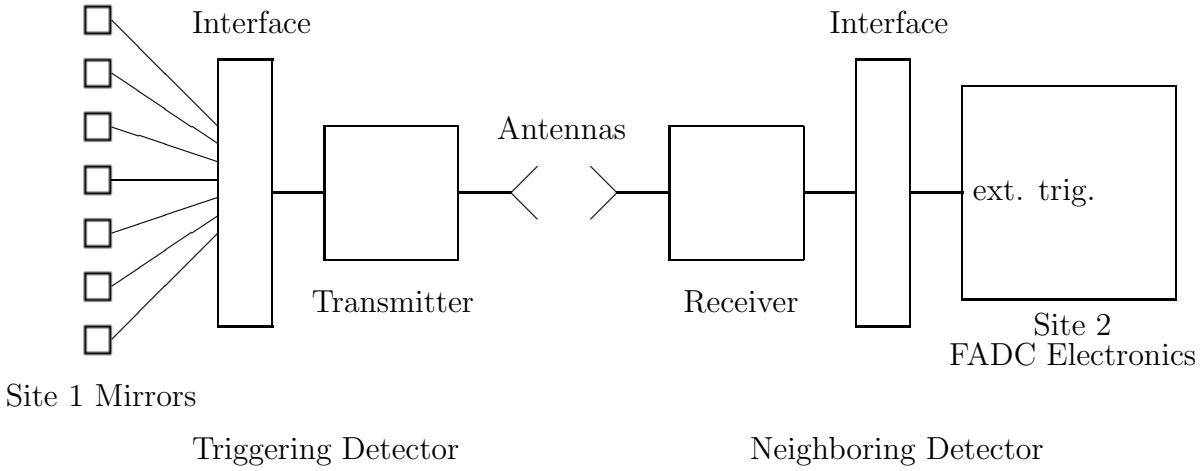

FIG. 2.30: Block diagram of intersite trigger

channel, but the radios we will use for TA will be two-way, with separate frequencies, transmitters, and receivers for each direction. Each element of the intersite trigger, connecting two sites, will cost about $22,000.

The information passed between two HiRes sites consists of a signal at the time of the trigger plus a 5-bit word which is the number of the triggering mirror. The Telescope Array data-collection system will allow us to transmit more information for the intersite trigger. We feel that the most useful information will be the length of the track seen at the triggering site. Having this information will allow the neighboring site to grade triggers and, if the data rate is momentarily high, only pick the most interesting intersite triggers to act upon.

We intend to connect all TA stations by the optical fiber network. One of the important purposes of the fiber link is to use it for the intersite trigger. We continue to study optical fiber and radio communications for the intersite trigger.

2.7 Data acquisition and online system

2.7.1 Data acquisition

An event size distribution of one TA station for the air shower events with energies above 10^{19} eV is shown in Fig. 2.31. The size is less than 1.5 kB for 90 % of the event. The event rate of air shower with energy more than 10^{16} eV is less than 0.3 Hz per station. Even we assume a maximum trigger rate of 10 Hz caused by the Cherenkov light of low energy showers and muons, the maximum data transfer rate is 15 kB/s. This rate of event building can be comfortably achieved by the Ethernet technology.

An overall scheme of TA event building is shown in Fig. 2.32. Once the signal finder module receives a DAQ request from the trigger, the stored data in the internal memory of

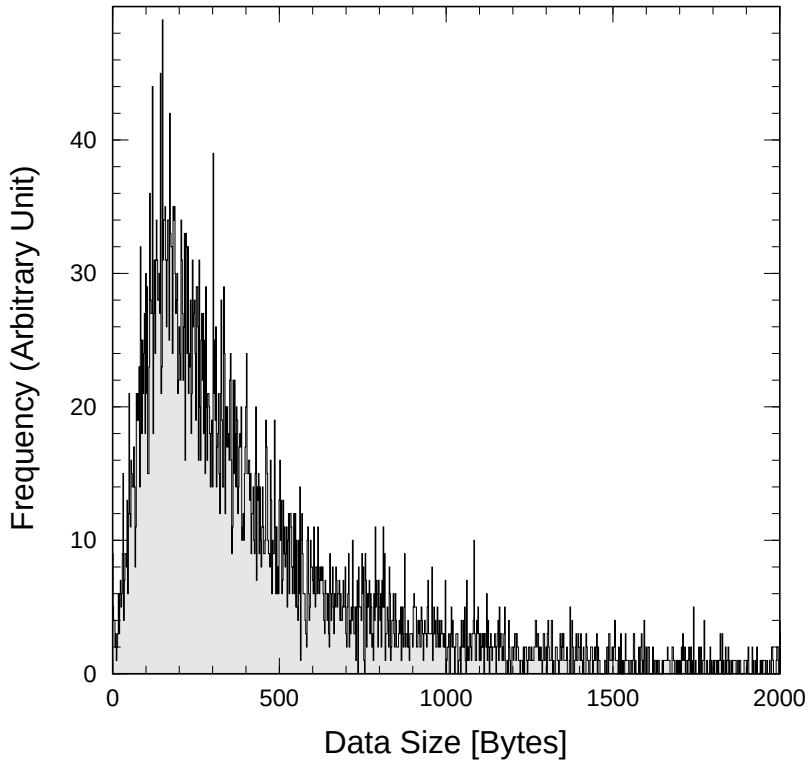

FIG. 2.31: Data size for air shower event.

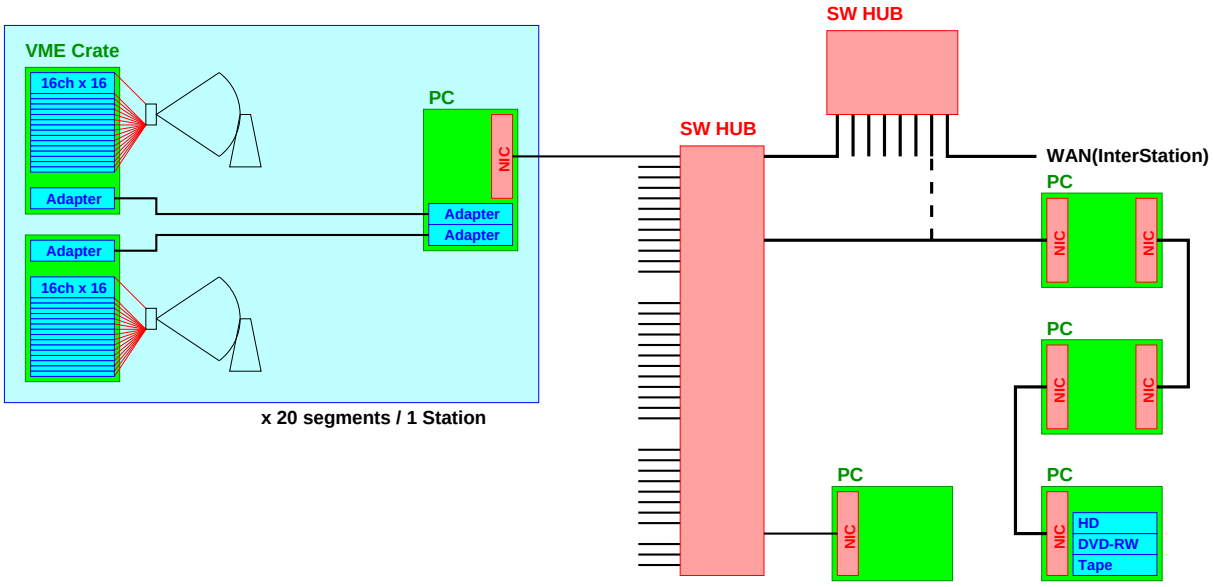

FIG. 2.32: TA data acquisition system.

DSP are sent to the event builder computer through a VME bus and VME/PCI adapter. Data from 512 channels (two telescopes) are gathered into one VME crate consisting of 8 units of 64ch signal finder modules and 1 VME/PCI adapter card. The adapter will send the combined data into 1 front-end network PC. The switching HUB is to merge the fast-ethernet data packets from 20 network PCs into the event builder PC by Giga-bit ethernet technique. An additional 2 PCs connected by the Giga-bit ethernet LAN will form a DAQ computing farm. The DAQ farm is responsible for the event building, filtering, quick online analysis and monitoring, and the maintenance of online calibration database.

2.7.2 Slow Control

In addition to the data acquisition function, the online system will be responsible for the slow control function such as;

(1) gain calibration of electronics.

(2) high-voltage monitor and control.

(3) atmospheric monitor.

(4) environmental supervising.

2.7.3 Structure of online software

The TA data acquisition (DAQ) system should handle 10,240 signal channels at each station. To increase the data taking efficiency and the data quality, a DAQ system with high degrees of homogeneity, flexibility and scalability is required. We are now building our own DAQ system by modifying CASCADE DAQ system [88], a multi-processor real-time data-acquisition system for High Energy Physics (HEP) experiments developed at CERN by the ECP-DS group.

The concept of a unit construction system has been followed. The basic software unit, called the *stage*, and the stage connection unit, called the *inter-stage link*, have been defined. Plugs for special-purpose connections like event monitoring, run control and experiment specific functions are provided. This approach allows for easy task distribution and their communications in a distributed system using a variety of operating system and physical hardware connections.

The stage is the fundamental construction of the DAQ system. It performs the basic functionality of a general single-processor, single-process, data-acquisition kernel. It is structured and parameterized so that several stages can be grouped together to form subsystems such as event builders or farms.

The stage is organized to perform several threads of execution. This allows operations to take place concurrently on different events so that the stage can deal with a number of input and output ports at their individual rates. The thread scheduling sequence in the stage is performed on a priority basis and has no fixed sequence. This is opposed to the flow of a particular event through a stage, which passes from one thread to the next in a

well defined order. Each thread corresponds to a given operation to be performed on an event or to a control action to be done on the stage.

Two consecutive stage units in the data-flow topology are linked by the DAQ connection unit, the inter-stage link. Communication between two stages is initiated by the dispatch phase of the upstream stage, which triggers the input phase of the downstream stage by sending it a signal. The protocol includes exchange of a message containing the event descriptor followed by the transfer of the event data. An acknowledge message is sent by the downstream stage to the link-acknowledge phase of the upstream phase once the event has been successfully transferred.

A high-level interface and a handshake protocol has been specified for the inter-stage link communication. They have been implemented on a number of hardware and software platforms.

2.7.4 Run Control

The run control facility is comprised of two processes running on a UNIX PC: the run control engine (NRC) and the human interface (XHI). NRC is a modular, general-purpose control program allowing complex data-acquisition systems to be modeled in an object-oriented way. It is based on a system originally designed by the OPAL [89] experiment and adapted in collaboration with NOMAD to better suit their needs. Operator interaction with the data-acquisition system is achieved by XHI, an X11/Motif program which provides a run time configurable graphical interface including menus, dialog boxes and various types of display panels.

NRC is a process controlling DAQ units such as stages, recorders, monitoring programs and user specific processes. Its main purpose is to provide synchronization between various DAQ units and to hold their respective states. Within NRC, each element is described in a uniform way as a Finite State Machine (FSM). A FSM is an object having a predefined set of allowed states and allowed transitions between these states. Since DAQ units are external to NRC, they are represented by internal FSM correspondents. A hierarchy of internal FSMs can be introduced to control subsets of the entire DAQ system.

Communication between NRC and the external FSMs is based on NIC, the TA Network component package via TCP/IP. The XHI, although a special object, communicates with NRC in the same way as the DAQ units. The NRC master is the network server and the external DAQ units are the clients, which can connect dynamically to the server. NRC maintains the states of all the data acquisition components as well as run time parameters in an external ORACLE data base. A run control domain is defined by an identifier which is used by NRC and the connected FSM's. In a given domain each object is identified by its unique ASCII name. More than one instance of the run control facility may be running at a given time using different addressing domains. For example a full production run can coexist with the test or calibration of a particular sub-system. When the NRC program is stated, the configuration information is read from an ORACLE data base. This information is used to build the run control data structures: the FSM definitions, default state of objects, state transitions, elements of the graphical user interface and run time parameters. A NRC user library allows for easy preparation of an external DAQ unit using three function calls.

2.8 Computing

Computing facility is used for a data management, physical/technical analysis, simulation work and any related computing tasks necessary for the TA experiment. This facility has to furnish enough ability for computing and data storage to all researchers, engineers and students in TA experiment working on-site and at each collaborating institute in Australia, Japan and USA through an established network.

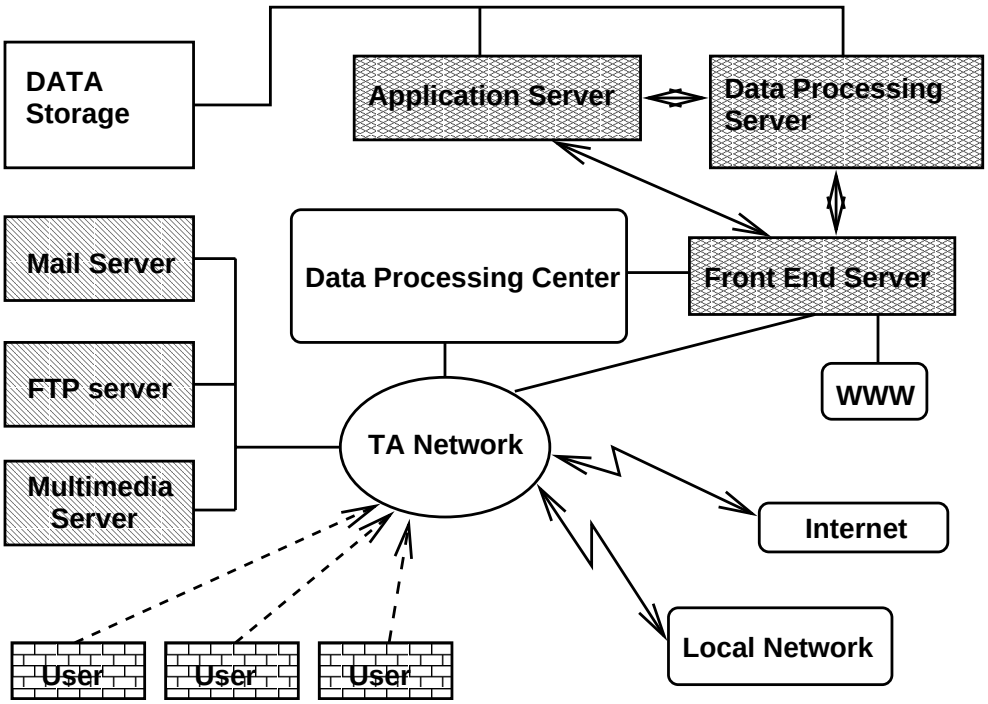

FIG. 2.33: Computing service of TA experiment.

A conceptual design of TA computing facility is shown in Fig. 2.33. It consists of two major servers; Data Processing Server and Application Server. **The Data Processing Server** consists of 8 work stations equipped with 667 MHz Alpha-21264 (dual processors) and unix based operation system. It is for a basic analysis of experimental data and simulation studies oriented for heavy CPU time load. This frame has 2000 GB hard disk system for the permanent data storage and temporary use. Also 5 Digital Linear Tape (DLT) drives are attached to the server for an additional on-line data storage and backup system. **The Application Server** is dedicated to the analysis of individual physical and technical problems oriented more for the I/O load and human interactivity. The analysis of atmospheric calibration data is an example of this. This server also consists of 10 work stations same with Data Processing Server, 4000 GB user disk area and 5 DLT drives.

The Front End Server is placed between two major servers and the user. It manages a user authorization and system related management/service tasks for the convenience of all the users. In addition, it will play an important role for the communication between the TA collaborators by offering a common notice board and Web-site services. Additional

servers for mail, FTP and a Multimedia will be installed in the system. A total of 15 terminal stations will be available for the local user of the facility.

For the system stability and safety, a UPS system with high capacity battery and a voltage stabilizer is installed in the AC power line. In case of a sudden power failure, all equipment will be shut down with a proper procedure before the ensuring time of 20 minutes expires. Computing and network system has to provide a high quality and reliable performance to carry out the experiment smoothly and to support user activity. Present design meets such demands on its ability, convenience and reliability.

Chapter 3

Atmospheric monitoring

3.1 Overview

The understanding of the atmosphere is essential to the air fluorescence technique of measuring particles with energies from 10^{17} eV to 10^{20} eV and beyond. The atmosphere is required for the primary particle to interact, the subsequent shower to develop, and the forward going Cherenkov light and isotropic ultra-violet (UV) light to be produced. Details of the UV light production yield details of the primary particle. The amount of UV light produced is proportional to the particle's energy. The shape and atmospheric depth of the shower profile contain information about the composition of the primary particle.

However, once the light is produced, the amount that reaches the optical detectors depends on how the light propagates between the shower and the detector. If the atmosphere were to somehow disappear just after the light was produced, the fraction of light reaching the detector would be a simple function of shower and detector geometry. Of course the atmosphere is always present; the benefit of light production that make experiments such as Fly's Eye, HiRes, and the Telescope Array possible is balanced by the challenge to understand the light propagation. The challenge increases for the next generation of experiments that plan to explore higher energies because the most interesting showers will be farther away from the detectors. For example, while the overall size of TA is larger than HiRes, the 10–30 km distances at which HiRes observes high energy events overlaps with the expected 20–40 km detector/shower separation expected for TA.

In order to maximize the performance, the TA experiment will be located in the same dry clear desert where relatively few aerosols are present. The west Utah desert has some of the clearest air in the world. Secondly the detector stations will be built on hills several hundred meters above the desert floor so that the optical detectors are above much of the ground fog and local dust. Finally, the experiment will include systems to monitor atmospheric clarity locally and throughout the detector aperture while the detector is collecting data. These systems will include artificial light sources, primary lasers, that fire beams of photons throughout the detector aperture. The same array of detectors that measure light from air showers also measure the scattered light from the artificial light sources. Changes in atmospheric clarity will change the amount of light observed from both the artificial light sources and the air showers. In this experiment, we anticipate that the techniques used at HiRes will also work for TA.

Continuing joint US and Japanese R&D efforts in atmospheric monitoring will enhance the tools available by providing independent cross checks and additional constraints. This R&D effort continues to evaluate other techniques including back-scatter LIDAR systems and systems to directly measure the horizontal attenuation.

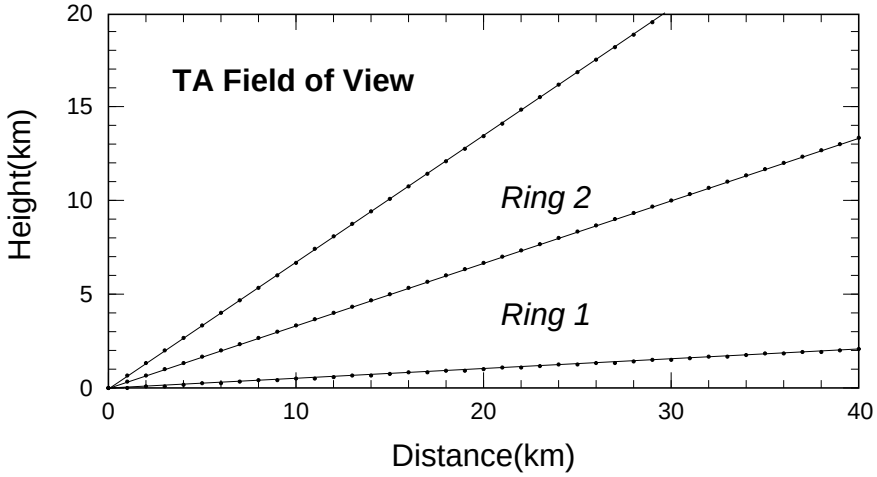

FIG. 3.1: Field of View in Height vs Distance for Telescope Array. The aperture of the Telescope Array detector (TA) extends approximately 30–40 km horizontally and 10 km vertically from the two detector stations. This field of view is similar to that of the HiRes experiment.

3.2 Components of the Atmosphere

For the purposes of an air fluorescence experiment, the atmosphere may be considered to have two parts: molecular and aerosol. The molecular component consists of the oxygen/nitrogen mixture. Although the density profile verses height varies slightly between winter and summer, the molecular component bounds the problem by providing the clearest, best-case, viewing conditions. The aerosol component consists of everything else such as dust, pollution, fog, clouds. This component is not constant, varying with time and location.

The molecular and aerosol components scatter the Cherenkov and scintillation light. There is also a third component, ozone, that absorbs light but its effects are negligible at the wavelengths of interest. The scintillation light produced by air showers falls in the 300–400 nm wavelength range [90] , just below the blue end of the visible spectrum.

The heart of the atmospheric monitoring problem for air fluorescent experiments is to monitor the distribution of aerosols in the detector aperture when data is being collected and to understand how light propagates through them. Specifically, one needs to know two quantities.

– The transmission coefficient between the shower and the detector is required to determine the shower energy and profile from the measured signals.

– The scattering probability as a function of scattering angle is needed understand the amount of scattered cherenkov light reaching the detector to that it can be subtracted from the fluorescence part of the signal.

These quantities can be extracted from measurements of laser and "flasher" shots fired through the detector aperture. Two approaches are possible. One uses select geometries to deconvolve the effects of aerosol scattering and extract the transmission. The second fits an aerosol model to the observed data to determine the model parameters. These parameters include a horizontal attenuation length, an aerosol scale height, and a scattering dependence or phase function.

3.2.1 The Molecular Component

The molecular part can be described analytically by the Rayleigh scattering theory. In this treatment, the nitrogen and oxygen molecules are treated as dielectric spheres that are much smaller than the wavelength of the incident light. This theory has several consequences that are important to fluorescence experiments. The probability for scattering increases rapidly as the wavelength decreases, proportional to $1/\lambda^4$. For more distant showers, the longer wavelength end of the spectrum, i.e., the 391 nm line, will be enhanced relative to the shorter wavelengths, i.e., the 337 nm line. The amount of light scattered at different angles varies by only a factor of two and is forward/backward symmetric, proportional to $1+\cos^2\theta$.

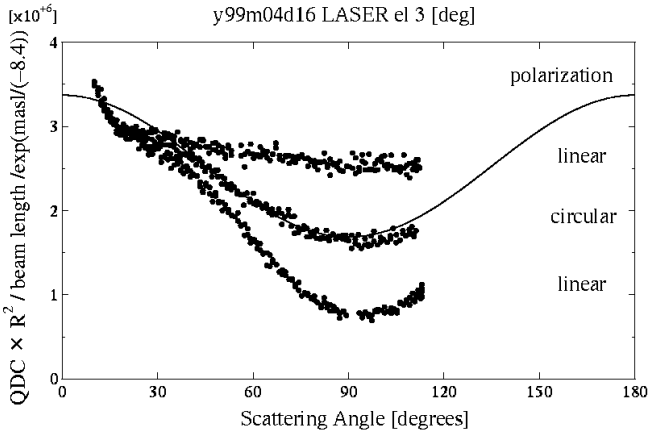

FIG. 3.2: Measurements by the USTA steerable telescope at Cedar Mt. The distributions show the effects of different polarizations from the HiRes steerable laser 20 km distant.

Molecular scattering effects have been observed by HiRes [91] and by the Cedar Mt Telescope [92] by measuring scattered light from linearity polarized laser beams. Figure 3.2 shows these measurements for a set of shots measured by the USTA telescope at Cedar Mt for two orthogonal linear polarizations and circularity polarized light. For this measurement the beam was fired nearly horizontally from the Camel's Back site 20 km distant. Except for small scattering angles where aerosols diminate, the observed phase function is in agreement

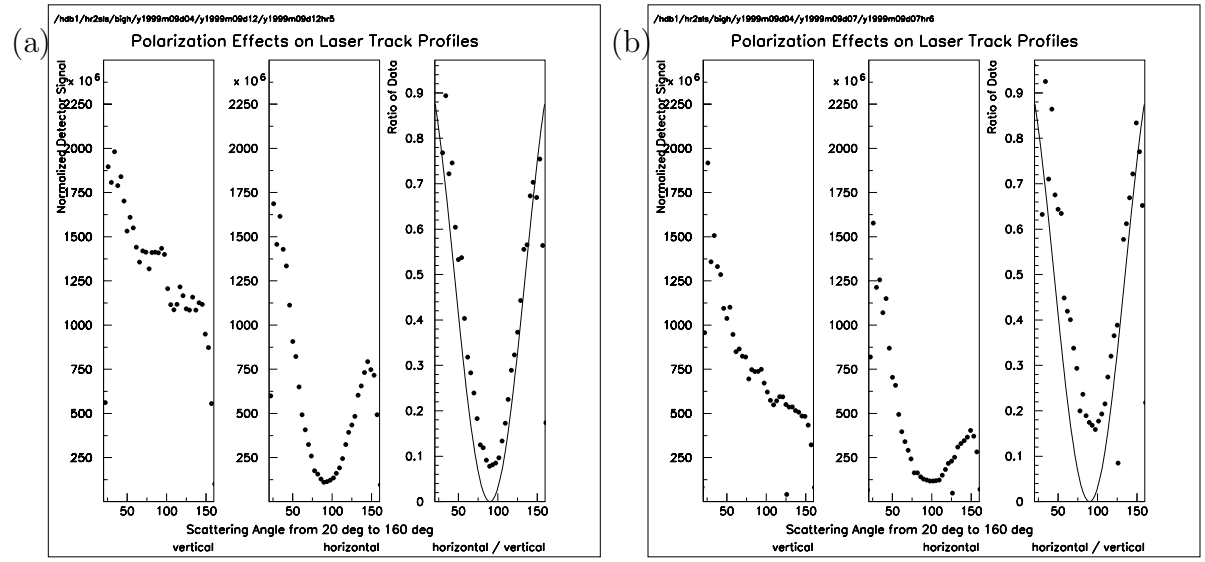

FIG. 3.3: Measurements of laser light at orthogonal linear polarizations and the ratio between them. Molecular scattering theory predicts that the ratio should be $\cos^2\theta$. These measurements were collected by the HiRes1 detector on relatively clear (a) and hazy (b) night.

with prediction for the Rayleigh scattering. The Rayleigh scattering theory also predicts that the ratio of the amount of light scattered from a beam polarized in the scattering plane to the amount of light scattered from a beam polarized perpendicular to the scattering plane will be $\cos^2\theta$ where θ is the scattering angle. Using the HiRes1 detector as a receiver, results for a relatively aerosol-free night (Fig. 3.3 (a)) are in good agreement with the $\cos^2\theta$ prediction. This agreement lessens on a hazy night due to depolarization of the beam by aerosols (Fig. 3.3 (b)).

The density profile of the molecular atmosphere and can be described by density and pressure at sea level and a scale height of 7.5 km. Daily and seasonal variations cause small variations at the 5 % level. A more accurate description can be obtained by daily radiosonde data in which pressure and temperature are recorded as a function of height by balloon based equipment released daily from major airports. Radiosonde data from Salt Lake City Utah and Reno Nevada, were compared over the period of a year. The differences between the Salt Lake and Reno density profiles measured on the same day were found to contribute an uncertainty to the molecular atmospheric transmission over 40 km of less than 3 % over a one year period [93].

3.2.2 The Aerosol Component

The aerosol component is more complicated. Aerosol sizes range from the from the 10^{-8}m scale of large molecules to the 10^{-5} m scale of particulate matter. Their distribution changes with location. Local dust can be lifted from the desert floor by the wind and transported to elevations that are typically less than a kilometer. More distant sources, for example, forest fires, volcanic erruptions, or manmade pollution can deposit aerosols high

in the atmosphere to be distributed over tens of km by upper level air flows. The aerosol distribution also varies with time. For example, a rain or snow storm will remove aerosols from the atmosphere often leaving near molecular viewing conditions.

The light scattering from aerosols of a specific size and regular shape can be described by the Mie scattering theory. In general the scattering probability as a function of angle, or phase function, is characterized by a forward peak, relatively little scattering at 90° and some enhancement for backwards scattering. The forward peak sharpens as the particle size increases, as one might expect from diffraction theory. Since the molecular phase function varies much less in this region, an increase in the amount of forward scattered light is a useful signature that aerosols are present. Of course the precise details of aerosol size, shape, and distribution are not known a priori and one must rely on phenomenologically based models for guidance. A commonly used simulation package called MODTRAN (Moderate Resolution Transmission) was developed by the US Air Force [94, 95]. It is also distributed commercially [96]. The package contains aerosol models for different regions including a "US Standard Desert" parameterization.

3.3 Monitoring the Atmosphere - Local measurements

Sensitivity to changes in the amount of aerosols is a crucial requirement of any atmospheric monitoring system. One simple technique used by HiRes for several years is to measure light scattered out of collimated Xenon flashbulb devices "Flashers" [97]. One of these is located relatively close to the HiRes1 detector in the geometry shown in Fig. 3.4. This device fires nearly horizontally 5 times every 7 minutes. HiRes measures its light over a range in scattering angles from approximately 30° to 150°. The two plots in Fig. 3.5 illustrate the sensitivity to aerosols. As the aerosol content increases, the amount of light detected at forward angles (30°) increases. However, the amount of light at large angles (120°–150°) remains relatively constant. The ratio of forward scattered light to large angle scattered light then yields a local measurement of changes in the aerosol content. Using a simple model based on the MODTRAN package [94, 95], this ratio can then be calibrated to a local horizontal attenuation length.

A one year compilation of flasher data (Fig. 3.6) reveals some interesting features. The distribution is not symmetric. The sharp edge on one side corresponds to the best case aerosol-free atmosphere that bounds the atmospheric monitoring problem. The mean value of the distribution corresponds to an aerosol ground level horizontal scattering length of 20–25 km. This is longer than the 12 km value for the standard desert parameterization under the MODTRAN simulation package. A conclusion of this analysis is that at least locally, the atmosphere at HiRes is clearer than the "standard desert" model. The atmosphere is better than "standard desert" and stable on about 70 % of the nights that HiRes operates. This data as well as similar data accumulated over two years of HiRes prototype operation in 1994–1995 shows that while local measurements are valuable it is still necessary to show that the atmosphere is homogeneous when it is stable and clear.

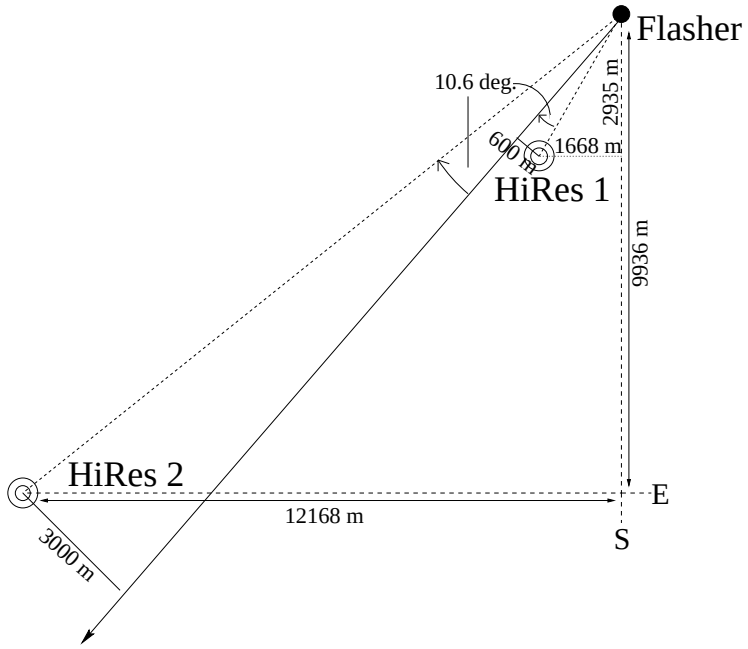

FIG. 3.4: Top view of the geometry of the HiRes intersite Flasher. The flasher elevation direction 4° above horizontal.

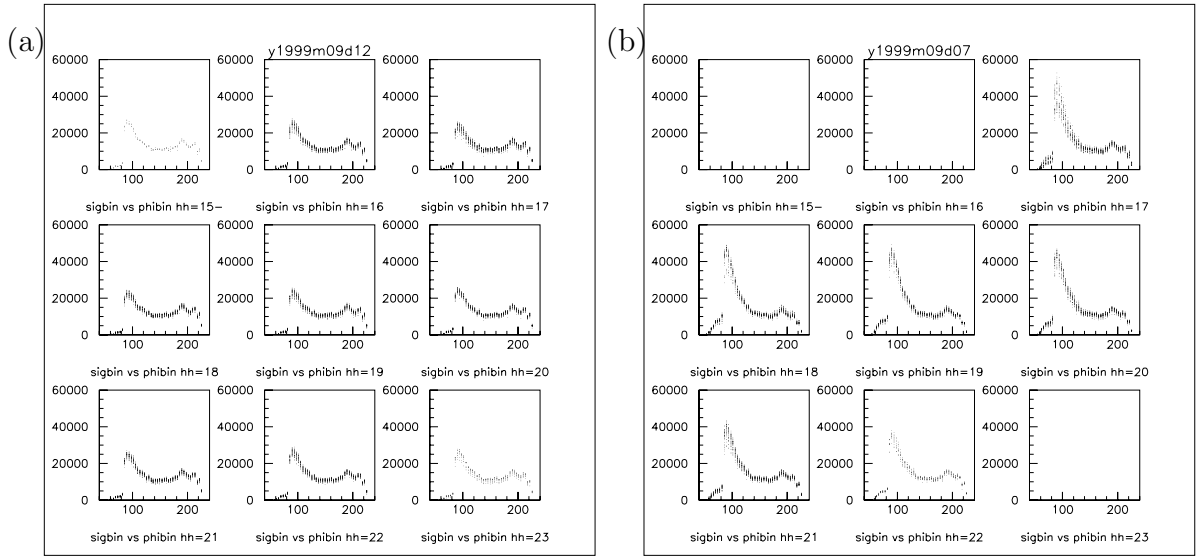

FIG. 3.5: Hour by Hour measurements of the Intersite Flasher on clear (a) and hazy (b) night. Each of the profiles shown covers a scattering angle from 30° to 150°. The height of the peak on the left axis is sensitive to changes in the local aerosol concentration. The forward scattering peak (left side of distribution) in the right figure has increased in comparison to the left figure.

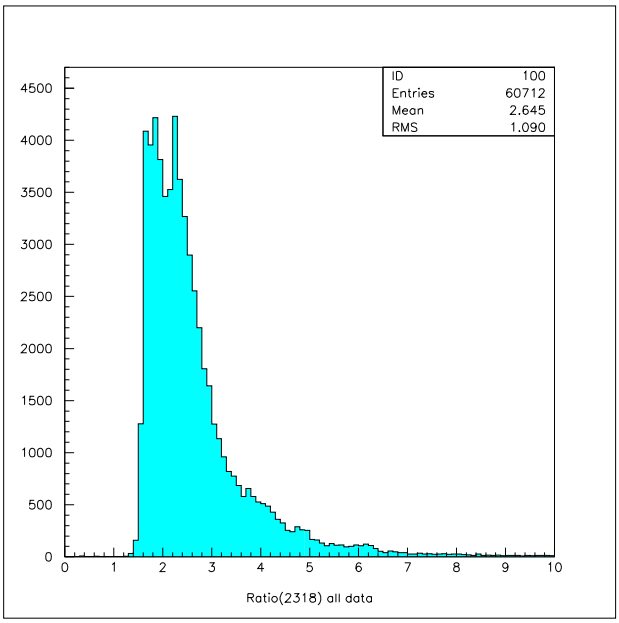

FIG. 3.6: The ratio of small angle scattering to sidewise scattering for the Intersite Flasher for 1998. The distribution cuts off on the left at molecular conditions. A "US Standard Desert" aerosol model has an aerosol attenuation length of 12 km and corresponds to 3.4 on this scale. At 2.6, the average of the data (20–25 km extinction length) indicates the average local atmosphere at HiRes is clearer.

3.4 Atmospheric Monitoring - longer range

Lasers are necessary to probe the large aperture in which the TA detectors will observe air showers. They also provide a signal with important similarities to the signal from an air shower. The 355 nm light from a frequency tripled Nd:YAG laser is well matched to the 357 nm air fluorescence line. The 10 ns pulse width is on the same scale as the thickness of the charged particle shower front that produces the scintillation light.

Such a laser system [98] (Fig. 3.7) is in use at HiRes. It has been observed by both the USTA telescopes at Cedar mt. and continues to be observed by the HiRes1 detector. The beam can be steered in any direction. The laser is specially designed for use in the field. Its polarization and energy can be varied under computer control. The relative energy of each shot is measured by a radiometer to an accuracy of about 1 %. The absolute energy is known to 10 %. A cover protects the steering mechanism from weather when not in use. A PC running linux controls the system and every component of the system is operated remotely.

Each hour this system produces a pattern of 1500 shots that are measured by the HiRes1 detector located 12.6 km away. The pattern, shown in Fig. 3.8, includes shots that sweep through the aperture. Light that has travel a total path length of more than 60 km from the laser to the scattering point and then to the detector can be observed on a clear night. For a given measured signal at the detector, this distance becomes smaller on the hazy night. A second system is being built at HiRes1 to be observed by the HiRes2 detector.

A variety of aerosol parameters have been extracted from the laser data. The aerosol

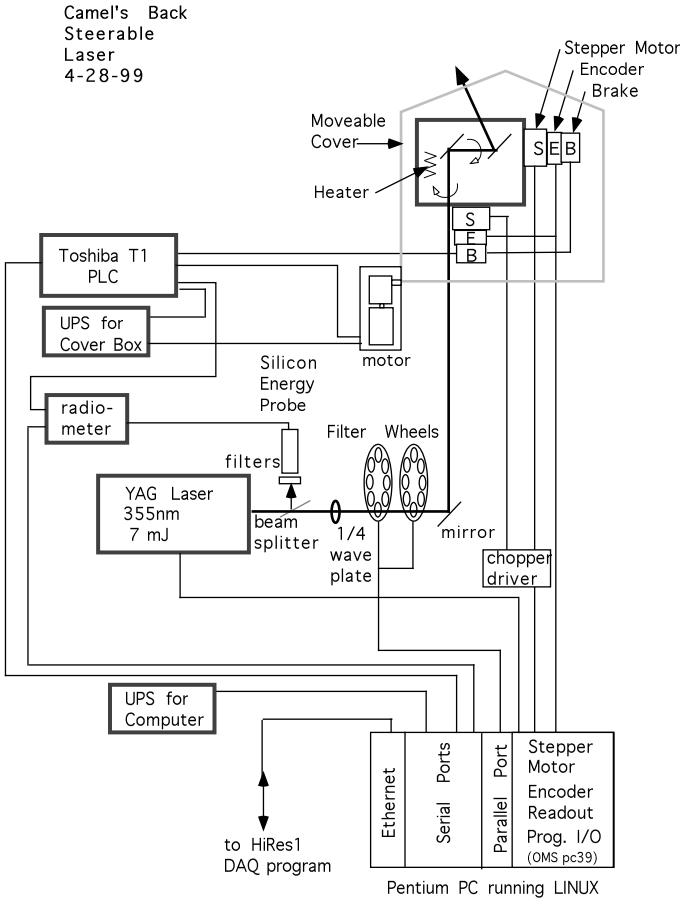

FIG. 3.7: HiRes2 Steerable Laser system.

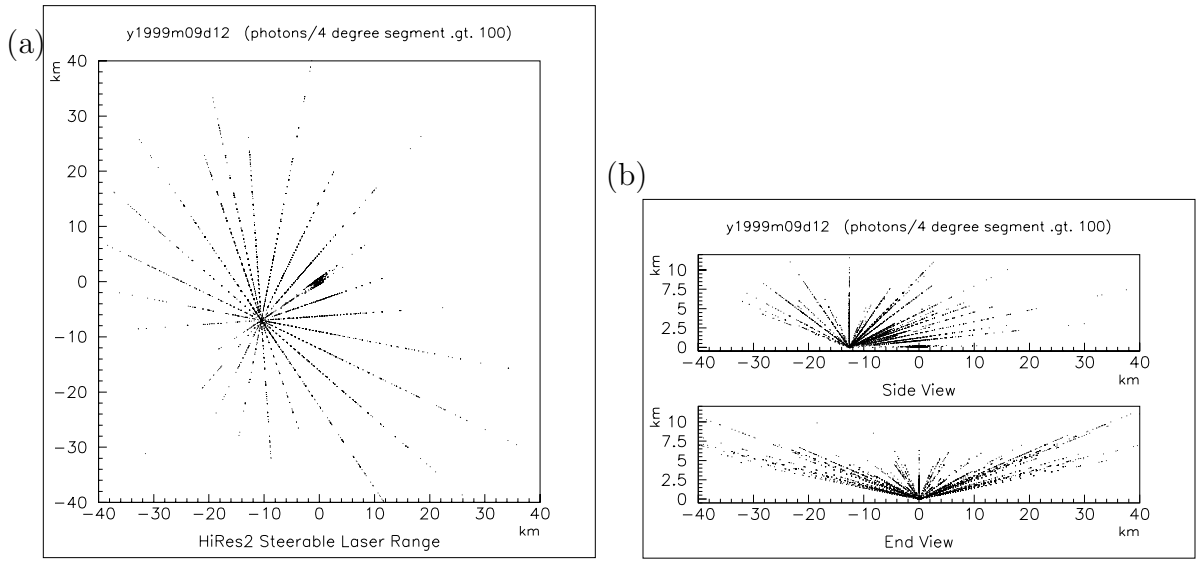

FIG. 3.8: Range of HiRes2 steerable laser as measured by the HiRes1 detector: (a) Top-view; (b) Side-view. The detector that made these measurements is located at 0,0 on the plot. These measurements were made on a night of typical viewing conditions.

transmission profile as a function of height can be obtained from a collection of laser tracks where the height and scattering angle is restricted to the region where aerosol scattering is much smaller than molecular scattering. (In this analysis, portions of the laser tracks for which the scattering angle ranges from 115° to 150° are selected. These angles should have minimal aerosol scattering on clear night. Thus the transmission as a function of height is obtained. We have assumed that the aerosols are uniform horizontally.)

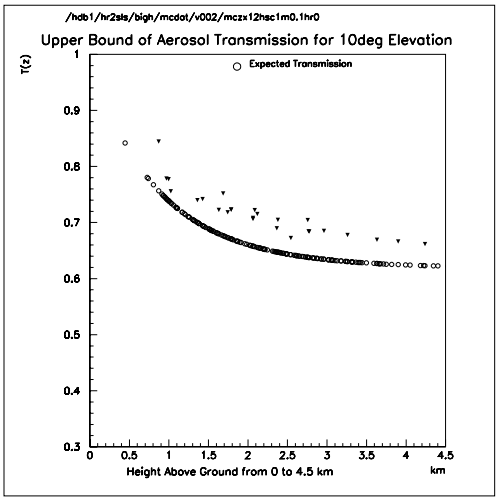

FIG. 3.9: Aerosol profile from simulated data for a "US Standard Desert Atmosphere. Circular points show the input parameterization. The vertical scale shows the transmission vs height for 10° viewing angle (4.5 km in height = 25 km horizontal distance).

Figure 3.9 shows results of this calculation for simulated data sample where the aerosol distribution is known. The data points extend to a height of 4.5 km. The transmission is calculated for a detector viewing angle of 10° which is typical of HiRes and TA. For reference, 4.5 km at 10° corresponds to a point 24 km distant. For this simulated data sample, the resulting transmission is about 10 % higher than the input value. It should be noted that an over estimate in the transmission corresponds to an under estimate in shower energy by a similar amount. Distributions for real data, shown for a relatively clear night (Fig. 3.10 (a)) of typical viewing conditions, and a very hazy night (Fig. 3.10 (b)). For reference, curves for a "standard desert" aerosol distribution are superimposed on the data distributions.

As the Japan/US R&D work continues and the second HiRes steerable laser system comes on line, it will be possible to test additional analysis techniques. Of particular interest are those for which the aerosol scattering is small or constant and measurements at different path lengths can be used to obtain the aerosol attenuation lengths. Several of these geometries are shown in Fig. 3.11 and Fig. 3.12.

Measurements of the aerosol horizontal attenuation length have also been obtained by scanning near horizontal laser shots with the USTA telescopes that were located 20 km distant at Cedar Mt. Since the both the laser and the telescopes could be pointed in any direction, the beam could be scanned over an attenuation length at nearly constant elevation. One of these measurements shown in Fig. 3.13 yields a total attenuation length of 11 km.

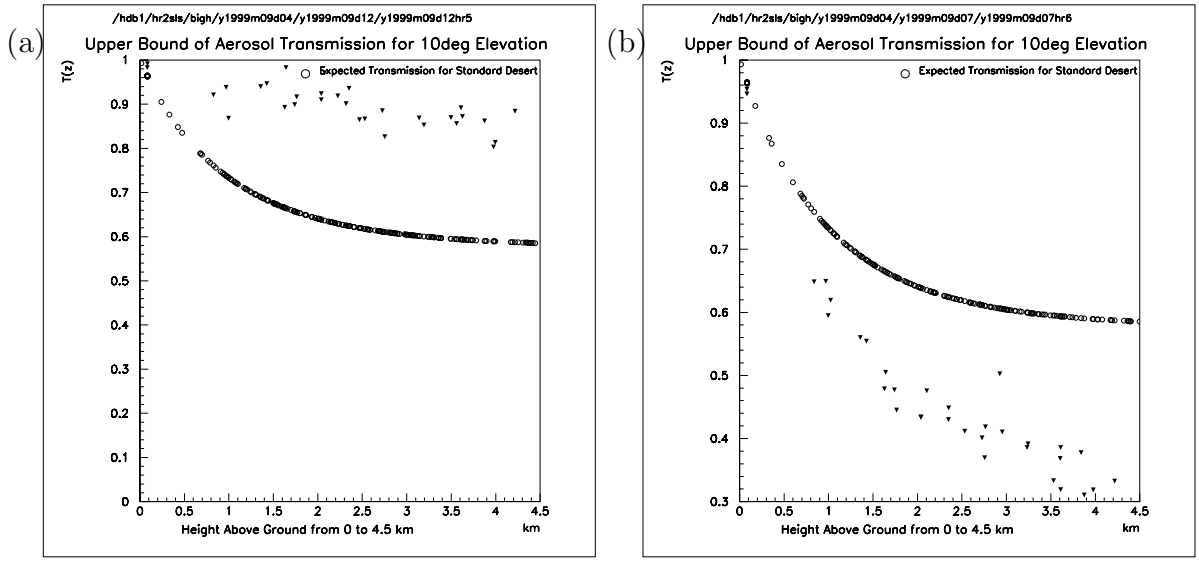

FIG. 3.10: Aerosol profile for real data on relatively clear (a) and hazy (b) night.

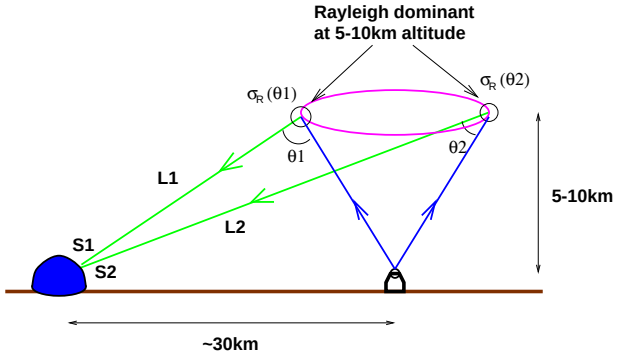

FIG. 3.11: Example of a detector laser geometry that can be used to obtain atmospheric attenuation lengths. The telescope observes the scattered light from the a height that is above the aerosols. The light scattered out of the beam can be described by the Rayleigh scattering theory. The attenuation length can be derived from the observation of the light intensities as a function of path length in the atmosphere.

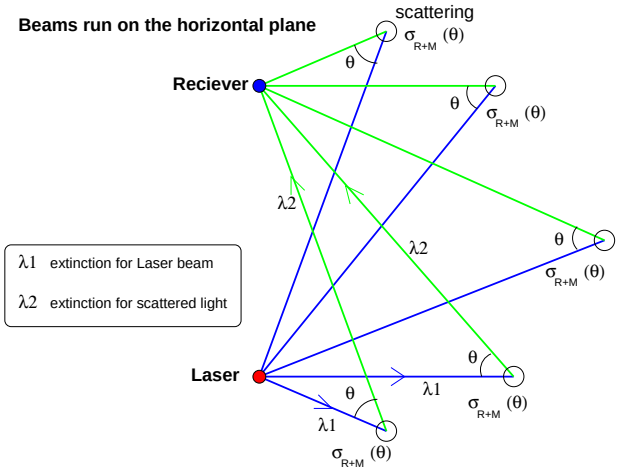

FIG. 3.12: Example of a detector geometry for determining horizontal attenuation lengths. The laser light is observed at a constant height and scattering angle.

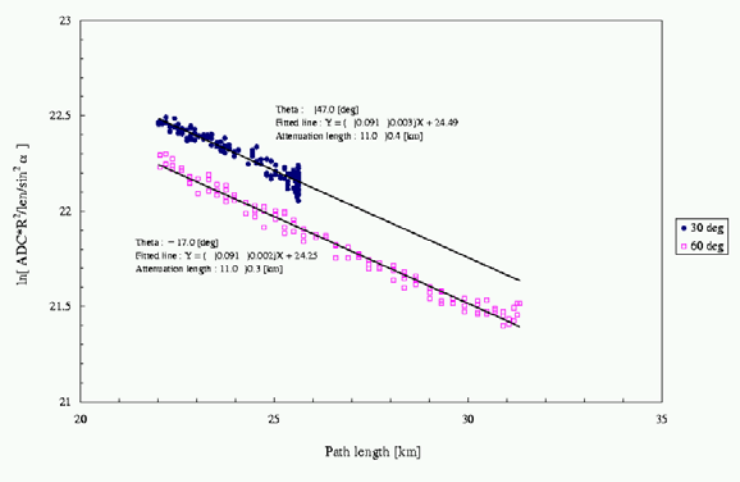

FIG. 3.13: The attenuation of a horizontal laser beam from the hr2sls system as measured by the USTA telescope at Cedar Mt. The attenuation length by the Mie scattering is estimated to be 28 km.

As part of the R&D effort an initial test of a LIDAR (Light Detection and Ranging) system was conducted at the HiRes1 site [99]. It consisted of a Nd:YAG(355nm) laser and a nearby 1.5 meter fixed direction mirror that collected the back scattered light and focused it on to a PMT. The PMT signal as a function of time was recorded by a digital oscilloscope. Figure 3.14 shows an example measurement made in Utah. The received light is described by the straight line. Under the assumption of atmospheric uniformity, we can obtain the transmittance as a function of thickness of atmosphere X. The attenuation length $\lambda(X)$ of 1440 g/cm^2 is obtained in this measurement.

The LIDAR technique is expected to be very valuable in determining inhomogeneities in the atmosphere. R&D is in progress to compare LIDAR and side scattered light sensitivity to aerosol parameters of interest.

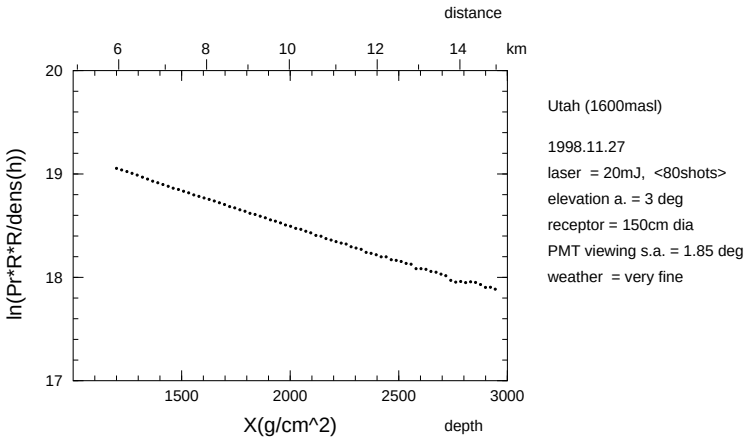

FIG. 3.14: A measurement made in Utah during a test of a back scatter LIDAR system. The attenuation length, λ was found to be 1440 g/cm^2 for $X = 1200$ to 3000 g/cm^2 during this test.

3.5 Cloud monitor by Infra-red imaging detector

With infra-red imaging detector, we can sense the temperature of each sky patch. If the cloud appear inside the field of view, it show the higher temperature than blue sky region. With the infra-red imaging detector sensitive to $\sim 10\mu$m photon, we can build high sensitive cloud monitor system. Mounting these system on the alt-azimuth mount (May be mounted on the Alt-Azimuth telescope), we can scan the whole sky and make the complete cloud map, for example, every 10min as shown in Fig. 3.15.

The cloud measurement will play a different role from atmospheric clarity measurement. Existing cloud in the target volume should be treated as dead volume in Telescope Array experiment. When we derive the energy spectrum, this effect should take into account in the exposure calculation.

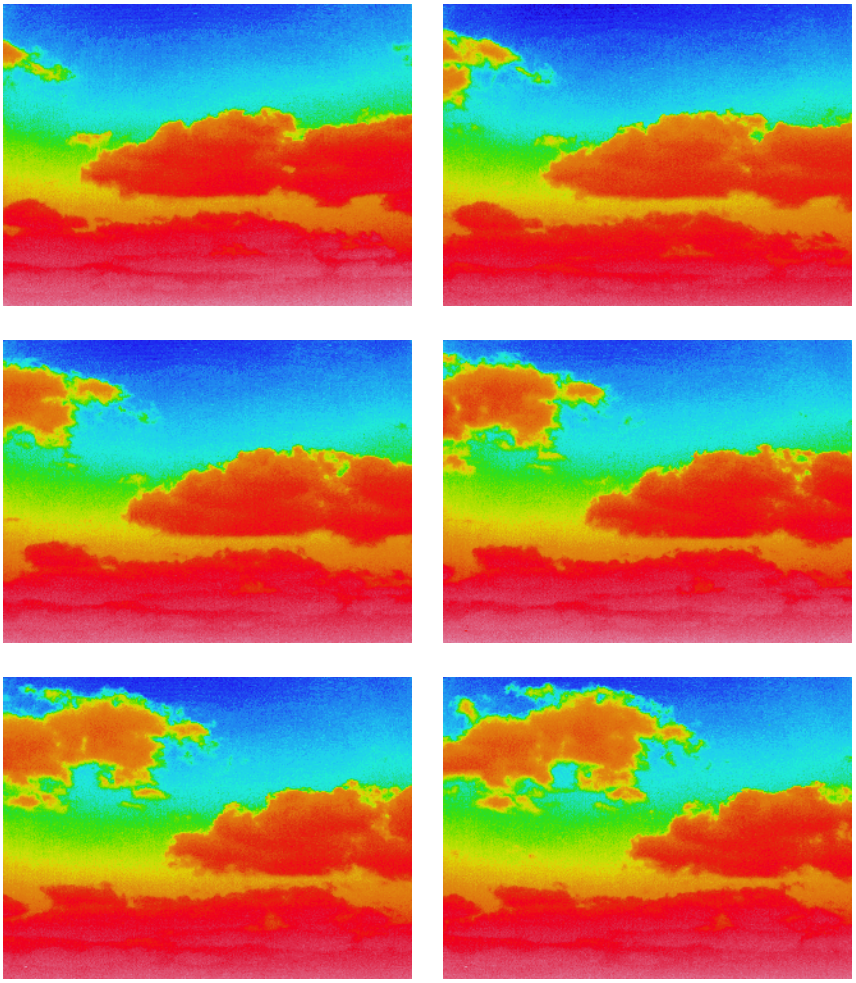

FIG. 3.15: The sky picture with 10μ photon. The field of view is elevation angle of $0^\circ - 19.5^\circ$, and azimuthal angle of 26° centered at south direction. The pictures were taken every 30 seconds. We can see well the movement of cloud.

3.6 Atmospheric Monitoring System for Telescope Array

The atmospheric monitoring system for the Telescope array will rely on steerable laser systems to probe the detector aperture. Of course, the TA fluorescence detectors can be used as optical receivers for atmospheric monitoring. When we use them, there is an advantage that tens to thousands of PMT's measure every laser and flasher shot fired through the detector aperture. We also plan to install the steerable telescopes of 3m diameter in each station, which have an advantage that the same camera is used to scan the laser beam for the side scatter measurement and reduce the systematic errors in the phase function measurement. This steerable telescope will also act as a LIDAR receiver for back scattered light to probe deep in the atmosphere.

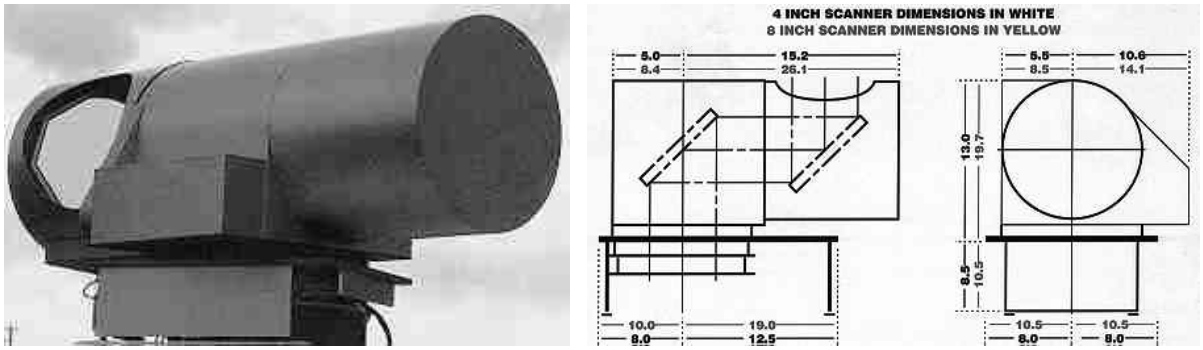

FIG. 3.16: LIDAR scanner developed by DFM engineering Inc. in US. The pointing resolution is 1/100 degrees, and the maximum rotating velocity is 60 degrees/sec. The interface with LINUX system is available. This system can be put at the top of the thick pipe located at the center of TA shelter.

In Fig. 3.16, the example of LIDAR scanner is shown. It was developed by DFM engineering, Inc. in US and used by researchers in meteorology. This system will be located at the top of the thick pipe at the center of the TA shelter. The linux interface is supported in this system and useful for the remote operation. The pointing resolution is 1/100 degree, and the maximum rotating velocity is 60 degree/sec. It is water proof. This system may satisfy our requirements. The laser system and optical system, similar with the HiRes2 laser system, which control the beam intensity and polarization will be installed inside the TA shelter and kept in the constant temperature environment.

The 3 m diameter alt-azimuth telescopes is shown in Fig. 3.17, which is developed as a Telescope Array prototype detector in Japan. It has pointing resolution of 1/1000 degree and the maximum rotating speed of 5 degree/sec.

The combination of the high accuracy pointing LIDAR scanner and the high accuracy alt-azimuth telescope in each station is very powerful. We can shoot laser at any direction and receive the scatter light from any point in the atmosphere and we can scan all sky region in both back scatter and side scatter measurement. Side scatter measurement can be done as an inter-site operation between neighboring two stations. The large diameter of the receiver will allow us the back scatter measurement in wide distance. The LIDAR

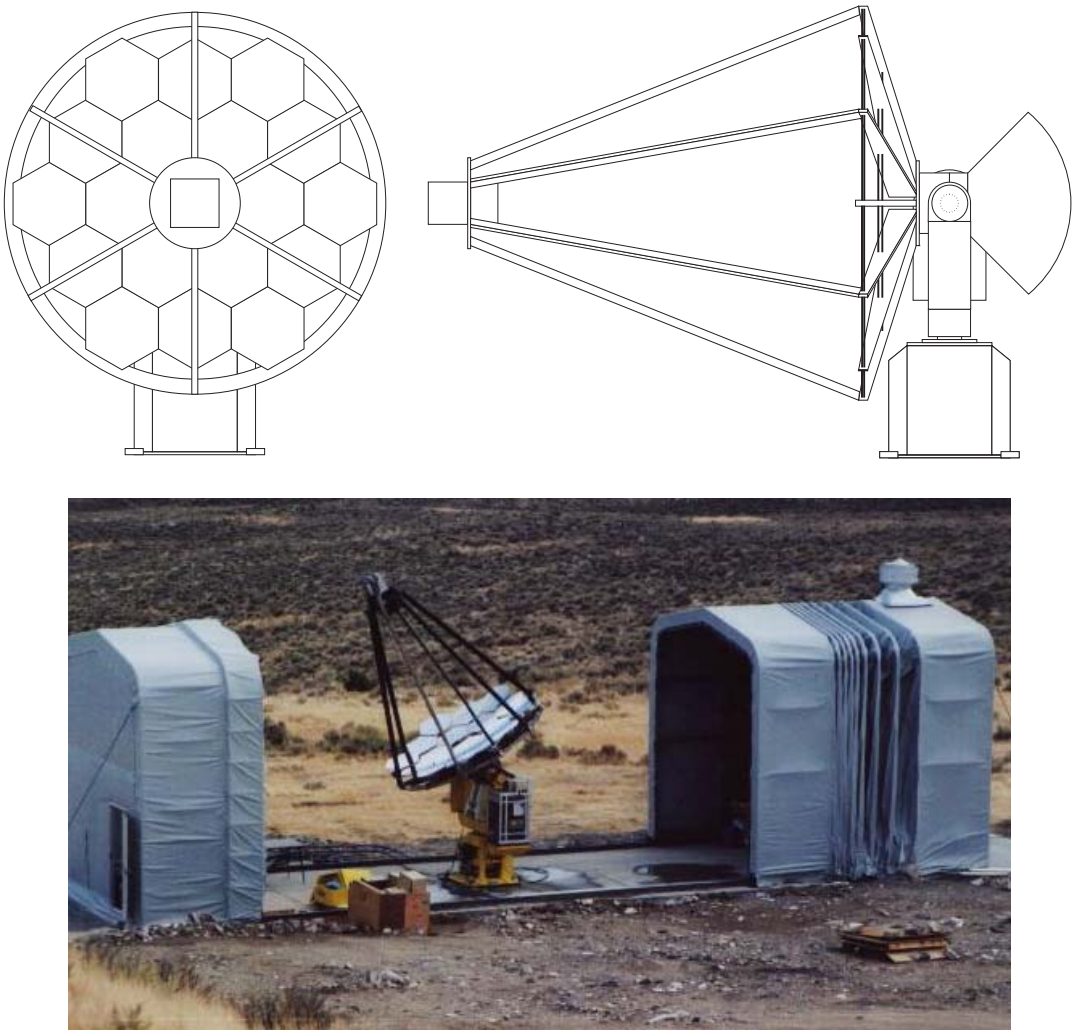

FIG. 3.17: Optical receiver for atmospheric monitoring in Telescope Array experiment. The mirror of 3m diameter is mounted on the alt-azimuth. The pointing resolution is 1/1000 degree and the maximum rotating speed is 5 degree/sec.

measurement at the zenith direction is also possible. There are a lot of freedoms in the atmospheric measurement with these apparatus.

The TA experiment will observe a large amount of atmosphere, roughly 300km by 100km, or about ten times that of HiRes. Despite the much larger area, details of the atmospheric monitoring challenge for HiRes and TA have important similarities. TA will be located in the same Great Basin desert area of Utah where HiRes is located. Although the 30–40 km intersite distances exceed the 12.6 km separation between the two HiRes stations, the highest energy showers observed by HiRes are generally 10–30 km away. This distance overlaps expected 20–40 km detector/shower separation for TA. The techniques used to monitor the atmosphere at HiRes will also work for Telescope Array, and the atmospheric monitor system for Telescope Array can be examined in the HiRes experiment.

Chapter 4

Physics Simulation and Expected Results

4.1 The TA Detector Simulation

The TA Detector Simulation Package has been developed and maintained for the R&D works. It consists of three subsets: the Event Generator, the Signal and Background Pulse Simulator, and the Event Reconstructor. In this section how the first two subsets work to generate simulation data is described briefly.

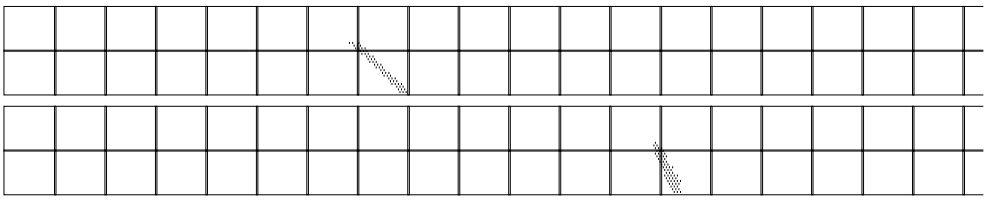

FIG. 4.1: An example of the simulated event tracks recorded in two stations.

4.1.1 The TA event generator

The Event Generator calculates signal strength produced by atmospheric fluorescence light emission from an Extensive Air Shower (EAS) with a given geometry, and builds simulation events by calculation of number of photoelectrons in every channels of a PMT camera in each mirror. It involves the longitudinal profile of an EAS, the models of the atmosphere, the air fluorescence yield, and the detector optics. Simulation of actual pulses with superposing the night sky background is performed in the second subset, the Signal and Background Pulse Generator, which will be described later.

The atmospheric density profile to calculate the physical height h_v as a function of atmospheric vertical depth X_v is given by

$$h_v(\mathrm{km}) = \begin{cases} 47.05 - 6.9 \ln X_v + 0.299 \ln^2 0.1 X_v & \mathsf{X_v} \leq \mathsf{25 g/cm^2} \\ 48.5 - 6.34 \ln X_v & \mathsf{25} \leq \mathsf{X_v} \leq \mathsf{230 g/cm^2} \\ 44.34 - 11.861 (X_v)^2 & \mathsf{X_v} \geq \mathsf{230 g/cm^2} \end{cases} . \quad (4.1)$$

Every $dX = 1$ g/cm^2 along a shower axis, it calculates number of electrons contained in the cascade if the primary cosmic ray has already initiated an EAS, otherwise will judge whether the primary particle interacts or not with the exponential probability $1 - \exp[-dX/\lambda_{int}] \sim dX/\lambda_{int}$. The number of electrons (the electron size) is calculated by the modified Gaisser-Hillas function:

$$N_e(E, X - X_1) = S_0 \frac{E}{\epsilon} \exp\left[\frac{X_{max}}{\lambda_{gh}} - 1\right] \left(\frac{X - X_1}{X_{max} - \lambda_{gh}}\right)^{\frac{X_{max}}{\lambda_{gh}} - 1} \exp\left[-\frac{X - X_1}{\lambda_{gh}}\right], \quad (4.2)$$

$$S_0 = 0.045 \left\{1 + 0.0217 \ln\left(\frac{E}{100\mathrm{TeV}}\right)\right\} \quad , \quad (4.3)$$

where $\epsilon \simeq 74$ MeV is the critical energy, X_1 is the first interaction length, $\lambda_{gh} \simeq 70$ g/cm^2 is the attenuation length of the shower profile, and X_{max} is the averaged position of shower maximum in the atmosphere as a function of primary energy E. We use the value of X_{max} by fitting the shower profile from the Corsika Monte Carlo simulation code given by

$$X_{max} = 58 \times \log\left(\frac{E}{1\mathrm{eV}}\right) - 297 \qquad \mathsf{g/cm^2} \qquad . \quad (4.4)$$

In this formula the actual position of shower maximum in an event is given by $X_{max} + X_1 - \lambda_{int}$. Consequently X_1 sampled for each event causes main fluctuations of the shower profile event by event. Note that this parameterization gives the radiation length X_{rad} for hadron-induced showers analytically by

$$\begin{aligned} X_{rad} &= S_0 \lambda_{gh} \exp\left[\tfrac{X_{max}}{\lambda_{gh}} - 1\right] \left(\tfrac{X_{max}}{\lambda_{gh}} - 1\right)^{-\left(\frac{X_{max}}{\lambda_{gh}} - 1\right)} \Gamma(X_{max}/\lambda_{gh}) \\ &\simeq \sqrt{2\pi \left(\tfrac{X_{max}}{\lambda_{gh}} - 1\right)} S_0 \lambda_{gh} \\ &\sim 32\, \mathsf{g/cm^2} \end{aligned} \quad . \quad (4.5)$$

The Generator also has another option to use numerical functions fitted by the shower profile simulated by the Corsika and/or AIRES Monte Carlo package instead of using the Gaisser-Hillas formula given by Eq. (4.2). In this option X_1 and X_{max} are given directly from the external Monte Carlo shower simulation package.

Number of photoelectrons received by a mirror in each station, which is originated in atmospheric fluorescence emission from the EAS, is then calculated as follows.

$$\frac{dN_{pe}}{dL} = \frac{N_e \epsilon_{fl}(h_v)}{4\pi r^2} T_{surf} T_M A_{mir} \int d\lambda \exp\left[-\frac{\Delta X_{det}}{\lambda_R} \left(\frac{400\mathsf{nm}}{\lambda}\right)^4\right] f_{fl}(\lambda) Q(\lambda) \epsilon_{BG3}(\lambda) R_{mir}(\lambda). \quad (4.6)$$

Here $\epsilon_{fl}(h_v)$ is yield of atmospheric fluorescence, T_{surf} is the transmission factor of the surface reflection, T_M is the transmission factor of propagation of light taking account of the Mie scattering, A_{mir} is area of a mirror, ΔX_{det} is the atmospheric slant depth between the location of a mirror and the light-emission point along the shower axis, $f_{fl}(\lambda)$ is atmospheric fluorescence spectrum as a function of wavelength λ, $Q(\lambda)$ is quantum efficiency of a PMT tube, $\epsilon_{BG3}(\lambda)$ is the transmission factor of an optical filter installed in front of the camera, and $R_{mir}(\lambda)$ is reflectivity of a mirror.

As expressed in Eq. (4.6), the Mie scattering cross section is approximated to be independent of the wave length λ in the current Generator. The transmission factor T_M is then written by

$$\ln T_M = \left(e^{-h/H_M} - e^{-h_{det}/H_M}\right) \frac{H_M}{L_M \cos\theta} \quad , \tag{4.7}$$

where H_M is the scale height and L_M is the mean free path.

The Cherenkov light emission also makes significant contribution to the overall light intensity especially if an EAS goes *toward* direction of a station. Because the Cherenkov radiation is anisotropic, one must consider the distribution of scattered angles during the propagation of light. Currently the Generator approximates that the angular distribution is determined dominantly by its direct Cherenkov emission angle and the Rayleigh scattering angle whose distribution follows $(1 + \cos\theta^2)$. Thus the overall Cherenkov intensity is calculated as follows.

$$\begin{aligned}\frac{dN_{pe}^{ch}}{dL} = \; & N_e \epsilon_{fl}(h_v) I_{ch}(h_v) T_{surf} T_M A_{mir} \\ & \times \Big[\frac{e^{-\theta/\theta_0}}{2\pi r^2 \sin\theta\theta_0} \int d\lambda \exp\left[-\frac{\Delta X_{det}}{\lambda_R}(\frac{400\mathsf{nm}}{\lambda})^4\right] \frac{1}{\lambda^2} Q(\lambda)\epsilon_{BG3}(\lambda) R_{mir}(\lambda) \\ & + \frac{3(1+\cos\theta^2)}{16\pi r^2} \int d\lambda (1.0 - \exp\left[-\frac{dX}{\lambda_R}(\frac{400\mathsf{nm}}{\lambda})^4\right]) \exp\left[-\frac{\Delta X_{det}}{\lambda_R}(\frac{400\mathsf{nm}}{\lambda})^4\right] \frac{1}{\lambda^2} Q(\lambda)\epsilon_{BG3}(\lambda) R_{mir}(\lambda)\Big]\end{aligned} \quad , \tag{4.8}$$

where θ_0 is the direct Cherenkov angular scale, $dX = 1\mathsf{g/cm^2}$ is the sampling step in the program, and $I_{ch}(h_v)$ is intensity of the Cherenkov emission as a function of the height in the air.

Then an individual photoelectron is given its source photon-emission point in the shower cascade taking account of the lateral distribution of air showers following the NKG function. The vector from the emission point to the detector station is put into the telescope ray-tracing program to calculate its trajectory to determine a mirror and a tube that receives the photon.

Repeating the above processes builds an array of number of photoelectrons as a function of time for every channels. It is passed to the Signal and Background Pulse Simulator.

4.1.2 Signal and background pulse simulator

This program simulates pulses in the electronics generated by the photoelectron distribution calculated by the Event Generator. It also estimates the night sky background intensity and simulates its contribution.

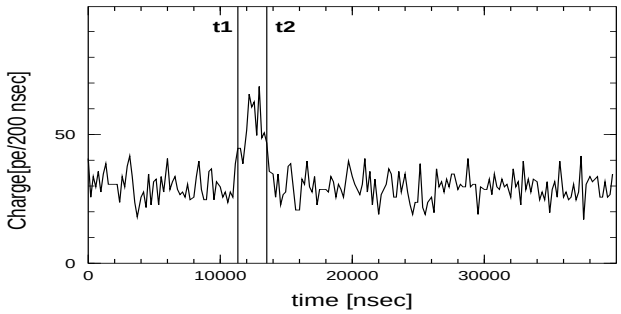

FIG. 4.2: An Example of the pulse profile simulated by the Pulse Simulator.

The signal finding algorithm described in Chapter 2 is then performed for all the recorded channels to determine the timing window $[t_1, t_2]$ to give the best signal to noise ratio. The pulse profile within the window is used for the event reconstruction. Figure 4.2 shows an example of the simulated pulse profile.

Figure 4.3 shows the longitudinal shower profile simulated by the procedure described here. The angular width of shower track makes differences of the number of photoelectrons in different tubes viewing the same atmospheric slant depth along the track. The dead space between the tubes ($\sim$ 2 mm) has also been taken into account in the generator to cause some ups and downs of the profile as seen in the figure.

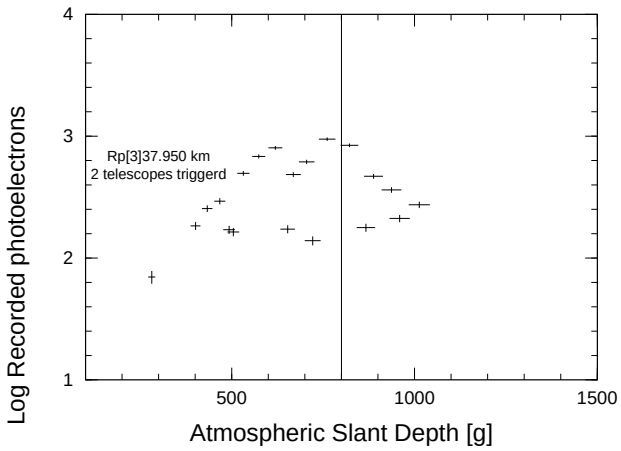

FIG. 4.3: An Example of the longitudinal shower profile simulated by the TA Monte Carlo. Each cross shows the number of photoelectrons and the FOV in unit of atmospheric depth of an individual tube. The vertical line corresponds to the shower maximum of this particular event.

4.2 The Event Reconstruction

4.2.1 The center-of-gravity constraint

For most of triggered events, the air fluorescence detectors that aim at observing air showers passing $\sim$ 30 km away have track lengths which are usually shorter than 15° on the PMT clusters because of the geometrical factor and the attenuation of signals in the atmospheric propagation. Short track events have several difficulties to be reconstructed with great accuracy. First, the χ^2 fitting procedures suffer multiple local minima to give the wrong geometry fitting. Secondly, even when the shower-detector plane can be fitted nicely with the event track, the true geometry cannot be always resolved because the longer the impact parameter becomes, the lesser the true geometry depends on direction of the fitted shower detector plane in each station. Finally the longitudinal shower development gives very rapid change in the flux along the track, which leads to strong correlation between the geometrical fitting and shower profile fitting. One needs to know how the flux changes along the track before the geometrical fitting in order to get better angular resolution.

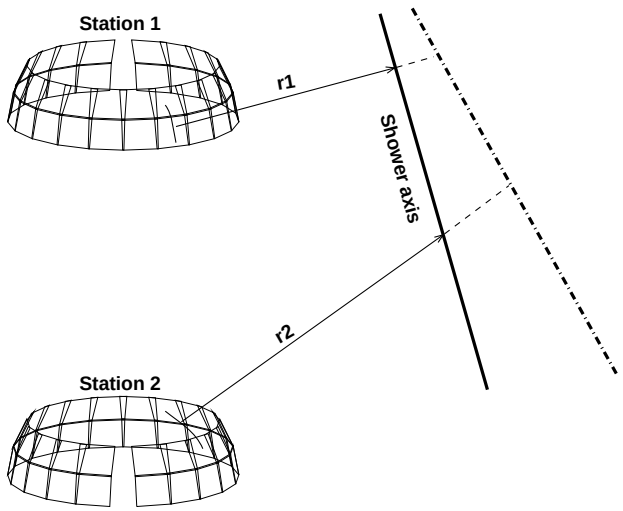

FIG. 4.4: Concept of the center of gravity constraint. The shower axis can be defined in two dimensional phase space, r_1 and r_2.

The local χ^2 problem originates in dealing with too many dimensions of the phase space in the χ^2 fitting procedure. One needs 4 parameters to define the shower geometry (e.g., zenith, azimuth angle, and (x, y) for the core location). Hence we have introduced additional constraint on the fitting to reduce the dimension. Short track events have no redundancy to deal with multiple dimensions.

Direction of the center of gravity of the event track is the one which can be calculated from the geometrical track information with maximum redundancy. This is determined as follows:

$$\mathbf{n_g} = \frac{1}{|\mathbf{n_g}|} \begin{pmatrix} \sum_i nx_{PMT,i} \times n_{pe,i} \\ \sum_i ny_{PMT,i} \times n_{pe,i} \\ \sum_i nz_{PMT,i} \times n_{pe,i} \end{pmatrix} \quad . \tag{4.9}$$

Here $(nx_{PMT,i}, ny_{PMT,i}, nz_{PMT,i})$ is the unit vector of the central direction of PMT i's FOV, and $n_{pe,i}$ is number of photoelectrons integrated and recorded in channel i.

The direction determined at each station should point the shower track. The Monte Carlo study actually confirmed that the direction can be determined within $\sim 0.03^\circ$ off the track axis. Thus it is very good assumption that the fitted shower axis should cross the axis of the center of gravity direction (noted as G-direction hereafter). Then only two parameters of r_1 and r_2, lengths along the axis of the G-direction at two stations would completely define the shower geometry. Under this constraint, the phase space of the geometrical fitting is two dimension of r_1 and r_2 which leads to very robust fitting for most of the events. This concept is illustrated in Fig. 4.4.

4.2.2 Fast reconstruction for initial guess

The data is first processed by the fast reconstruction to give an initial guess of its geometry before the main reconstruction procedure. The method here is based on the Amplitude Weighting Method, the simplest and traditional way of using available PMT signal in-

formation to determine the shower geometry. The shower-detector plane (SDP) at each station is determined to minimize the χ^2,

$$\chi^2 = \sum_k \frac{(\Delta\theta_k)^2}{\sigma_k^2} w_k \qquad , \tag{4.10}$$

where

$$\Delta\theta_k = \cos^{-1}(\mathbf{n_{pmt,k}} \mathbf{n_{SDP}}) - \frac{\pi}{2} \qquad , \tag{4.11}$$

$$\sigma_k = 0.3^\circ, w_k = \frac{n_{pe,k}}{\bar{n}_{pe}} \qquad . \tag{4.12}$$

Here $n_{pmt,k}$ is normal vector of direction viewed by PMT k, $\bar{n}_{pe}$ is averaged number of photo electrons per channel over an event track, $\mathbf{n_{SDP}}$ is the normal vector of the SDP direction.

Then the arrival direction $\mathbf{n}$ is determined by

$$\mathbf{n} = \frac{\mathbf{n_{SDP,i}} \times \mathbf{n_{SDP,j}}}{|\mathbf{n_{SDP,i}} \times \mathbf{n_{SDP,j}}|} \qquad . \tag{4.13}$$

The suffix i, j are associated with the stations to trigger the event. When more than two stations trigger an event, two stations receiving most and second most number of photoelectrons are selected to give an initial guess of its arrival direction.

The G-direction defined by Eq. (4.9) and the length of the axis of this direction to the initially determined shower axis then can be calculated. The determined r_1 and r_2 set the starting point for the main fitting procedure described below.

4.2.3 Reconstruction using the pulse profile

The TA front-end electronics based on the ADC-DSPs records the signal profile as a function of the sampling time. Fine geometrical resolution is obtained by minimizing the χ^2 built by comparison of the prediction of the signal profile by the TA Monte Carlo event generator with the recorded profile every sampling frequency. This is called the Signal Wave Form Fitting method.

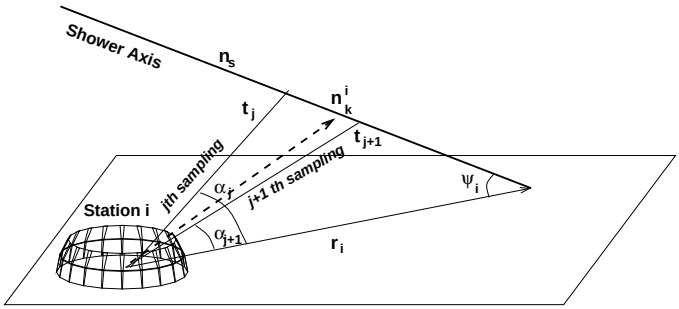

FIG. 4.5: Concept of the Signal Wave Form fitting for the ADC-DSP-based electronics. $t_{j+1} - t_j$ corresponds to the sampling time (200 nsec for the TA ADC-DSPs).

Figure 4.5 illustrates how the event geometry determines the signal profile. The longitudinal direction α_j at the station i along the shower track is related to a given event geometry and relative timing at j-th sampling as follows.

$$\alpha_j = \pi - \psi_i - 2\tan^{-1}\left[\frac{c}{R_p^i}\left(t_j - t_0 - \frac{\mathbf{n_s}\mathbf{r_i}}{c}\right)\right], \tag{4.14}$$

where R_p^i is the impact parameter from station i, $\mathbf{n_s}$ is direction of the shower axis, and $\mathbf{r_i}$ is the vector from the station to the core location. The event geometry is defined by the two parameters r_1, r_2 that are the lengths along the axis of the G-direction and t_0, the absolute origin of the timing assuming that the clock at each station is relatively synchronized. Consequently the signal profile at every sampling time, i.e., how the light spot crosses the PMT is a function of r_1, r_2 , and t_0 via Eq. (4.14).

In fact the prediction of the signal profile relies on not only the geometrical factor as expressed by Eq. (4.14) but the other factors: the telescope optics such as spot size and optical aberrations, PMT response, intrinsic width of the shower track (i.e., lateral distribution of electrons in the cascade), and the longitudinal shower profile. The optics and PMT response can be simulated by ray-tracing program and the detector Monte Carlo. The lateral distribution of showers can be reasonably described in the NKG formula as a function of the atmospheric slant depth. Hence this method needs to utilize the full detector simulation to estimate the expected amplitude in each channel. To deal with the the longitudinal shower profile, we use the normalization method to average the expected flux from all PMTs within a certain angular bin along the track based on the assumption that the flux change smoothly along the track. In this method the Monte Carlo simulation is responsible for predictions of effects from the optics, the PMT response, and the lateral distribution of a shower but does not need to consider the longitudinal profile.

Then χ^2 to be minimized in the Signal Amplitude Fitting to determine the geometry of a shower track is given by

$$\chi^2 = \sum_{i}^{station}\sum_{k}^{PMT}\sum_{j}^{sampling}\frac{\left(n_{pe,measured}^{i,k,j} - n_{pe,predicted}^{i,k,j}(r_1, r_2, t_0)\right)^2}{n_{pe,measured}^{i,k,j}} \quad , \tag{4.15}$$

with the normalization by

$$\sum_{k}^{\Delta\alpha} n_{pe,predicted}^{i,k,j}|_{t_j} = \sum_{k}^{\Delta\alpha} n_{pe,measured}^{i,k,j}|_{t_j} \quad . \tag{4.16}$$

Here t_j is timing at j-th sampling. The angular bin of the normalization in Eq. (4.16), 3° of $\Delta\alpha$, gives the best performance. Several investigations have shown that minimizing the χ^2 value only with the channels having better than 4σ of integrated signal-to-noise ratio over the time window leads to the reasonable reconstruction. The reconstruction program initially requires two stations with recording more than 5 PMTs with $\geq 4\sigma$.

The χ^2 written by Eq. (4.15) still has many local minima. In the initial investigation one finds that even the fitting under the center of gravity constraint sometimes trap events in a local minimum to give the bad geometrical resolution if one performs the fitting in too large size of the phase space. The risk of the minimization process finding some local minimum

is not negligible. Several investigations showed that using the Amplitude Weighting χ^2 as a guideline to define the size of the phase space (r_1,r_2) works well to prevent the poor fitting. In this method, whenever the Amplitude Weighting χ^2 given by Eq. (4.10) reaches a certain threshold value, the routine stops the fitting further and try a new dimension of the phase space for another trial as if the fitting procedure "bounced" at a wall.

4.2.4 Reconstruction of longitudinal shower development

Reconstruction of the longitudinal development to determine a first interaction point, X_1, and X_{max} is based on the Maximum Likelihood Method. The probability of a photoelectron arrival at a PMT i from longitudinal angle α along the axis of the shower track is given by

$$P_i(\sigma^i_{spot}, \alpha) = \frac{1}{\Delta_i} \int_{-\Delta_i/2}^{+\Delta_i/2} \frac{1}{\sqrt{2\pi}\sigma^i_{spot}} \exp\left[-\frac{(\alpha-\psi)^2}{2{\sigma^i_{spot}}^2}\right] d\psi \quad . \tag{4.17}$$

The spot size σ^i_{spot} and pixel size Δ_i are calculated by the ray tracing program.

This equation based on angular space can be transformed to phase space of the physical atmospheric slant depth:

$$P_i(\sigma^i_{spot}, X - X^i_0) = \frac{\sqrt{1-(\mathbf{nn_i})}}{r_i} \left.\frac{dh_v}{dX_v}\right|_{X=X^i_0} \frac{1}{\Delta_i}$$
$$\times \int_{\frac{-\Delta_i}{2}}^{\frac{\Delta_i}{2}} \frac{1}{\sqrt{2\pi}\sigma^i_{spot}} \exp\left[-\frac{(\frac{\sqrt{1-(\mathbf{nn_i})}}{r_i}\frac{dh_v}{dX_v}(X-X^i_0)-\psi)^2}{2{\sigma^i_{spot}}^2}\right] d\psi \quad , \tag{4.18}$$

where $\mathbf{n_i}$ is normal vector of the FOV direction of PMT i, X^i_0 is the atmospheric slant depth along the track at center of the FOV of PMT i, r_i is a distance from the mirror to the shower track at the center of FOV, h_v is the vertical height of atmosphere and X_v is the vertical atmospheric depth.

Then we can form a likelihood function for the longitudinal profile of signals along the track by folding the probability function of Eq. (4.18) with a longitudinal development of photoelectrons expected from the air shower:

$$\ln L_l = \sum_i^{all} n^{measured}_{pe,i} \times \ln\left[\kappa \int dX P_i(\sigma^i_{spot}, X - X^i_0) N_e(X, X_{max}, X_1, N_{max}) \frac{dN_e}{dN_{pe}dX}\right], \tag{4.19}$$

where κ is the normalization factor, N_{pe} is number of photoelectrons, N_e is electron size as a function of atmospheric depth given by the Gaisser-Hillas Formula:

$$N_e(X, X_{max}, X_1, N_{max}) = N_{max}\left(\frac{X-X_1}{X_{max}-X_1}\right)^{\frac{X_{max}-X_1}{\lambda}} \exp\left[\frac{X_{max}-X}{\lambda}\right] \quad . \tag{4.20}$$

And $dN_e/dN_{pe}dX$ is determined by geometry of track, fluorescence yield, transmission factors due to the atmospheric extinction, and detection efficiency of the detectors, all of which is calculated by the Monte Carlo simulation. Let us remark here that

$$P_{pe}(X, X_{max}, X_1) = N_e(X, X_{max}, X_1, N_{max}) \frac{dN_e}{dN_{pe}dX} \tag{4.21}$$

is the photoelectron distribution expected from the longitudinal development profile determined by X_{max}, X_1, and N_{max}.

X_{max} and X_1 are determined by maximizing L_l, and N_{max} in Eq. (4.20) is estimated by summation of detected photoelectrons. The primary energy of the event is given by

$$E = \frac{\epsilon}{X_{rad}} \int N_e(X, X_{max}, X_1, N_{max}) dX \qquad , \tag{4.22}$$

where $X_{rad} = 34.5$ g/cm^2 is the radiation length in the atmosphere and $\epsilon \simeq 74$ MeV is a critical energy.

4.3 Aperture

In this section the event reconstruction aperture expected in the Telescope Array is described. The TA detector simulation described in the previous sections has generated simulation data sets for this study. The events are reconstructed when at least 6 PMTs of one or two neighboring telescopes are fired 4 σ above the night sky background. The total number of detected photoelectrons and the length of the reconstructed track are shown in Fig. 4.6 for 10^{20} eV protons having at least one reconstructed track.

In order to define the stereo aperture of TA, we required that at least two stations have a well reconstructed track, both of which extend more than 5° in the field of view (FOV). Some representative properties of the reconstructed tracks are shown in Fig. 4.7 for 10^{20} eV protons. The aperture obtained with this condition is plotted in Fig. 4.8 for 10^{18} – 10^{21} eV protons. It is $\sim$ 50,000 km^2 sr for 10^{20} eV protons. The location of the shower luminous center is plotted in Fig. 4.9 for 10^{19} and 10^{20} eV protons. The figure indicates that the shower as far as $\sim$ 60 km away from the closest station can be detected and reconstructed for 10^{20} eV protons. The acceptance for the 10^{19} eV proton is not concentrated in the vicinity of each station but rather uniformly distributed near the center of the TA site.

The expected event rates are listed in Table 4.1. The events with energies beyond 10^{20}eV are detected at 50 events/year assuming the flux of super GZK events measured by AGASA.

Table 4.1: The Cosmic ray hadron annual event rate detected and reconstructed by the Telescope Array. The cosmic ray flux measured by AGASA is assumed.

Energy			Event rate [yr^{-1}]
3×10^{18} eV	$\leq$ E $\leq$	10^{19} eV	9550
10^{19} eV	$\leq$ E $\leq$	3×10^{19} eV	1700
3×10^{19} eV	$\leq$ E $\leq$	10^{20} eV	320
10^{20} eV	$\leq$ E		50

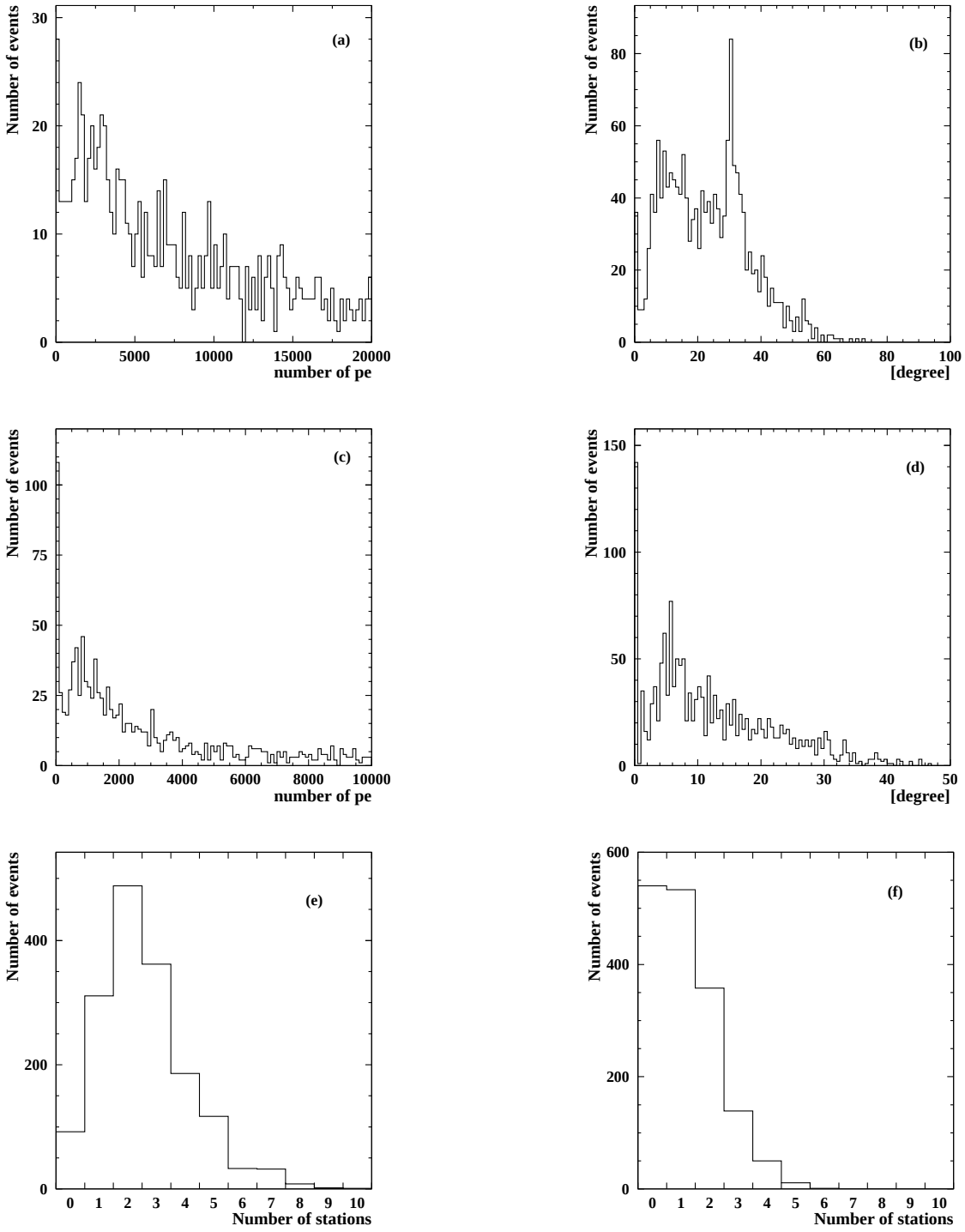

FIG. 4.6: (a,b) The number of photoelectrons and the track length for the the station observing the longest track. (c,d) The same for the station observing the second longest track of the event. The number of stations with the track length longer than 5° (e) and 15°.

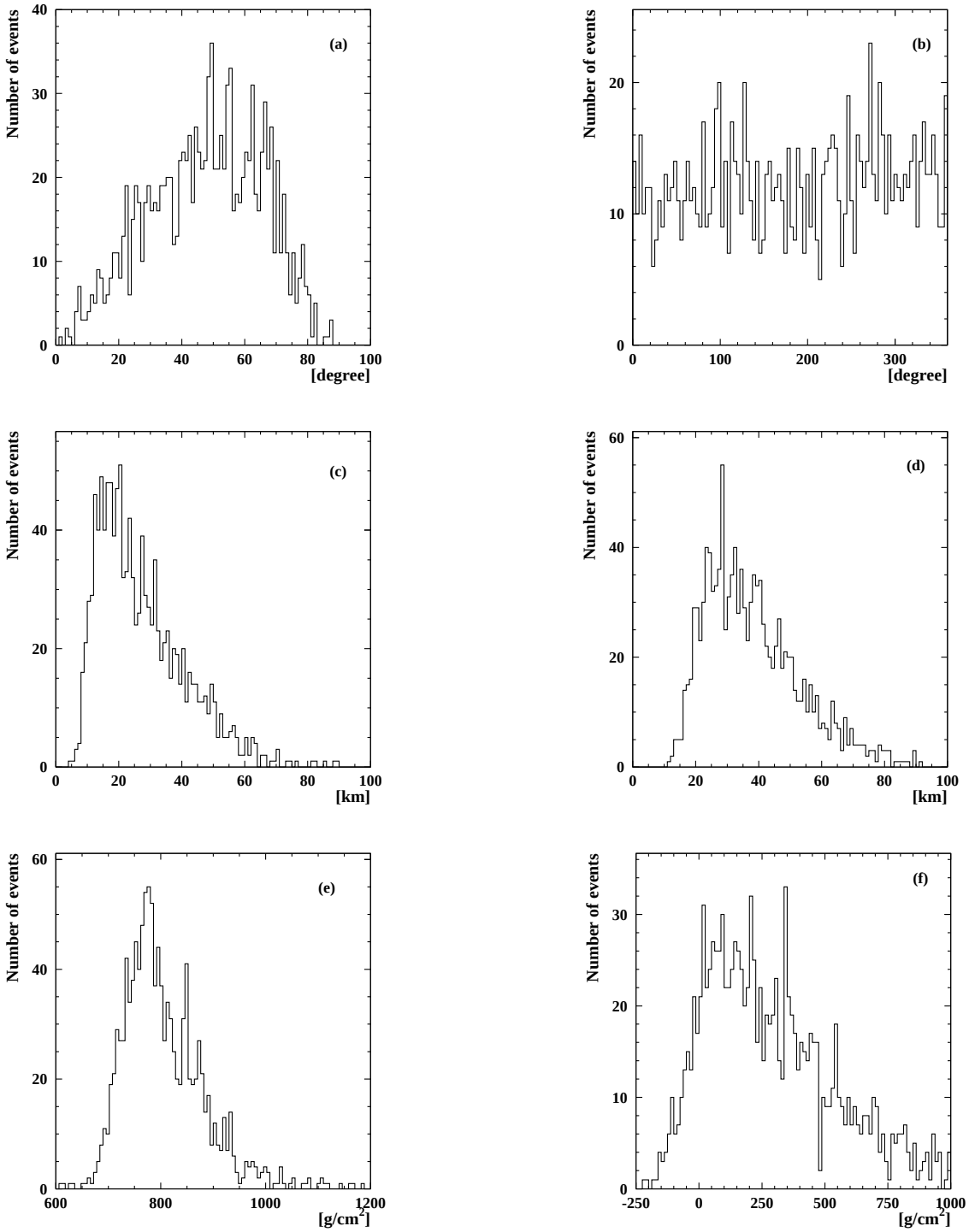

FIG. 4.7: (a) Zenith and (b) azimuthal angle distribution of reconstructed tracks. (c) The distance from the luminous center of the shower to the nearest station and (d) to the second nearest station. (e) X_{MAX} and (f) $X_{END} - X_{MAX}$ distribution where X_{END} means the last observed point (tail) of the shower. The negative $X_{END} - X_{MAX}$ means the shower maximum was not observed in the FOV.

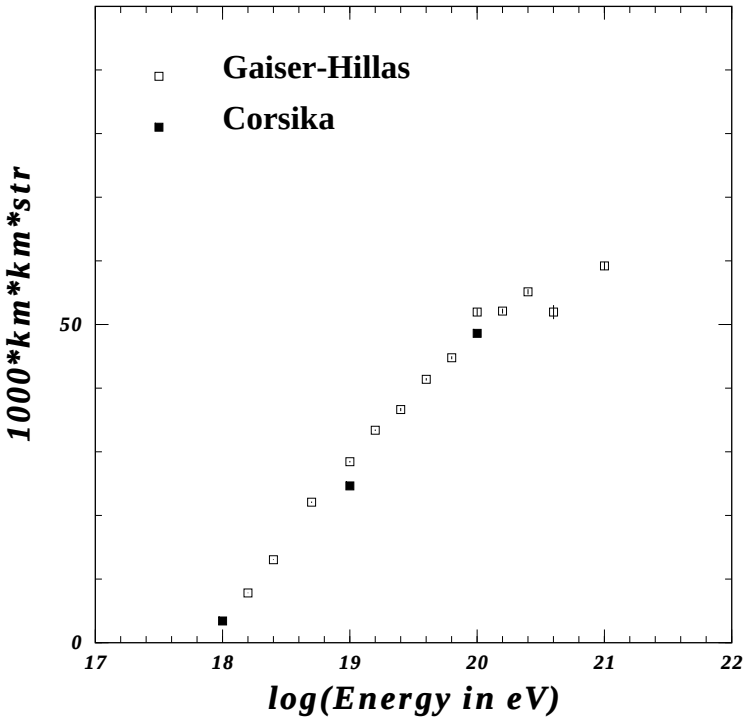

FIG. 4.8: The stereo aperture of TA.

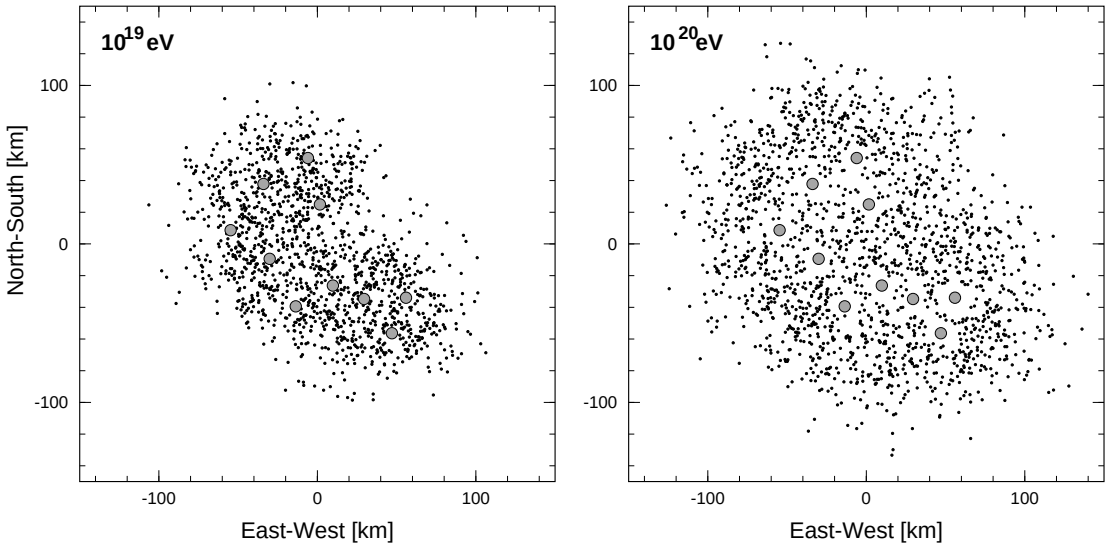

FIG. 4.9: The projection of shower luminous centers to the ground. The shaded circles correspond to locations of the 10 stations.

4.4 Resolutions of Energy, Angle and X_{max}

For the air fluorescence method, there are 3 major factors to influence the resolution of measurement.

- Event reconstruction
- Atmospheric correction
- Pixel calibration (optics and electronics)

The accuracy of event reconstruction is important for all the observables such as the energy, the arrival direction and the shower maximum X_{max}. The atmospheric correction and the pixel calibration are most relevant for the resolution of energy measurement. Besides the resolution, we need to estimate the accuracy of the measurement in absolute scale, which is particularly important for the energy measurement.

4.4.1 Accuracy of arrival direction and X_{max}

The accuracy of event reconstruction is estimated by comparing the value obtained by the event reconstruction with the value used for the event generation. The original X_{max} used for the generation, X_{max}^{gen}, is determined by fitting the generated shower profile with Gaisser-Hillas function [1]. The reconstruction resolution of X_{max} and the arrival direction is plotted in Fig. 4.10 for 10^{20} eV protons generated by the CORSIKA simulation code. All the events satisfying the stereo condition are used except that a few events with large χ^2 in the fitting are excluded. The large χ^2 events mostly correspond to the sizable contributions from the Cherenkov emission. These events amount less than 3% of the total sample and they can be recovered by refining the event reconstruction algorithm in future. It is remarkable that the X_{max} and angular resolution distribution have a well controlled shape without a long tail.

In order to determine the reconstruction resolution, we fitted the distribution of X_{max} by the Gaussian. The angular resolution is determined from the integral distribution (Fig. 4.10(c)) as the point below which 68% of the events are contained. The resolution obtained this way is plotted in Fig. 4.11. It includes the effect of shower fluctuation, the photoelectron statistics and the systematics originated from the fitting procedure. In tne same figure, the resolutions obtained for 10^{18}–10^{21} eV protons are plotted.

4.4.2 Determination of energy

As described in §4.2, the energy determination is based on the calorimetric energy integral, which leads to less sensitivity on unknown assumptions concerning the hadron interactions at extremely high energies. Here let us describe the reliability and systematic uncertainty on our energy determination with the Telescope Array.

[1] We use superscripts ^{gen} and ^{rec} for the value used for the generation and the value obtained by the reconstruction.

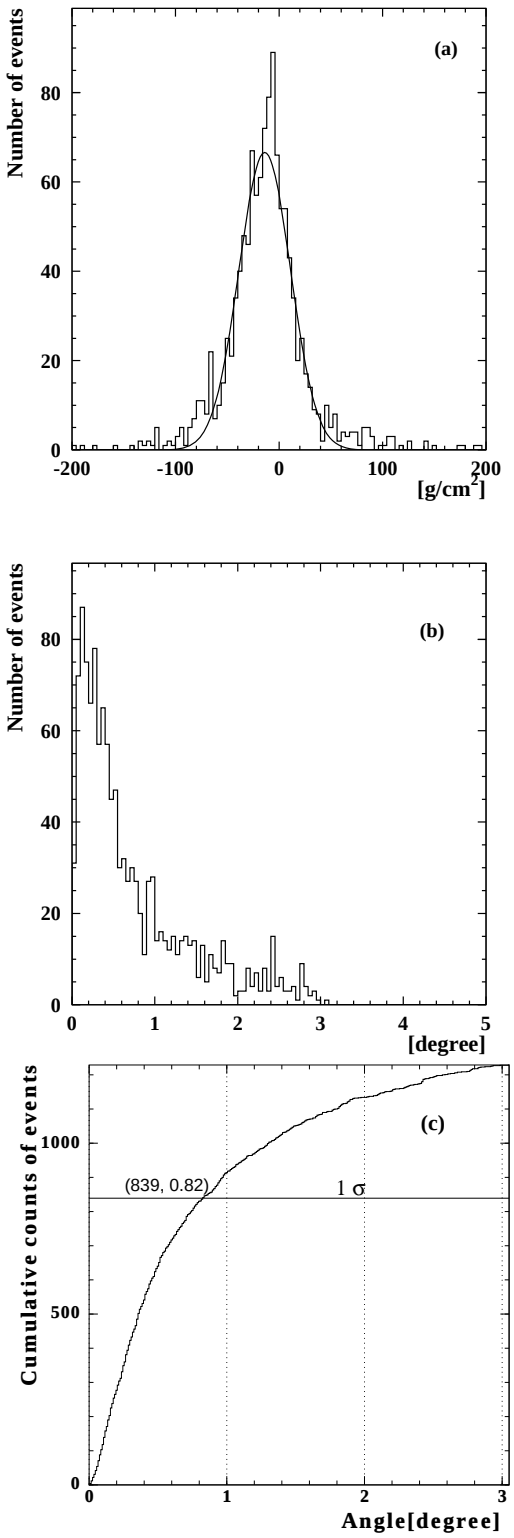

FIG. 4.10: (a) The X_{max} resolution; $X_{max}^{rec} - X_{max}^{gen}$, (b) The distribution of the opening angle between the generated and reconstructed vectors of the arrival direction, (c) Integral form of (b) obtained for 10^{20} eV protons generated by CORSIKA.

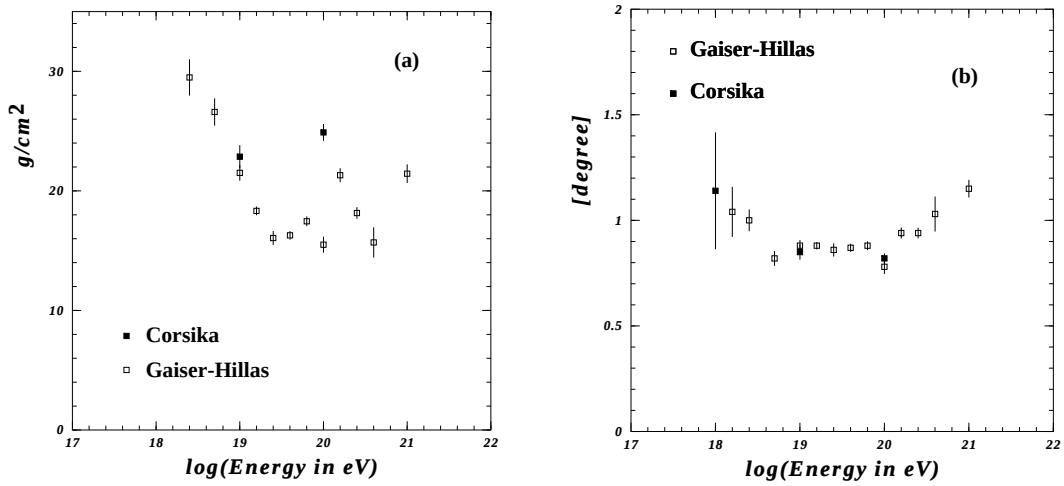

FIG. 4.11: The energy dependence of (a) X_{max} resolution and (b) angular resolution.

Energy of the EAS is determined by Eqs. (4.6) and (4.22):

$$E = \frac{\epsilon_{dep}}{T_{surf} A_{mir}} \int dX N_{pe}(X) \frac{dL}{dX} \frac{4\pi r^2}{\epsilon_{fl} T_M} \left[\int d\lambda f_{fl}(\lambda) T_{ray}(\lambda, X) \epsilon_{det}(\lambda) \right]^{-1} \quad , \qquad (4.23)$$

where $\epsilon_{dep} = \epsilon / X_{rad}$ is energy deposit of charged particles in EAS per unit atmospheric depth, T_{surf} is the transmission factor of the surface reflection, T_M is the transmission factor of propagation of light taking into account the Mie scattering, A_{mir} is area of the mirror, ϵ_{fl} is yield of atmospheric fluorescence, $f_{fl}(\lambda)$ is atmospheric fluorescence spectrum, T_{ray} is the transmission factor due to the Rayleigh scattering in the light propagation, and ϵ_{det} is the overall detection efficiency such as the mirror reflectivity, quantum efficiency of the tube, the inefficiency due to the dead space and the data recording, and the optical filter transmission, all of which is measurable and estimated by the detector Monte Carlo simulation with ray-tracing of the detector optics.

What we observe is N_{pe} in Eq. (4.23), the number of photoelectrons per unit slant depth along the shower axis. The geometrical term $4\pi r^2$, the air fluorescence yield ϵ_{fl}, and the Rayleigh scattering term T_{ray} are determined from the event geometry. Consequently the accuracy of estimation on the event geometry would affect the final resolution of the energy determination. These terms, however, change only gradually along the path integral over dX. Thus energy estimation is rather robust without heavily relying on accuracy of the geometrical term. The energy is then approximately given by

$$\begin{aligned} E \sim & \frac{4\pi R^2}{T_{surf} A_{mir}} \int dX N_{pe}(X) \frac{dL}{dX} \frac{\epsilon_{dep}}{\epsilon_{fl}} \left[T_M \int d\lambda f_{fl}(\lambda) T_{ray}(\lambda, X) \epsilon_{det}(\lambda, X) \right]^{-1} \\ \sim & \frac{4\pi R^2}{A_{mir}} \int dX N_{pe}(X) \frac{dL}{dX} \frac{\epsilon_{dep}}{\epsilon_{fl}} \frac{1}{\epsilon_{overall}(X)} \end{aligned} \quad . \qquad (4.24)$$

Here R is the distance from the station to the shower luminous center and the geometrical factors are represented at the location where the shower cascades has its maximum development. $\epsilon_{overall}$ is the overall transmission factor taking into account the atmospheric extinction and the detector related efficiency ϵ_{det}. This equation shows that our energy determination is based on the slow function of the energy integral term, $\int dX N_{pe}(X)/\epsilon_{overall}$, which gives the stable resolution of our energy estimation by the Telescope Array.

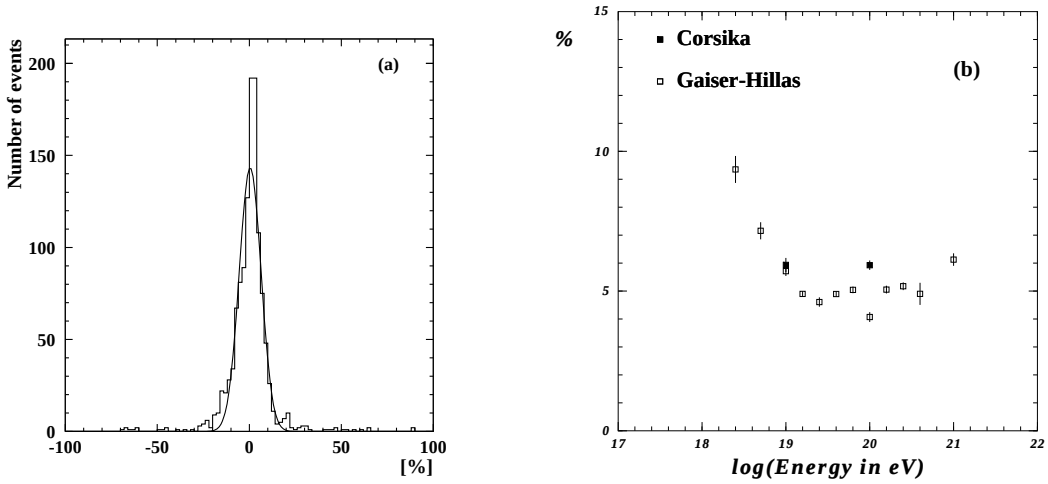

FIG. 4.12: The Energy Resolution distributions;$(E^{rec} - E^{gen})/E^{gen}$ (a) and the resultant energy resolution as a function of shower energy (b)

Figure 4.12(a) shows the energy resolution distribution obtained for 10^{20} eV protons generated by the CORSIKA simulation code. As we expected, it is well represented by the Gaussian distribution, which is crucial for a reliable measurement because the cosmic ray energy spectrum is sharply falling with energy. The resolution is $\sim \pm 6$ % over the wide energy span from 3×10^{18} to 10^{21} eV as shown in Fig. 4.12(b).

As one can see in Eq. (4.24), the systematic uncertainties on the energy estimation mainly arise from the following factors:

- Uncertainties on the detector efficiencies ϵ_{det}, which is calculated by the detector Monte Carlo in the energy determination procedure.
- Uncertainties on the air fluorescence yield ϵ_{fl}.
- Uncertainties on the charged particle energy deposit ϵ_{dep}.
- Energies carried by neutrinos and muons.
- Uncertainties on the factors concerning the atmospheric extinction, T_M and T_{ray}.

The first term, the detector efficiencies are measurable/predictable by our detector calibration and the detector Monte Carlo simulation. The overall uncertainty is estimated to be 10 %.

The second term, the fluorescence yield ϵ_{fl} has been well measured by a laboratory experiment [90]. The yield for low energy electrons below 1 MeV is not quite understood, however, and the uncertainty is given as $\sim$ 10 %.

The energy deposit per unit atmospheric length ϵ_{dep} is based on our knowledges of the particle interactions. It is known to have slight dependences on the age of EAS cascade and the primary mass initiating an EAS. The canonical number for electromagnetic cascades is 2.0 MeV/(g/cm^2). The modified Gaisser Hillas function given by Eq. (4.2) gives 2.31 MeV/(g/cm^2). The CORSIKA full Monte Carlo simulation gives 2.19 MeV/(g/cm^2) with

some dependences on the primary particle mass. The uncertainty have been estimated to be ~ 5 % mainly because of the dependences on the shower age and the threshold energy of secondary electrons and photons in the simulation.

Energies carried by penetrating particles like neutrinos and muons must be taken into account to estimate primary energy of cosmic rays from the air shower energy determined by Eq. (4.23). The full Monte Carlo simulation can calculate the fraction of these missing energies. The CORSIKA simulation gives this fraction as

$$\frac{E_{primary}}{E} = 0.959 - 0.082 \left(\frac{E}{10^{18}\mathrm{eV}} \right)^{-0.15} \quad . \tag{4.25}$$

for average behavior of protons and irons. Uncertainty of 5 % has been estimated due to lack of knowledge of primary mass.

The last term related on the atmospheric extinction is expected to make major contributions to the overall uncertainty on the energy estimation. We discuss the resultant systematics in detail next.

4.4.3 Atmospheric correction

The energy resolution may be significantly affected by the atmospheric correction. In Fig. 4.13, we show a scatter plot of the extinction caused by the Mie scattering vs the distance from the shower luminous center to the station for 10^{20}eV protons. As shown, the average extinction by the Mie scattering reaches 0.7 for showers more than 40 km away, but it saturates beyond this limit.

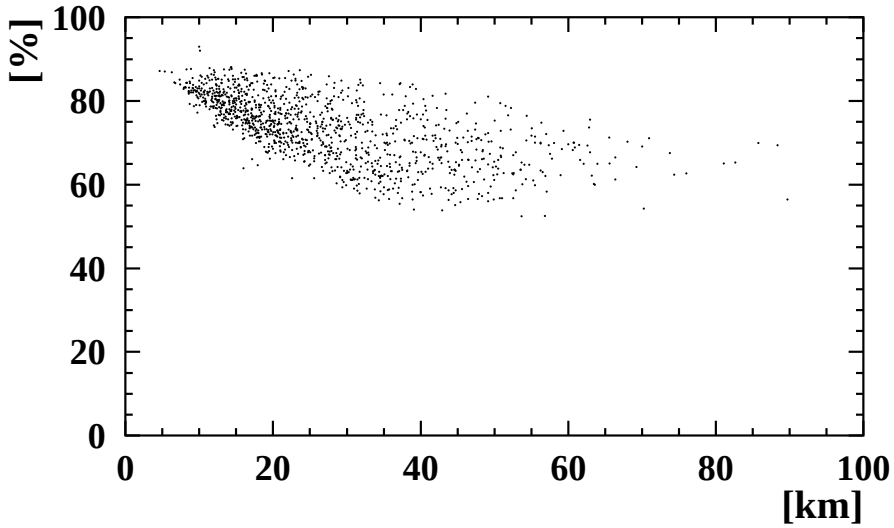

FIG. 4.13: Scatter plot of the distance from the shower luminous center to the station vs Mie extinction. It is plotted for the nearest station to the shower center.

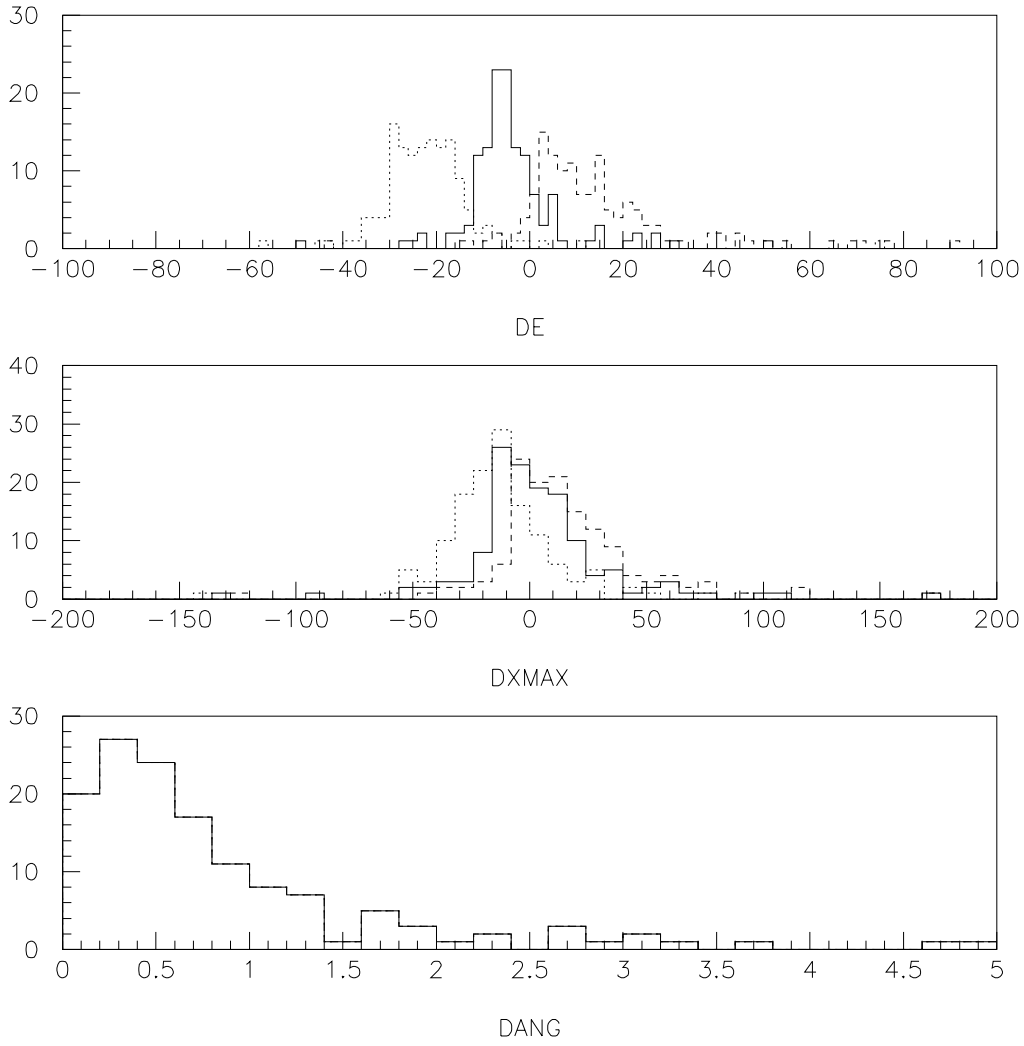

FIG. 4.14: Effect of wrong Mie scattering coefficient. The resolution for energy (DE in unit of %), X_{max} (DXMAX in unit of g/cm^2) and angle (DANG in unit of degree) are plotted. The solid line histogram is reconstructed with correct atmospheric parameters ($L_M = 20$ km and H_M=1.2 km.) The broken line histogram used $L_M = 15$ km and dotted line histogram used $L_M = 35$ km when reconstructed. The H_M was taken 1.2 km for both cases.

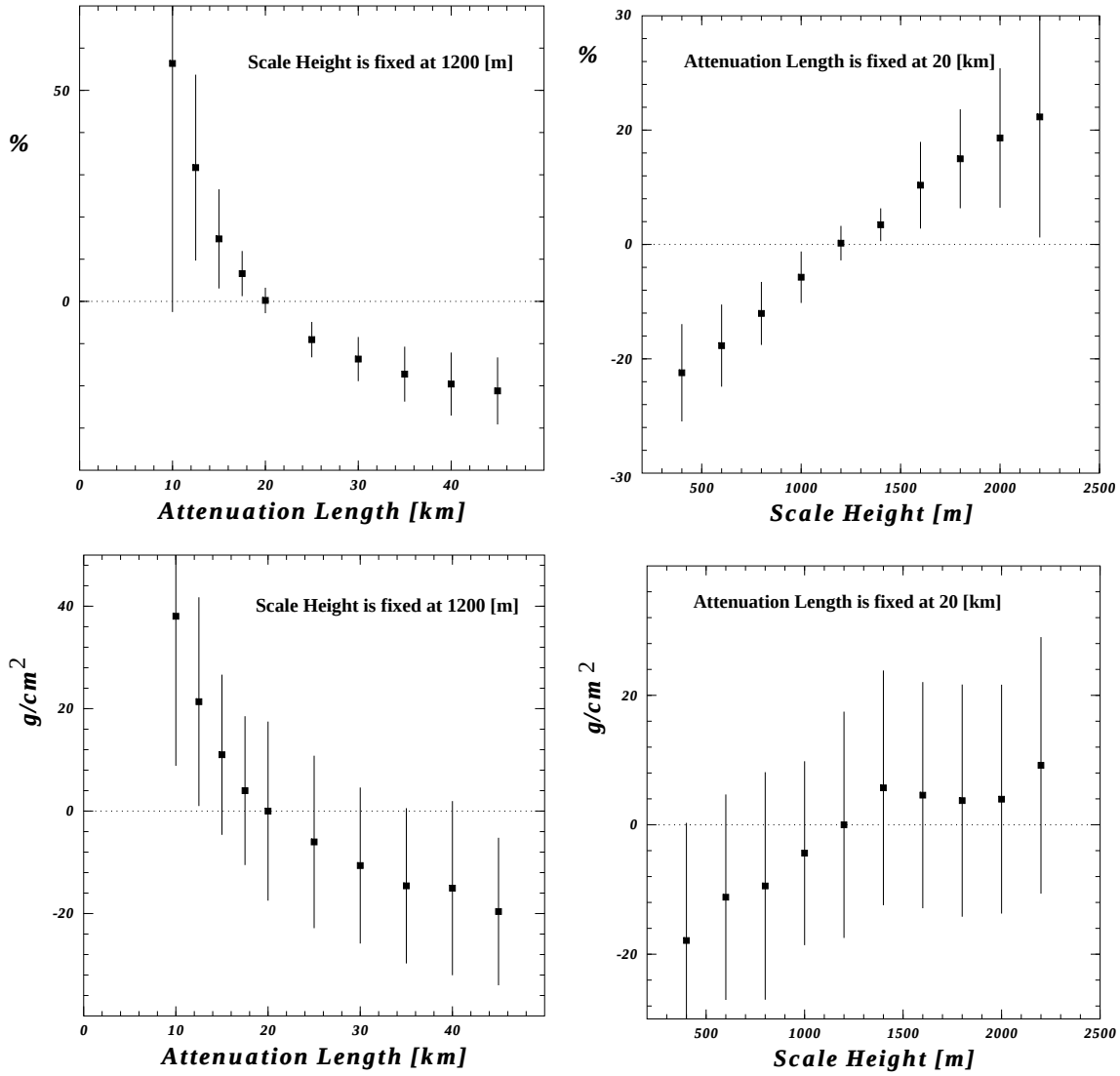

FIG. 4.15: (a) The change of reconstructed energy by using various "wrong" values of L_M and the "correct" value of H_M in reconstruction. The values used for the event generation were L_M=20 km and H_M=1.2 km. The error bar represents the resolution of reconstruction. (b) The same by using various "wrong" values of H_M and the "correct" L_M. (c) The change of reconstructed X_{max} with "wrong" L_M. (d) The same with "wrong" H_M.

The simulation program uses 20 km for the attenuation length by the Mie scattering (L_M in Eq. (4.7)) at the ground level. The density of the scattering center decreases exponentially with the height with the scale height of H_M=1.2 km. Both generation and reconstruction use the same values of L_M and H_M. We studied the effect of the Mie scattering uncertainty by intentionally taking a different set of parameters for the generation and reconstruction of events. An example showing the difference of reconstructed energy, X_{max} and arrival direction for such cases is given in Fig. 4.14. It is seen that event reconstruction with wrong understanding of the atmospheric transparency could lead to both larger systematic shift and poorer resolutions on the energy determination. On the other hand, the angular reconstruction had no influence of wrong atmospheric parameters because our method to determine event trajectories is decoupled from the procedure to reconstruct longitudinal shower profile (see §4.2).

The effect of taking a wrong L_M and H_M for the reconstruction is summarized in Fig. 4.15. Although the systematic shift caused by reconstructions with the wrong parameters is not negligible, it should be remarked that the results suggest that 10% shift of average reconstructed energy is equivalent to $\Delta L_M = {}^{+6}_{-3}$ km, or $\Delta H_M = \pm$ 0.7 km where ΔL_M and ΔH_M are the errors of L_M and H_M. We believe this level of accuracy can be achieved by the laser calibration. The extinction by the Rayleigh scattering can be calculated reliably and its contribution to the systematic uncertainty is negligible compared with the Mie scattering. We estimate that the energy uncertainty arising from the atmospheric correction can be controlled at the level of 10%. The X_{max} was affected by the wrong atmospheric parameters by average shift of $\pm$5 g/cm^2.

4.4.4 Uncertainty of measurement

The measurement of EHE cosmic showers has no convenient way of calibrating the energy scale. However, the accuracy of the measurement can be estimated directly from the uncertainties of the numbers used for the energy calculation. The accuracies we intend to achieve in TA for these numbers are listed in Table 4.2. The major contributions are from the uncertainties of scintillation efficiency, calibration, atmospheric correction and overall shower correction each at the level of 5$\sim$10%. A quadratic sum of all factors in the table gives 20% and this is the accuracy of absolute energy we expect to achieve at TA.

The uncertainty of angle determination is dominated by the reconstruction error already taken into account in the simulation. The absolute alignment of PMT and telescope can be calibrated with an accuracy better than 0.1° by shooting the laser from the center of the station.

The simulation indicates that the value of X_{max} changes depending on which functional shape to be used for fitting the longitudinal profile near the shower maximum. This difference is approximately 15 g/cm^2. The discrepancy between the generated and the reconstructed X_{max} is comparable to this shift as illustrated in Fig. 4.10. We take 15 g/cm^2 as the systematic uncertainty of measuring the X_{max}. It should be noted that the different shower simulation programs predict different X_{max} for the particles with the same energy. For example, X_{max} is 827 g/cm^2 for 10^{20} eV proton by CORSIKA whereas AIRES predicts 863 g/cm^2. The ability of TA to discriminate primary cosmic ray particle mass will be significantly improved if the theoretical understanding of cascade shower improves and the

prediction of the Monte Carlo becomes more reliable.

The resolution and systematic uncertainties of energy, angle and X_{max} measurement is summarized in Table 4.3 for 10^{20} eV protons.

Table 4.2: Estimated systematic uncertainties of energy measurement

Item		Error	Comments
Number of photoelectrons	N^{pe}	5%	
Fluorescence yield	ϵ_{fl}	10%	inc. pressure uncert.
Distance to shower	R	5%	error in R^2
Detection efficiency	ϵ_{det}	10%	5% for mirror, 5% for filter, 8% for PMT, 3% for obscuration.
Energy loss rate	ϵ_{dep}	5%	
Atmospheric correction	T_M, T_{ray}	10%	
Missing energy correction	$E_{primary}/E$	5%	the primary particle mass dependences
T O T A L		20%	quadratic sum of all

Table 4.3: Resolution and systematic accuracy of TA

Observable	(unit)	Resolution	Sys. Uncert.
Energy	(%)	6	20
Angle	(°)	0.8	0.1
X_{max}	(g/cm^2)	18	15

4.5 Detection of EHE Neutrinos

The expected EHE neutrino fluxes are in the range $1 \sim 30\nu$s km^{-2} yr^{-1} sr^{-1} above 10^{19} eV and their detection requires a detector of huge aperture considering the low neutrino cross sections. The standard type underground neutrino telescopes, which observe long-range upward-going muons with effective areas of 0.1 km^2 or smaller, would not be capable of EeV neutrino detection [102]. An alternative detection method is to search for extensive air showers (EAS) initiated by electrons/hadrons produced by neutrinos through the charged current process $\nu_l + N \rightarrow l + X$. Showers developing deep in the atmosphere must be produced by penetrating particles. The Fly's Eye experiment searched for such an event to get an upper bound on the EHE neutrino flux [57, 103]. Similar to the Fly's Eye, the Telescope Array measures EHE cosmic ray air showers using air fluorescence but with much better resolutions and larger aperture. It can reconstruct the EAS development as a function of atmospheric depth with better than 30 g/cm^2 resolution and easily distinguish normally developing showers from deeply penetrating showers (DPS).

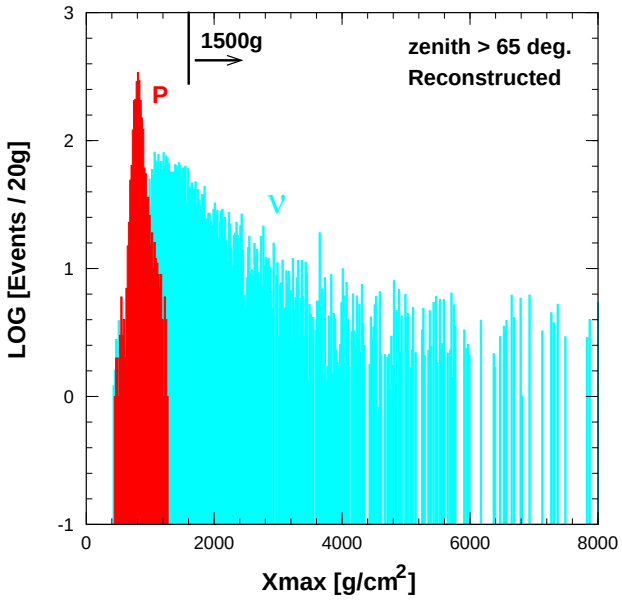

FIG. 4.16: Reconstructed X_{max} distribution for cosmic ray protons with energies of 10^{19} eV or greater (shown by the red hatches) and neutrinos. Number of events of the protons corresponds to one year observation by Telescope Array.

The interaction length of cosmic ray hadrons and gamma rays is $50 \sim 100$ g/cm^2 near 10^{19} eV. Thus the probability of these particles initiating EAS at deeper than 1500 g/cm^2 is $\sim 3\times10^{-7}$, so any shower starting that deep in the atmosphere would be a candidate neutrino event. In fact the miss-reconstructed proton induced showers could constitute a background in the neutrino search because of the tail of distribution of the X_{max} reconstruction errors. It should be remarked, however, that the excellent resolutions of the Telescope Array given by the data criteria as illustrated in §4.5 shows that the discrimination of the proton induced showers from the DPS would be experimentally robust. Figure 4.16 shows the X_{max} distribution for both proton and neutrino induced showers simulated and reconstructed by the TA Monte Carlo. One can see that none of the proton events has left over in the region of X_{max} deeper than 1500 g/cm^2. A search for a DPS with $X_{max} \geq 1500$ g/cm^2 indeed excludes the hadron background.

Detection rates can be obtained by folding the predicted fluxes with the product of the charged current neutrino-nucleon cross section, $\sigma_{\nu N}(E) \simeq 2.82\times10^{-32}(E/10\,\mathrm{EeV})^{0.402}\,\mathrm{cm}^2$ [102], and the acceptance $A(E)$. The following equations give the event rate [53]:

$$\frac{dN}{dt}(\geq E_{\nu_e}) = \int_{E_{\nu_e}}^{\infty} dE'_{\nu_e} J(E'_{\nu_e}) D_\nu(E'_{\nu_e}) \quad , \tag{4.26}$$

where $D_\nu(E_{\nu_e})$ is the "effective aperture" which is folded with the cross section:

$$D_\nu(E_{\nu_e}) = N_A \int_0^{E_{\nu_e}} dE_e \frac{d\sigma_{\nu_e}}{dE_e}(E_{\nu_e}) T(E_e) \quad , \tag{4.27}$$

$$T(E_e) = \int d\Omega (X_\Omega - 1500[\mathrm{g/cm}^2]) A(\Omega, E_e) \quad , \tag{4.28}$$

where σ_{ν_e} is the cross section of the charged current process with the nucleon, E_e is the energy of the produced showers, N_A is Avogadro's number, X_Ω is the slant depth of the atmosphere for the solid angle Ω, and $A(\Omega)$ is the acceptance of the air fluorescence detector for deeply penetrating showers. $T(E_e)$ represents the effective aperture column density (km^2 sr g/cm^2) of the detector for the DPS.

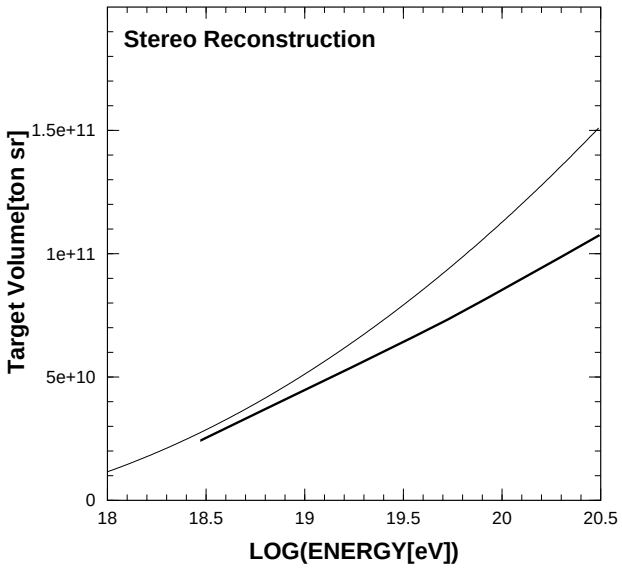

FIG. 4.17: The effective target volume for the DPS. Thick curve: Results obtained by the TA Monte Carlo simulation. Thin curve: Results obtained by the analytical formula.

The Monte Carlo detector simulation can calculate the effective target volume $T(E_e)$. Figure 4.17 shows the results by the simulation. Target volume is $\sim 10^7$ km^2 sr g/cm^2 $\sim 10^{11}$ ton sr for 10^{20} eV showers. The results are consistent with the analytical formula [53] given by

$$T(E_e) \simeq (\frac{N_{st}}{10}) \left[1.1 \times 10^6 \left(\frac{h}{8.4\text{km}}\right) \left(\frac{r_0}{8\text{km}}\right)^{\frac{4}{5}} f^2 - 7 \times 10^5 \left(\frac{h}{8.4\text{km}}\right)^2 \right] \qquad [\text{km}^2\text{sr g/cm}^2], \tag{4.29}$$

where

$$f = 3.3 + \log\left(\frac{E_e}{10^{20}\text{eV}}\right) - \log\left[\frac{n_{th}}{4\sigma} \left(\frac{r_0}{8\text{km}}\right) \left(\frac{e_{eff}}{4\text{m}^{-1}}\right)^{-1} \left(\frac{R_{mir}}{1.5\text{m}}\right)^{-1} \sqrt{\left(\frac{n_{NB}}{10^6\text{m}^{-2}\text{sr}^{-1}\mu s^{-1}}\right)\left(\frac{t_{gate}}{5\mu s}\right)} \right], \tag{4.30}$$

for accounting the detector related S/N, N_{st} is the number of the station, n_{NB} is the night sky photon intensity and t_{gate} is the time window for collecting signal, e_{eff} is the fluorescence light yield from an electron (photons per meter), R_{mir} is the radius of the telescope mirror, h is the atmospheric scale height ($\sim$ 7.5 km), and r_0 is the extinction length of light due to the atmospheric scattering.

The effective aperture $D_\nu(E_{\nu_e})$ is approximately given by

$$D_\nu(E_{\nu_e}) \sim 5 \times 10^{-2} \left(\frac{N_{st}}{10}\right) \left(\frac{E_{\nu_e}}{10^{20}\text{eV}}\right)^{0.402} \left(3.3 + \log\left(\frac{E_{\nu_e}}{10^{20}\text{eV}}\right)\right)^2 \qquad [\text{km}^2\text{sr}]. \tag{4.31}$$

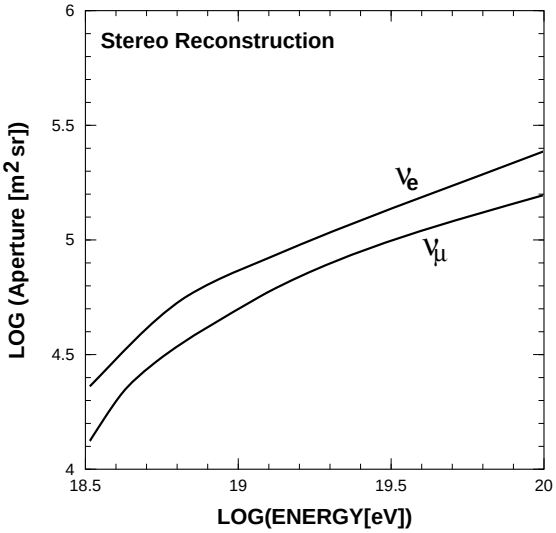

FIG. 4.18: The effective aperture for detection of the EHE neutrinos.

The detailed Monte Carlo simulation together with the numerical integral of Eq. (4.27) has obtained the consistent results as plotted in Fig. 4.18 showing that the Telescope Array has the effective neutrino aperture of ~ 0.3 km^2 sr for energies of 10^{20} eV. Note that the inelasticity for the neutrino-nucleon interactions makes the differences between the aperture for electron-neutrinos and that for muon-neutrinos because high energy muons induced by muon-neutrinos would not contribute detectable air showers.

The expected neutrino event rate for the Top Down models [38] and the "Z-burst" scenario [44] that the EHE neutrino beams colliding with the neutrino dark matter are sources of the highest energy cosmic rays (see §1.4) is summarized in the Tables 4.4 and 4.5.

4.6 Identification of EHE γ-rays

Some viable models to explain the EHE cosmic rays have predicted that the major primary composition at extremely high energies is γ-rays. A photon has no electric charge and would neither be bended by the galactic nor extragalactic magnetic field. Identification of the possible γ-ray population would be thus of great importance to resolve the mystery of the EHE cosmic rays.

It has been suggested that the photon-induced air showers might have different longitudinal development profile than hadron induced showers. The LPM effect [104, 105] leads to very slow shower development with significant fluctuations due to the possible mechanisms of suppression of bremsstrahlung and pair creation processes at extremely high energies. On the other hand, the geomagnetic cascading starting with electron-positron pair creation in the geomagnetic field at out of atmosphere [106, 107] also affects shower curve but with much *faster* development than those of LPM showers and the feature is strongly related to the arrival direction. In this section we report the differences on longitudinal development initiated by hadronic and γ-ray primaries, and discuss on a possibility of γ-ray identification.

Table 4.4: The expected event rate [/10yr] for some viable Top Down scenarios explaining the cosmic rays at least above 100 EeV.

Modes	Fragmentation	m_X [GeV]	Event Rate $E \geq 3 \times 10^{18}$ eV	Event Rate $E \geq 10^{19}$ eV
qq	SUSY	10^{16}	1.271(ν_e) 1.476(ν_μ)	0.837(ν_e) 0.986(ν_μ)
qq	no-SUSY	10^{16}	0.492(ν_e) 0.604(ν_μ)	0.379(ν_e) 0.466(ν_μ)
$\nu\nu$	-	10^{13}	7.511(ν_e) 6.195(ν_μ)	6.627(ν_e) 5.095(ν_μ)
$\nu\nu$	-	10^{14}	1.000(ν_e) 1.306(ν_μ)	0.194(ν_e) 0.186(ν_μ)

Table 4.5: The expected event rate [/10yr] for the Z-burst scenario [44].

f_ν^*	Event Rate $E \geq 10^{19}$ eV	Event Rate $E \geq 10^{20}$ eV
1000	0.154(ν_e) 0.331(ν_μ)	0.075(ν_e) 0.179(ν_μ)
300	0.459(ν_e) 1.005(ν_μ)	0.227(ν_e) 0.552(ν_μ)
20^a	5.302(ν_e) 11.722(ν_μ)	2.649(ν_e) 6.448(ν_μ)

* the overdensity factor of eV mass neutrino dark matter over a supercluster scale of ~ 5 Mpc.
^{a} the lower bound allowed by the EGRET diffuse γ-ray limit. This case sets an upper bound for EHE neutrino intensity in the Z-burst scenario.

4.6.1 Simulation of hadronic and γ-ray shower

To study on the profile of air shower development initiated by γ-rays and hadrons (proton or iron) the AIRES [108] simulation code with QGSJET hadronic interaction model has been used in this work. AIRES code uses EGS4 program code for simulation of electromagnetic showers and the LPM effect is included, but the interaction with magnetic field is not incorporated in itself. We developed our own code for electromagnetic cascading in the geomagnetic field. To simulate showers from EHE γ-ray showers, first we modeled cascading in the geomagnetic field starting with a single photon far away from the Earth's surface down to the top of atmosphere. Then secondary particles that reach at the top of atmosphere were set as an input for AIRES code. An air shower initiated by a single EHE γ-ray is constructed as a superposition of lower energy γ-ray subshowers.

Main elementary processes leading to particle multiplication in magnetic field are magnetic bremsstrahlung and magnetic pair production. It is well known that the essentially non-zero probabilities for magnetic bremsstrahlung and pair production require both strong field and high energies [109]. The relevant parameter determining the criteria for this is:

$$\chi = \frac{\varepsilon}{mc^2}\frac{H}{H_{cr}} \qquad , \tag{4.32}$$

where ε is the particle energy, H is the magnetic field strength (the component normal to the particle trajectory), m is the electron mass and $H_{cr} = 4.41 \times 10^{13}$ G.

The total probabilities (cross sections) for radiation and pair production for a given value of the magnetic field strength depend only on χ. Magnetic pair production has significant probability for $\chi \geq 0.1$ but for effective shower development one needs even higher values of χ ($\chi \geq 1$) because the radiated photon spectrum becomes harder with increasing χ .

We used the differential probabilities (per unit length) for magnetic bremsstrahlung and magnetic pair production [110] given by the expressions:

$$\begin{aligned} \pi(\varepsilon,\omega)\,d\omega &= \frac{\alpha m^2}{\pi\sqrt{3}}\frac{d\omega}{\varepsilon^2}\left[\left(\frac{\varepsilon-\omega}{\varepsilon}+\frac{\varepsilon}{\varepsilon-\omega}\right)K_{\frac{2}{3}}\left(\frac{2u}{3\chi}\right)-\int\limits_{\frac{2u}{3\chi}}^{\infty}K_{\frac{1}{3}}(y)\,dy\right], \\ \gamma(\omega,\varepsilon)\,d\varepsilon &= \frac{\alpha m^2}{\pi\sqrt{3}}\frac{d\varepsilon}{\omega^2}\left[\left(\frac{\omega-\varepsilon}{\varepsilon}+\frac{\varepsilon}{\omega-\varepsilon}\right)K_{\frac{2}{3}}\left(\frac{2u_1}{3\chi}\right)+\int\limits_{\frac{2u_1}{3\chi}}^{\infty}K_{\frac{1}{3}}(y)\,dy\right], \end{aligned} \tag{4.33}$$

where ε and ω are the electron and photon energy and $u = \frac{\omega}{\varepsilon-\omega}$, $u_1 = \frac{\omega^2}{\varepsilon(\omega-\varepsilon)}$ .Parameter χ was defined above. Here $\hbar = c = 1$. $K_\nu(z) = \int\limits_0^\infty e^{-zch(t)}\mathrm{ch}(\nu t)\,dt$ is a modified Bessel function known as MacDonald's function.

While for $\chi \gg 1$ (strong field) the electromagnetic cascade develops similarly to the cascade in matter[111], in the region $\chi \leq 1$ (Earth's magnetic field) the photon interaction length increases sharply with decreasing photon energy. Electrons continue to radiate and the shower becomes a bunch of photons carrying $\geq 94-95\%$ of the primary energy.

In our simulation we used the International Geomagnetic Reference Field (IGRF) and World Magnetic Model (WMM) which provides a good approximation of the Earth's magnetic field up to 600 km from the ground and its extrapolation above this altitude.

We have simulated the electromagnetic cascading by injecting EHE γ-rays at a distance of 3 Earth's radii from the surface of the Earth. An γ-ray and secondary particles are propagating via pair production and bremsstrahlung. Interaction probabilities are calculated each step of of every 10 km. Only particles above threshold energy of 10^{15} eV were followed in the simulation until they reach at the top of atmosphere (50 km above the ground level). This threshold energy is enough low to neglect the contribution of sub threshold particles in the cascade.

Interaction probabilities of incident γ-rays with the geomagnetic field has been estimated for different zenith and azimuthal angles of their arrival directions. Figure 4.19 shows probability maps for γ-ray conversion for 4 different primary energies in coordinates of zenith and azimuthal angles. The region with a smaller probability is centered at 39° in a zenith angle and a direction of 14° west from the south. The size of this "window" is shrinking quickly with an increase of primary energy, and most primary γ-rays with energies greater than 10^{20}eV initiate the geomagnetic cascade before the top of atmosphere. Average energy spectra of secondary γ-rays and electrons at the top of atmosphere are shown in

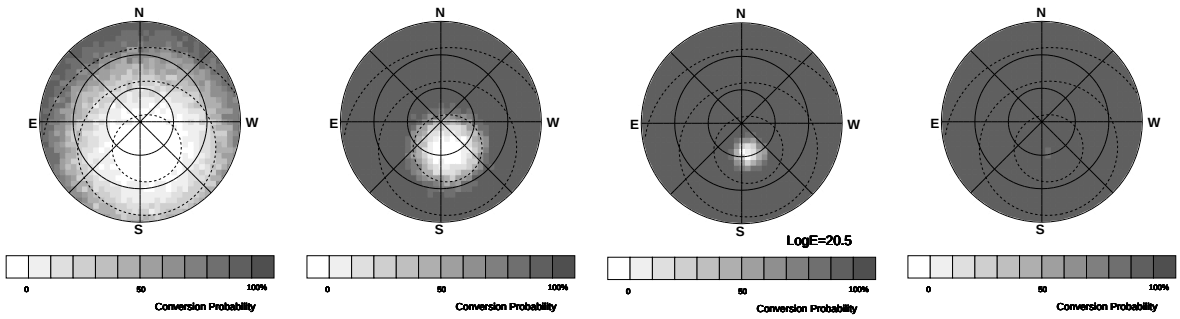

FIG. 4.19: Maps of γ-ray conversion probability for primary energies of $10^{19.5}$ eV, $10^{20.0}$ eV, $10^{20.5}$ eV, and $10^{21.0}$ eV. Inner Circles show zenith angles of 30° and 60° and horizon. Dashed lines correspond to the angular distances of 30°, 60° and 90° to the inverse direction of geomagnetic field at Utah.

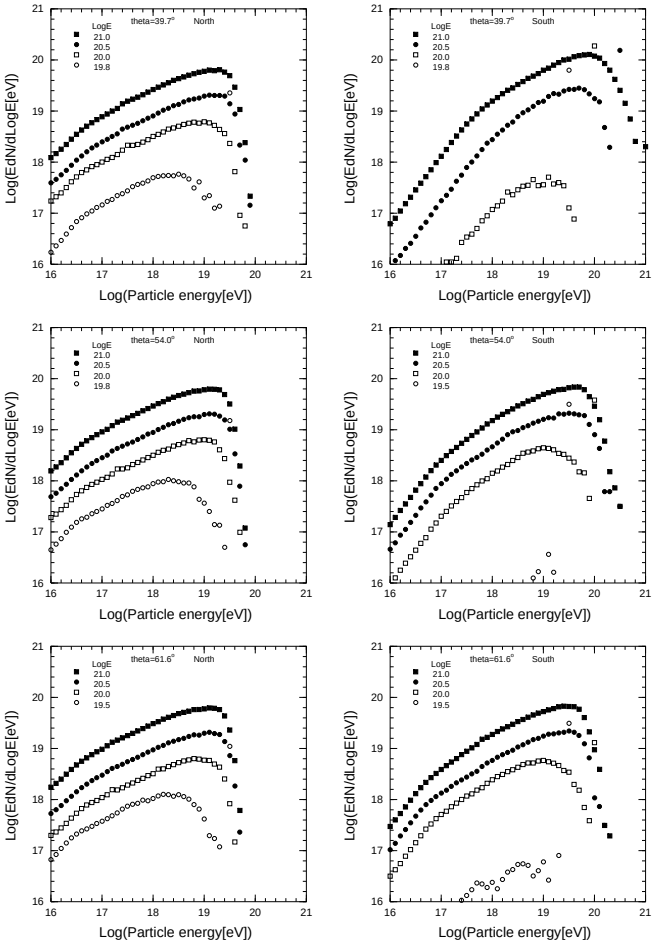

FIG. 4.20: Energy weighted spectra of secondary γ-rays and electrons at the top of atmosphere for primary γ-ray energies of $10^{19.5}$ eV (open circles),$10^{20.0}$ eV (open square), $10^{20.5}$ eV (solid circles), and $10^{21.0}$ eV (solid square) with 3 different zenith angles (39.7°, 54.0° and 61.6°). Azimuthal angles are assumed as north and south.

Fig. 4.20. Energy spectra for primary γ-rays with energies of $10^{19.5}$, $10^{20.0}$, $10^{20.5}$ and $10^{21.0}$eV are drawn in each frame. Zenith angles are sampled in 39.7°, 54.0° and 61.6° and azimuthal angles are assumed as north and south. Shapes of energy spectra change with different arrival directions at a fixed primary energy, and primary γ-rays without interaction to geomagnetic field could be found at the right end of energy spectra in specific cases, which makes dominant contributions to the fluctuation of the cascade profile due to the LPM effect.

Each secondary γ-ray and electron generated by the geomagnetic cascade initiates electromagnetic sub air showers. Air shower simulation has been performed using the AIRES code with QGSJET hadronic interaction model of thinning level of 10^{-5}. Next, we present the feature of the electromagnetic air shower profiles after the geomagnetic cascades.

4.6.2 The Longitudinal development of γ-ray induced showers and its identification

Shower characteristics depend on primary energy and arrival direction because the LPM effect and cascading in the geomagnetic field are affected by particle energy and geomagnetic field strength.

Examples of individual shower developments initiated by primary γ-rays are shown in Fig. 4.21. Primary γ-rays with energies of $10^{19}, 10^{20}$ and 10^{21}eV and zenith angle of 54.0° and 61.6° are shown in these plots. Shower developments from directions of south and north are shown in left and right figures, respectively. Shower developments with $E_0 = 10^{20}$eV from south are largely fluctuated in comparison with ones of other primary energies, as seen in Fig. 4.21. The reason is that the LPM effect contributes strongly to a shower development of γ-ray which does not interact with the geomagnetic field. On the other hand, developments of showers from north and/or ones with much higher primary energy show faster profiles with smaller fluctuations due to the geomagnetic cascading process.

Figure 4.22 shows average X_{max} as a function of primary energy. Average X_{max} of γ-ray primary has been calculated with zenith angles of 54.0° and 61.6°(open circles and crosses,respectively) and the cases of south/north arrival directions. Ones of proton and iron primaries are also plotted with solid and broken lines in the same figure. Though average X_{max} of proton and iron showers are increasing with a constant rate(elongation rate), one of γ-ray shower has much larger elongation rate in comparison with hadronic showers and the rate becomes a larger because of the LPM effect. The geomagnetic cascading starts its contributions to air shower development above energies of several times 10^{19}eV which depends on the arrival direction of γ-ray. Then, average X_{max} is decreasing and reaches at the minimum values.

The X_{max} distributions for showers initiated by protons and γ-rays with energy of $10^{19.5}$, 10^{20} and $10^{20.5}$ eV and zenith angle of 39.6°, 54.0° and 61.6° are shown in Fig. 4.23. All distributions here are shown as ones after taking into account a detector resolution to determine X_{max} of $\sim$ 30 g/cm^2. Typically, X_{max} distribution of γ-ray with energy of 10^{20} eV and zenith angle of 54.0° distributes broadly because LPM showers and showers with geomagnetic cascading effect are mixed together.

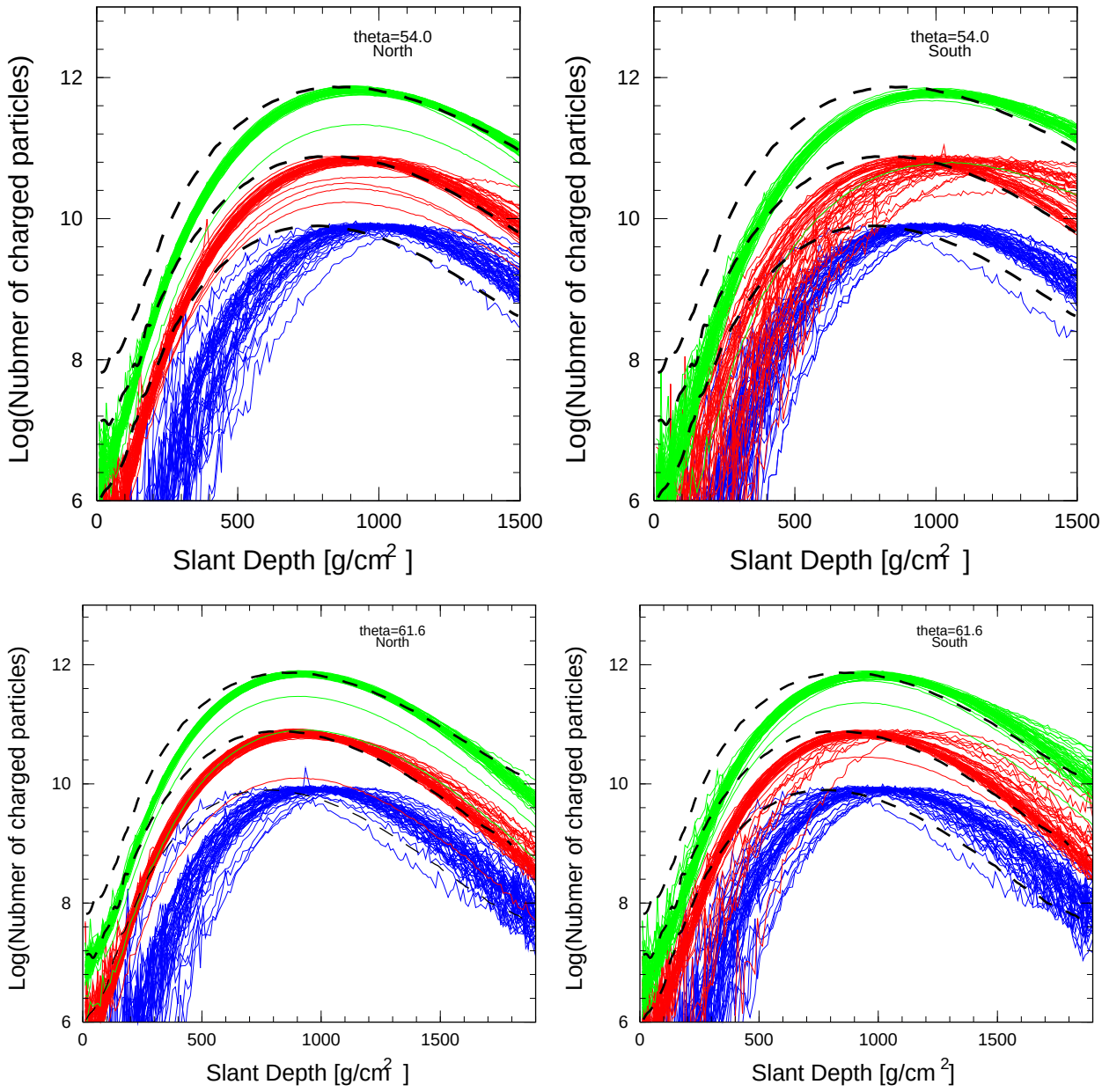

FIG. 4.21: Longitudinal developments of individual showers initiated by γ-rays with energies of 10^{19} eV, 10^{20} eV, and 10^{21} eV with various injection directions. Left and right figures correspond to ones of showers from north and south, respectively. Broken lines show average developments of proton initiated shower with same energies.

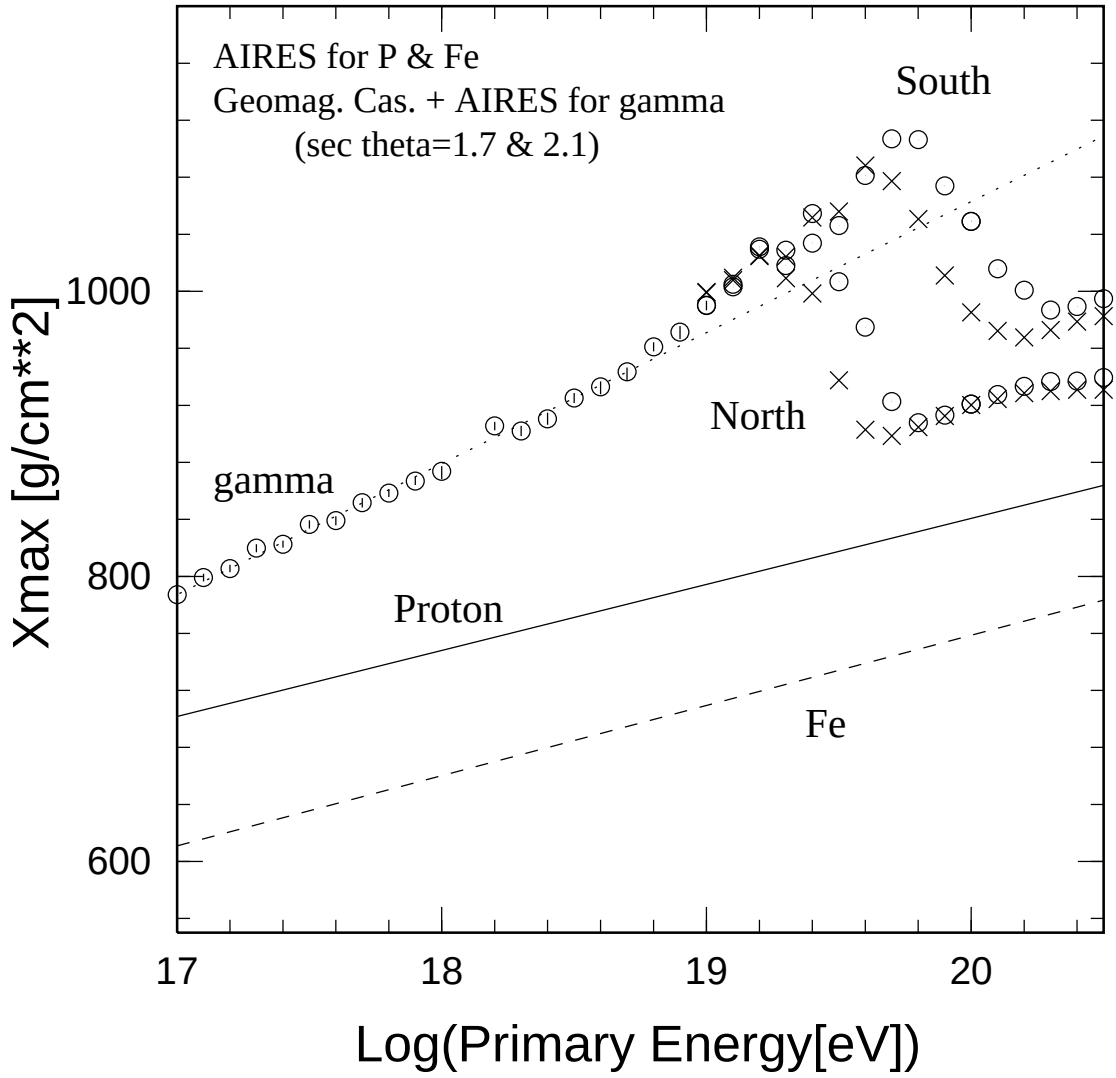

FIG. 4.22: Average X_{max} for showers initiated by proton, Fe and γ-ray as a function of primary energy. Proton and Fe showers were simulated with AIRES-QGSJET. X_{max} of γ-ray showers from south and north with zenith angles of 54.0° and 61.6° are shown.

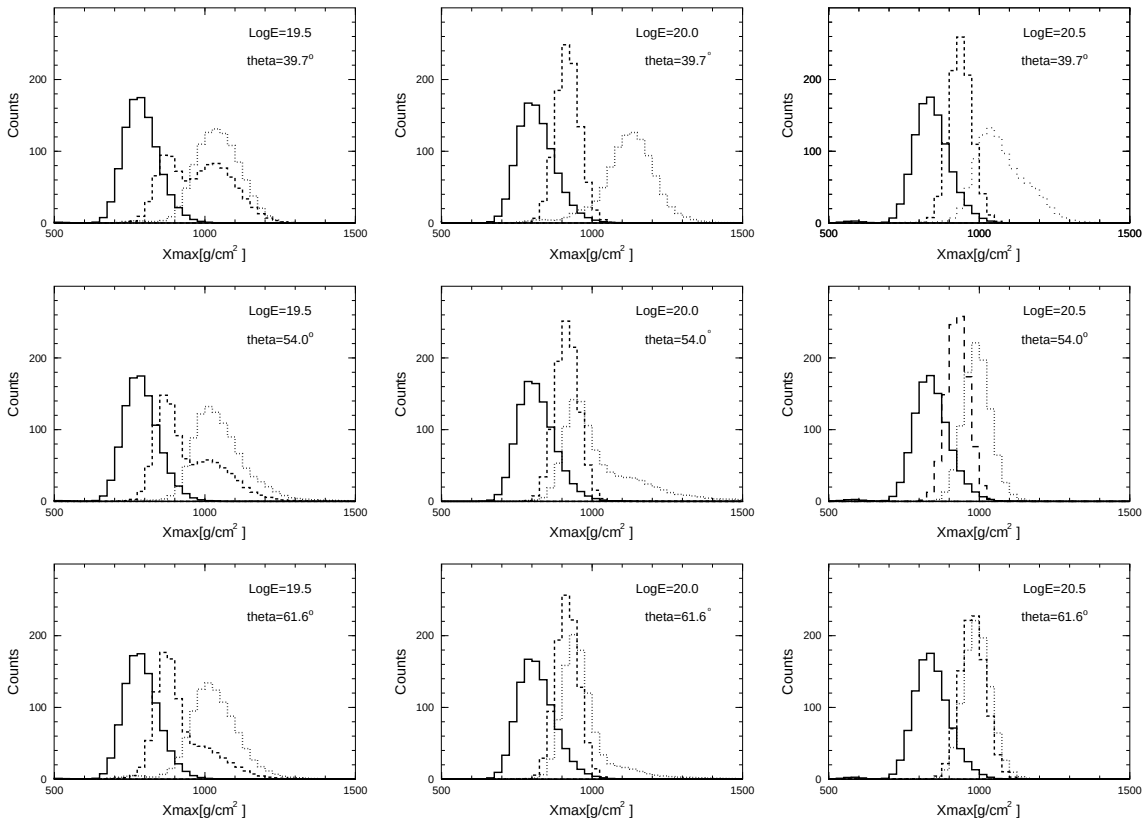

FIG. 4.23: X_{max} distributions for proton and gamma-ray showers with energies of $10^{19.5}$eV, 10^{20}eV and $10^{20.5}$eV (left, center and right, respectively). Zenith angles of 39.7°, 54.0° and 61.6°(top, center and bottom, respectively) are assumed. X_{max} distributions of gamma-ray showers with arrival directions from south and north are shown in separately. All distributions here are shown as ones after taking into account a detector resolution for X_{max} of $\sim 30 g/cm^2$.

4.7 The Observational Power to Distinguish Different Models

We have seen the capabilities of the Telescope Array to measure the highest energy cosmic rays. Now the question is *how* we will be able to distinguish the different models to resolve the long-standing mystery of their origin with the expected power of the detectors. Our observations consist mainly of the energy spectrum, the primary mass composition, and the arrival directions of the energetic particles. The proposed models have their own predictions that can be measurable by our detector. Let us show some examples. Figure 4.24 illustrates our typical discrimination power by measurement of the energy spectrum. It is clearly seen that the spectrum is reconstructed well enough to show whether the GZK cutoff indeed exists or not.

The newly proposed scenarios such as the Top Down models and the neutrino Z-burst model have predicted the "new" population of cosmic rays dominating above 10^{20} eV

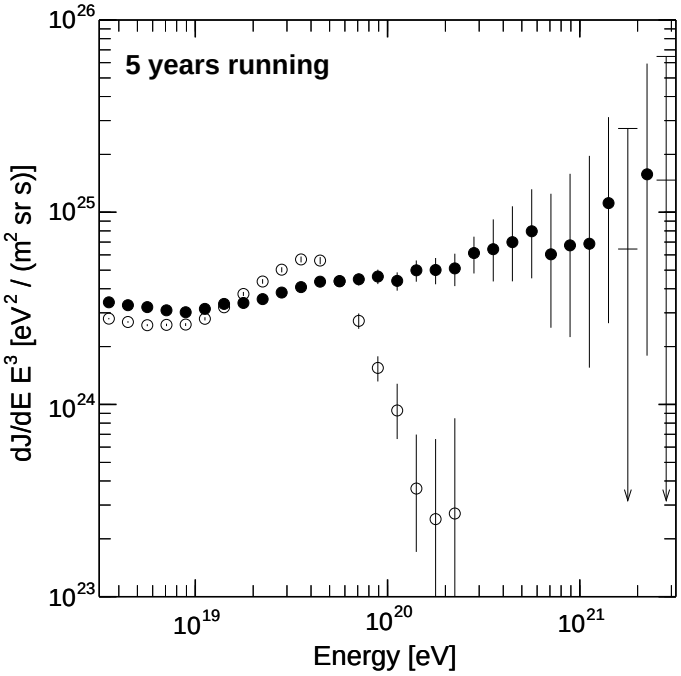

FIG. 4.24: 5 years observation of the energy spectrum by the Telescope Array. Closed circles show the case if the spectrum simply extends well beyond 10^{20} eV [4] while open circles represent the "standard model" with the GZK cutoff assuming the sources are distributed homogeneously in the Universe [17].

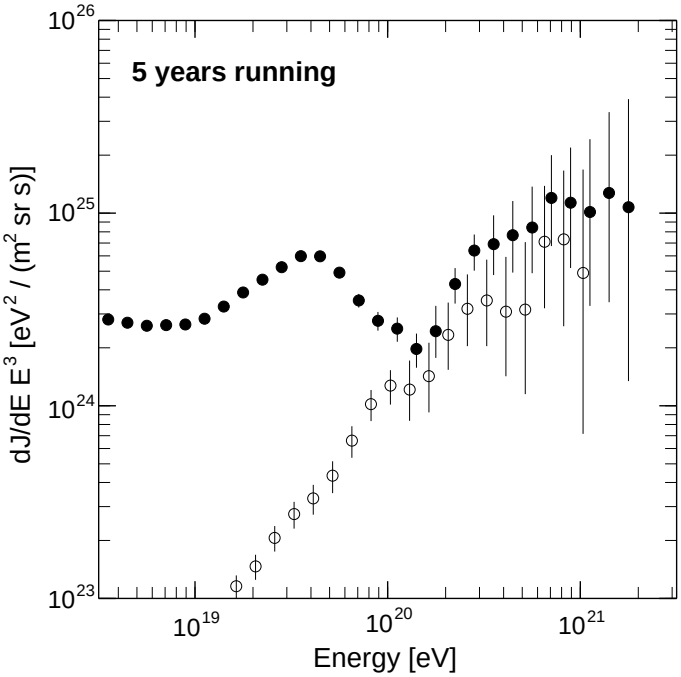

FIG. 4.25: 5 years observation of the energy spectrum by the Telescope Array if the highest energy cosmic ray has a new population dominating above 10^{20} eV as predicted by the Z-burst or Top Down models. open circles represent the primary γ-ray component predicted by the Z-burst model [44].

which would be created by decay of the supermassive particles [33] or cascading initiated by superhigh energy astrophysical neutrino beams [45, 48]. In this case the Telescope Array should see the new component extending well beyond 10^{20} eV. As illustrated in Fig. 4.25, the observation for 5 years would be enough to detect these superhigh energy particles that become predominant after the GZK cutoff. The dip structure appears at 10^{20} eV if the low energy component presumably radiated from the radio galaxies, the most favorite candidates of the high energy cosmic ray emitters, exhibits the GZK cutoff as expected from our standard GZK picture. This would be a strong signature to suggest the Top Down/Z-burst models that are necessarily associated with the hard energy spectrum ($\sim E^{-2}$) extending to 10^{21} eV or even higher.

It should be noted that these models lead to primary γ-ray flux that is comparable or higher than nucleon intensity with energies above 10^{20} eV. As described in §4.6, our capability to measure the longitudinal shower profile gives significant sensitivity to identify primary γ-rays if they exist. As shown in Fig. 4.25, our sensitivity would be good enough to detect the predicted γ-rays component if these models are correct.

Because trajectories of γ-rays would not be bended by any magnetic field, the most energetic particles are able to be traced back exactly to their emission point where one can find counterparts of the astronomical objects like AGNs or GRBs. Five years observation by the Telescope Array is expected to detect ~ 250 events with energies greater than 10^{20} eV, and at least more than 30 % of them is predicted to be γ-rays. This indicates that we will have a fairly good chance to see many triplets or more dense event clusters if the possible small-scale anisotropy AGASA has seen is real. Whether we find astronomical counterparts in their directions and whether the counterparts are within the GZK horizon or not would be direct evidence to identify the highest energy cosmic ray sources, which resolves how the Universe produce such energetic particles, our long-standing astrophysical puzzle.

4.8 Detection of Active Galactic Nuclei Neutrino

In this section, we describe the potential to detect neutrinos of energies more than 10^{16}eV through deeply penetrating air showers using TA. Assuming some simple conservative trigger and selection requirements with a monocular detection technique which uses each detector station for air showers in an independent way, we obtain the acceptance for deeply penetrating air showers as induced by high energy neutrinos by Monte Carlo method. We then give the expected event rates for two neutrino fluxes as predicted in different proton AGN models.

Neutrinos produce showers in most interactions with the atmosphere which are of different nature depending on the process in consideration. We consider both deep inelastic charged and neutral current interactions which always produce hadronic showers. In the case of charged current electron neutrino interactions the emerging electron contributes in addition a pure electromagnetic shower carrying a large fraction of the incoming particle energy. We will ignore the resonant cross section because it is only significant near the peak of the cross section which occurs at an incoming neutrino energy of 6.4 PeV, well below the region of high efficiency for the TA project.

For a neutrino flux dI_ν/dE_ν interacting through a process with differential cross section $d\sigma/dy$, where y is the fraction of the incident particle energy transferred to the target, the event rate for deeply penetrating showers can be obtained by a simple convolution:

$$Rate[E_{sh} > E_{th}] = N_A \rho_{air} \int_{E_{th}}^{\infty} dE_{sh} \int_0^1 dy \frac{dI_\nu}{dE_\nu}(E_\nu) \frac{d\sigma}{dy}(E_\nu, y) \epsilon(E_{sh}) \qquad , \qquad (4.34)$$

where N_A is Avogadro's number and ρ_{air} is the air density. The energy integral corresponds to the shower energy E_{sh} which is related to the primary neutrino energy E_ν in a different way depending on the interaction being considered. ϵ is a detector acceptance, a function of shower energy, which corresponds to the volume and solid angle integrals for different shower positions and orientations with respect to the detector.The function is different for showers induced by charged current electron neutrino interactions from those arising in neutral current or muon neutrino interactions. This is because hadronic and electromagnetic showers have differences in the particle distributions functions, particularly for muons. For $(\nu_e + \overline{\nu}_e)N$ charged current interactions, we take the shower energy to be the sum of hadronic and electromagnetic energies, $E_{sh} = E_\nu$. For $(\nu_\mu + \overline{\nu}_\mu)N$ charged current interactions and for neutral current interactions, we take the shower energy to be the hadronic energy, $E_{sh} = yE_\nu$. To simplify the event rate evaluations, here we neglect the distribution of $\frac{d\sigma}{dy}(E_\nu, y)$ as a function of y replacing it into $\frac{d\sigma}{dy}(E_\nu, y = 0.2)\delta(y - 0.2)$ in Eq. (4.34) because $< y > \sim 0.2$ does not depend on the primary energy beyond 10^{16}eV in both cases of charged and neutral current interactions [112].

Assuming optimized efficiency for triggering on nearby as well as distant events as described in a later section on electronics and neglecting angular factor and Mie scattering attenuation, an estimate of signal to noise generated in a time during which the track is in view of a PMT is given by:

$$\frac{S}{N} = \frac{N_e N_\gamma}{4\pi} \left(\frac{c}{B}\right)^{1/2} \frac{e^{-r/\lambda_R}}{R_P^{3/2}} \left(\frac{\epsilon D^3}{d}\right)^{1/2} ,$$

where N_e is the number of electrons in the air shower generating the light, N_γ is the fluorescent yield which is measured to be $\sim$5 photons/electron/m, B is the night sky background at new moon phase, which is measured to be $\sim 2 \times 10^5$ photons m^{-2} sr^{-1} μs^{-1} over the wave length range 310–440 nm including atmospheric airglow, R_P $R_P$is the impact parameter, λ_R is the Rayleigh scattering length $\sim$ 18 km, ϵ is the overall optical efficiency for converting photons into photoelectrons, d and D are the diameters of the PMT and mirror aperture respectively. Next, we convert electron size N_e to energy in order to obtain an estimate for energy triggering thresholds. We take [113]:

$$E = 1.6 \times 10^{-9} N_e \qquad ,$$

where E is the primary energy in EeV. Also assuming $r = R_P$, $\epsilon = 0.2$, $d = 0.06$m, and $D = 3$m, a crude estimate of the energy threshold is given by:

$$E_{th}[\text{EeV}] = 10^{-4} \left(\frac{S}{N}\right) R_P^{3/2} e^{R_P/\lambda_R} \qquad ,$$

where R_P is in km. E_{th} as a function of R_P in cases of $S/N = 2$ and 4 is shown in Fig. 4.26. This simple estimate suggests that the sensitive TA detector optics and readout devices should allow us the lower detectable energy threshold of 10^{16} eV and the more statistics for AGN neutrino events because of the steep slope of the flux spectrum shown in the previous section. This is a good advantage of the TA detector. Furthermore realistic acceptance estimates from Monte Carlo simulation study for neutrinos as a function of the primary energy will be described just later.

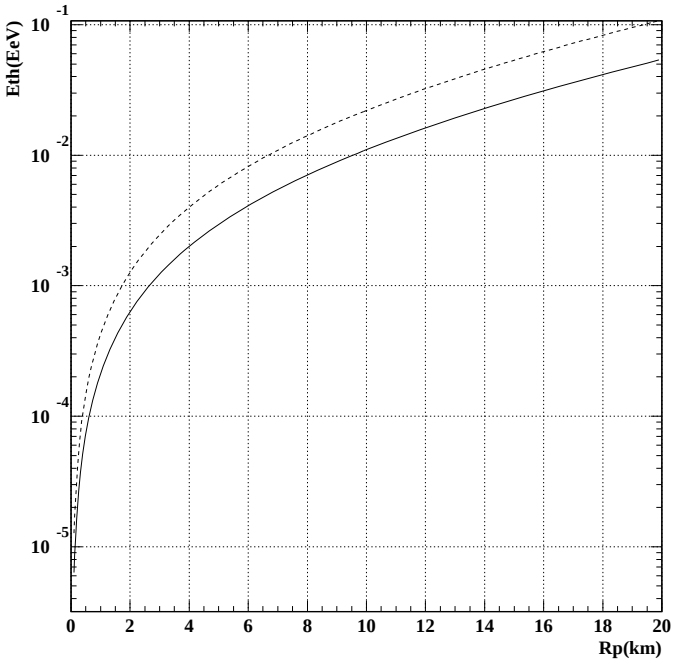

FIG. 4.26: A simple estimate of the minimum detectable energy in EeV as a function of impact parameter R_P in km in cases of PMT trigger levels $S/N = 2$ and 4.

Here we use new calculations of the cross sections for charged-current and neutral current interactions of neutrinos with nucleons [114, 112], according to the CTEQ4-DIS (deep inelastic scattering) parton distributions [115]. The CTEQ4-DIS parton distributions take account of new information about the parton distributions within the nucleon [116] using more accurate and extensive DIS data than before from New Muon Collaboration (NMC) [117]and DESY ep collider HERA [118, 119], as well as new data from E665 [120]. The cross section for the charged-current reaction $\nu_l N \rightarrow l^- + anything$ as a function of the neutrino energy E_ν is shown in Fig. 4.27 (thin solid line). At low energies the charged-current cross section σ_{CC} rises linearly with E_ν. For energies exceeding about 10^4 GeV, the cross section is damped by the W-boson propagator. Also Fig. 4.27 shows the neutral-current cross section σ_{NC} for the reaction $\nu_l N \rightarrow \nu_l + anything$ (dashed line), together with σ_{tot}, the sum of charged-current and neutral-current cross sections (thick solid line). Since the valence contribution is negligible E_ν >10^6 GeV, νN and $\overline{\nu} N$ cross sections become equal. For 10^{16} eV$\leq E_\nu \leq 10^{21}$ eV, the CTEQ4-DIS cross sections are given within 10% by:

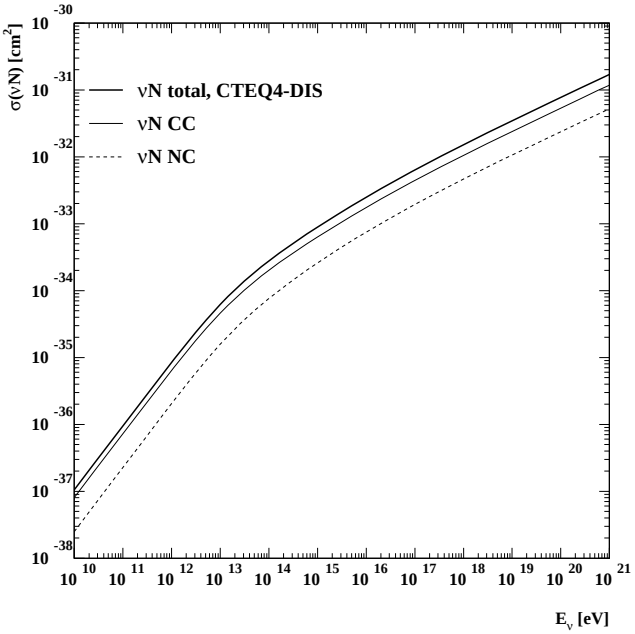

FIG. 4.27: Cross sections for interactions according to the CTEQ4-DIS parton distributions: dashed line $\sigma(\nu_l N \rightarrow \nu_l + anything)$; thin line, $\sigma(\nu_l N \rightarrow l^- + anything)$; thick line, total (charged-current plus neutral-current) cross section.

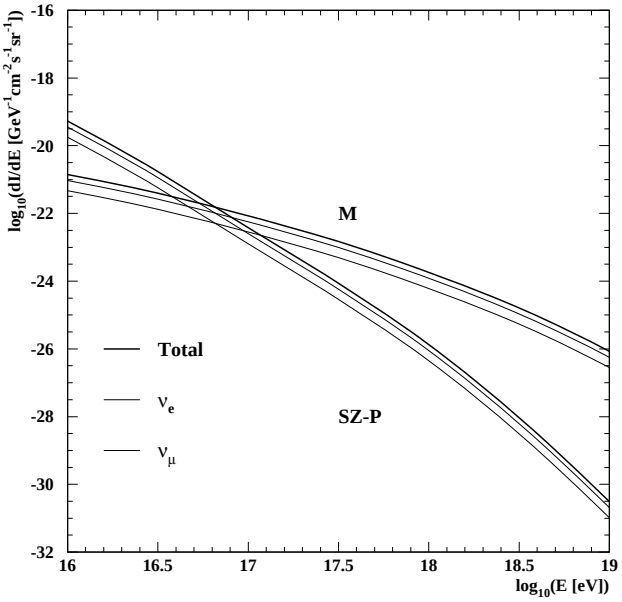

FIG. 4.28: Neutrino flux predictions in the EeV range as labeled in the text.

$$\sigma_{CC}(\nu N) = 5.5 \times 10^{-36}\mathrm{cm}^2 \left(\frac{E_\nu}{1\mathrm{GeV}}\right)^{0.363},$$

$$\sigma_{NC}(\nu N) = 2.3 \times 10^{-36}\mathrm{cm}^2 \left(\frac{E_\nu}{1\mathrm{GeV}}\right)^{0.363},$$

$$\sigma_{tot}(\nu N) = 7.8 \times 10^{-36}\mathrm{cm}^2 \left(\frac{E_\nu}{1\mathrm{GeV}}\right)^{0.363}.$$

Detailed discussions on physics and flux calculation of AGN neutrinos are in the previous section. Here we select two typical models for neutrino production in AGN as shown in Fig. 4.28. First model assumed chock acceleration in the AGN cores and predicted relatively flat fluxes up to energies of about 10^{15} eV. For our event rate calculation we select the prediction of [77], labeled SZ-P. There is however recent evidence that the GeV to TeV gamma ray emission observed from AGN corresponds to the blazar class. Most recent models for the proton blazars site the acceleration in the jets themselves. We use the prediction of [78], labeled M, which illustrates that the emitted neutrinos may extend well into the EeV region.

The simulation methods employed to evaluate the detector acceptance and performance for neutrino induced air showers are briefly described here. A ten-eye fluorescence system linearly arranged with 30km separation on a flat place at 1600m above see level which is same as that of Utah site is investigated. Each eye (or detector station) images the sky from an elevation angle of 3° up to that of 35° with 1.2° diameter pixels. Other detailed detector parameters are described in the previous section.

Each simulation for a given primary cosmic ray (electron neutrino, muon neutrino, or proton) was performed at fixed energy. The shower energy of neutrinos depends on the generation as described above. In the simulation we fix the energy transfer parameter y to be the average value $< y >= 0.2$, which is reasonable for $E_\nu > 10^{16} eV$. For each shower energy, the mean depth of proton shower maximum was determined from simulations [121]. For each primary particle at each energy, the mean of the interaction length $X_1$was determined from the above interaction cross sections of neutrinos with nucleons or that of protons, $83.1(E/\mathrm{GeV})^{-0.052}$ g/cm^2 [122]. The shower energy determines the shower size at maximum, N_{max} [86]. Given N_{max}, X_{max}, and X_1, the complete longitudinal profile was described by the Gaisser-Hillas function [113]. The NKG lateral distribution function [123, 124] normalized with the Gaisser parameterization has been used for the total number of electrons and positrons in hadronic (electromagnetic) cascade showers to determine the location where fluorescence lights are produced. We took into account the fluctuations of the first interaction depth, impact point, and directional angles of air shower cores with appropriate distributions but not air shower size fluctuations.

The light yield arriving at the detector site is calculated. Rayleigh and Mie scattering processes are simulated, with full account taken of the spectral characteristics of the light. The isotropically emitted fluorescence light, as well as direct and scattered Cherenkov light, is propagated. Night sky background noise is added to the signal. All processes that affect

to overall optical efficiency; mirror area and reflectivity, optical filter transmission, PMT quantum efficiency factors are folded with the light spectrum to give the photoelectron yield in each PMT, due to signal and noise.

A "fired" PMT is defined to require that its instantaneous photoelectron current is greater than the 2σ noise level of the night sky background. We preselected events if at least one of 10 eyes contains at least 10 firing PMTs. To ensure track quality, we cut events of which shower maximums are not viewed by any eye. Finally to reject proton background events, we selected only events with $X_{max} > 1300$ g/cm^2. We obtained the detector aperture corresponding the above selection cuts and calculated them into the acceptances multiplying the appropriate interaction length of neutrino with nucleon. The results are shown in Fig. 4.29 for both electron and muon neutrinos as a function of the primary energy.

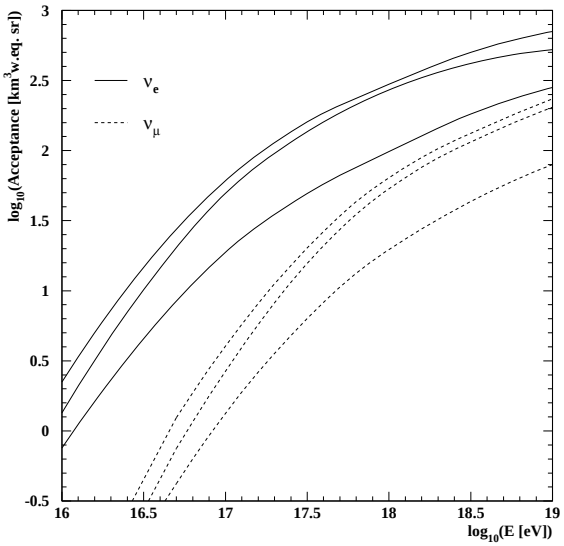

FIG. 4.29: Acceptance of the TA detector to neutrino induced air shower. Volume units are km^3 of water equivalent. The higher, middle, and lower curves corresponds to events after preselection, track quality, and proton rejection cuts.

We have estimated event rates for several energy threshold and selection cuts using a variety of models for the neutrino fluxes from proton AGN models which assume the proton acceleration region is at the core or the jets [77, 78].

The origins of the highest energy cosmic rays are not well understood, but cosmic rays should be accompanied by very high energy neutrinos in all models. The absolute normalization and energy dependence of the fluxes vary from model to model. The TA detector as a neutrino telescope ultimately will probe extraterrestrial accelerator sources using enough statistics of AGN neutrino events. Also we can distinguish between the assumptions for the location in AGN where protons could be accelerated well from the observed neutrino spectrum once we can detect neutrinos well with $E_\nu > 10^{16}$ eV.

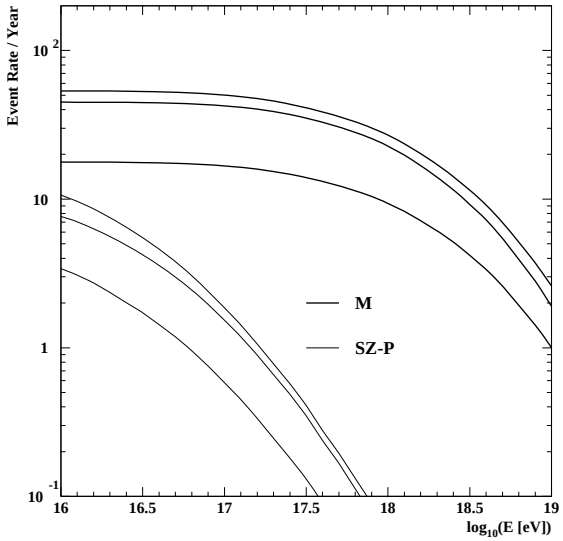

FIG. 4.30: Annual event rates as a function of the neutrino energies in the TA detector for neutrino induced air showers with fluxes from two different AGN models (see text). Three kinds of curves from each proton AGN model correspond to the required selections.

Table 4.6: Annual event rates in the TA detector for neutrino induced air showers with fluxes from two different AGN models (see text). Left and right side of slash(/) shows the numbers of events which survive the cuts from proton AGN-jet and AGN-core model respectively. The numbers of proton background events which survived all the cuts are also shown.

E_{th}(eV)	10 PMTs (S/N $\geq$ 2)	Viewing X_{max}	$X_{max} > 1300$g/cm^2	p background
10^{16}	53.5 / 10.7	44.9 / 7.6	17.8 / 3.4	310
10^{17}	50.1 / 1.9	42.4 / 2.4	16.7 / 0.6	17

Chapter 5

Collaboration

The Telescope Array will be built by the collaboration of Japanese, American and Australian physicists. The group consists of cosmic ray physicists who have been working in the AGASA and HiRes experiments, and high energy physicists who worked in large accelerator experiments in US and Japan.

Table 5.1: List of Telescope Array Collaborators.

Institute	Participants
ICRR, Inst. for Cosmic Ray Research, Univ. of Tokyo	T.Aoki, M.Fukushima, N.Hayashida, F.Ishikawa, H.Ohoka, M.Sasaki, M.Sasano, N.Takeda, M.Teshima, R.Torii, S.Yoshida
KEK, High Energy Accelerator Research Organization	Y.Arai, S.Kabe, T.Suwada
Kinki Univ.	M.Chikawa
Konan Univ.	F.Kajino, M.Sakata, Y.Yamamoto
Nagasaki Inst. of Applied Science	Y.Tanaka
Osaka City Univ.	S.Kawakami
Saitama Univ.	N.Inoue
Tokyo Inst. of Technology	F.Kakimoto, S.Ogio
Yamanashi Univ.	N.Kawasumi, K.Hashimoto, K.Honda
Columbia Univ.	J.Boyer, B.Knapp, E.Mannel, M.Semen, M.Shaevitz
Montana State Univ.	J.Beltz
Rutgers Univ.	G.Thomson
UCLA	K.Arisaka, D.Cline, W.Slater, A.Tripathi, T.Vinogradova
Univ. of New Mexico	B.D.Dieterle, G.Martin, J.A.J.Matthews, S.Riley, M.Roberts, T.Tessier
Univ. of Utah	Z.Cao, B.D.Kieda, E.C.Loh, J.N.Matthews, P.Sokolsky, W.Springer, L.Wiencke
Univ. of Adelaide	R.W.Clay, B.Dawson, N.Wild

Chapter 6

Cost and Schedule

The estimated total cost for the construction of Telescope Array is 8000 Million Japanese Yen or 75.5 M$ (see Tab.6.1). The Japanese group will contribute 80% of the total cost. The request of the construction budget was first submitted to Monbusho in April 1999. The US group plans to contribute to the rest of 20%. The request will be submitted to DOE and NSF and will be reviewed by the SAGENAP committee.

Table 6.1: Estimated Cost of Telescope Array.

item	cost (M Yen)	comments
Telescope	2370	mirror, frame, housing etc.
Imaging camera	2450	PMT, filter etc.
Electronics	2120	CSI, ADC, trigger, HVPS etc.
Data acquisition	230	inc. offline preprocessor
Atmosph. monitor	300	steerable laser, IR camera etc.
Infrastructure	530	site, road, elect., communication etc.
Total	8000	= 75.5 M$ (1 $ = 106 Yen)

We plan to test a complete set of telescope, electronics and atmospheric monitoring system in 2000 near the planned site. All the R/D efforts are targeted for the start of construction in the spring of 2001. It will take 4 years to build 10 stations.

References

[1] N. Hayashida *et al.*, Phys. Rev. Lett.**73**, 3491 (1994).

[2] D. J. Bird *et al.*, Astrophys.J. **441**, 144 (1995).

[3] S. Yoshida *et al.*, Astropart. Phys. **3**, 105 (1995).

[4] M. Takeda *et al.*, Phys. Rev. Lett. **81**, 1163 (1998).

[5] K. Greisen, Phys. Rev. Lett. **16**, 748 (1966); G. T. Zatsepin and V. A. Kuzmin, JETP Lett. **4**, 178 (1966).

[6] The Pierre Auger Observatory Design Report (compilation by S. Swardy).

[7] P. O. Lagage and C. J. Cesarsky, Astronomy and Astrophys. **118**, 223 (1983).

[8] D. B. Bird *et al.*, Phys. Rev. Lett. **71**, 3401 (1993).

[9] A. M. Hillas, in *Proceedings of the 12th International Cosmic Ray Conference, Hobart, Tasmania, Australia, 1971*, Vol. 3, p. 1001.

[10] H. Y. Dai *et al.*, J. Phys. G: Nucl. Phys. **14**, 793 (1988).

[11] M. Takeda *et al.*, Astrophys. J. **522**, 225 (1999).

[12] N. Hayashida *et al.*, in *Proceedings of the 26th International Cosmic Ray Conference, Salt Lake City, 1999*, Vol. 3, p. 256. *astro-ph/9906056.*; N. Hayashida *et al.*, Astrop. Phys. **10**, 303 (1999).

[13] T. Abu-Zayyad *et al.*, *astro-ph/9911144.*

[14] N. Hayashida *et al.*, J. Phys. G: Nucl. Part. Phys. **21**, 1101 (1995).

[15] B. R. Dawson, R. Meyhandan and K. M. Simpson, Astropart. Phys. **9**, 331 (1998).

[16] A. M. Hillas, Ann. Rev. Astron. Astrophys. **22**, 425 (1984).

[17] S. Yoshida and M. Teshima, Prog. Theor. Phys. **89**, 833 (1993).

[18] M. Simard-Normandin and P. P. Kronberg, Astrophys. J. **242**, 74 (1980).

[19] R. J. Rand, S. Kulkarni and J. J. Hester, Astrophys. J. (Lett) **352**, L1 (1990).

[20] R. J. Dettmar, Astronomy & Astrophysics **232**, L15 (1990).

[21] P. P. Kronberg, Rep. Prog. Phys. **57**, 325 (1994).

[22] L. Ferreti *et al.*, Astronomy & Astrophysics **302**, 680 (1994).

[23] E. Waxman, *astro-ph/9911395*.

[24] R. D. Blandford, *asto-ph/9906026*.

[25] P. L. Biermann, in *Proceedings of Workshop on Observing Giant Cosmic Ray Air Showers from* $\geq 10^{20} eV$ *Particles from Space, 1997*, edited by J. F. Kirzmanic, J. F. Ormes, and R. E. Streitmatter (AIP Conference Proc., 1997), **433**, p. 22.

[26] C. A. Norman, D. B. Melrose and A. Achterberg, Astophys. J. **454**, 60 (1995).

[27] F. C. Jones, in *Proceedings of Workshop on Observing Giant Cosmic Ray Air Showers from* $\geq 10^{20} eV$ *Particles from Space, 1997*, edited by J. F. Kirzmanic, J. F. Ormes, and R. E. Streitmatter (AIP Conference Proc., 1997), **433**, p. 37.

[28] C. Cesarsky and V. Ptsukin, in *Proceedings of the 23rd International Cosmic Ray Conference, Calgary, 1993*, Vol. 2, p. 341.

[29] A. V. Olinto, in *Proceedings of the 23rd International Cosmic Ray Conference, Salt Lake City, 1999*, Vol. 4, p. 361.; *astro-ph/9911154*.

[30] R. V. E. Lovelace, Nature **262**, 649 (1976).

[31] J. R. Jokipii and G. Morfill, Astrophys. J. **312**, 170 (1987).

[32] T. Totani, Astropart. Phys. **11**, 451 (1999).

[33] P. Bhattacharjee, C. T. Hill, and D. N. Schramm, Phys. Rev. Lett. **69**, 567 (1992).

[34] G. Sigl, D. N. Schramm, and P. Bhattacharjee, Astropart. Phys. **2**, 401 (1994).

[35] G. Sigl, D. N. Schramm, and P.Bhattacharjee, Science **270**, 1977 (1995).

[36] G. Sigl, S. Lee, D. N. Schramm, and P. S. Coppi, Phys. Lett. B **392**, 129 (1997).

[37] V. Berezinsky, P. Blasi, and A. Vilenkin, Phys. Rev. D **58**, 103515 (1998).

[38] G. Sigl, S. Lee, P. Bhattacharjee, and S. Yoshida, Phys. Rev. D **59**, 043504 (1999).

[39] C. T. Hill, Nucl. Phys. B **224**, 469 (1983).

[40] V. Berezinsky, M. Kachelriess, and A. Vilenkin, Phys. Rev. Lett. **79**, 4302 (1997).

[41] V. Kuzmin and I. Tkachev, Phys. Rev. D **59**, 123006 (1999).

[42] D. J. H. Chung, E. W. Kolb and A. Riotto, Phys. Rev. Lett. **81**, 4048 (1998).

[43] K. Hamaguchi, Y. Nomura and T. Yanagida, Phys. Rev. D **58**, 103503 (1998).

[44] S. Yoshida, G. Sigl, and S. Lee, Phys. Rev. Lett. **81**, 5505 (1998).

[45] T. J. Weiler, Astropart. Phys. **11**, 303 (1999).

[46] D. J. H. Chung, G. Farrar, E. Kolb, Phys. Rev. D **57**, 4606 (1998); G. Farrar, in *Proceedings of Workshop on Observing Giant Cosmic Ray Air Showers from* $\geq 10^{20} eV$ *Particles from Space, 1997*, edited by J. F. Kirzmanic, J. F. Ormes, and R. E. Streitmatter (AIP Conference Proc., 1997), **433**, p. 226.

[47] S. Coleman and S. L. Glashow, Phys. Rev. D **59**, 116008 (1999).

[48] D. Fargion, B. Mele, and A. Salis, Astrophys. J. **517**, 725 (1999).

[49] V. A. Kuzmin, and V. A. Rubakov, Phys. Atom. Nucl. **61**, 1028 (1998).

[50] C. T. Hill and D. N. Schramm, Phys. Rev. D **31**, 564 (1985).

[51] T. J. Weiler, Phys. Rev. Lett. **49**, 234 (1982); Astrophys. J. **285**, 495 (1984); E. Roulet, Phys. Rev. D **47**, 5247 (1993).

[52] S. Yoshida, Astropart. Phys. **2**, 187 (1994).

[53] S. Yoshida, H. Dai, C. C. H. Jui, and P. Sommers, Astrophys. J. **479**, 547 (1997).

[54] S. Lee, Phys. Rev. D **58**, 043004 (1998).

[55] M. A. Lawrence, R. J. O. Reid, and A. A. Watson, J. Phys. G: Nucl. Part. Phys **17**, 733 (1991).

[56] W. Rhode *et al.*, Astropart. Phys. **4**, 217 (1996).

[57] R. M. Baltrusaitis *et al.*, Phys. Rev. D **31**, 2192 (1985).

[58] K. S. Capelle, J. W. Cronin, G. Parente, and E. Zas, Astropart. Phys. **8**, 321 (1998).

[59] J. F. Ormes *et al.*, in *Proceedings of the 25th International Cosmic Ray Conference, Durban, 1997*, Vol. 5, P. 273.

[60] M. Jang and H. R. Miller, Astrophys. J. **452**, 582 (1995).

[61] C. M. Urry and P. Padovani, Pub. Astr. Soc. Pacif. **107**, 803 (1995).

[62] R. C. Hartman *et al.*, Astrophys. J. Suppl. **123**, 79 (1999).

[63] J. R. Mattox *et al.*, Astrophys. J. **xxx**, xxx (1997).

[64] R. Mukherjee and J. Chiang, *astro-ph/9902003*.

[65] J. Chiang and R. Mukherjee, Astrophys. J. **496**, 752 (1998).

[66] M. Catanese, Astrophys. J. **501**, 616 (1998).

[67] M. Punch *et al.*, Nature **358**, 477 (1992).

[68] J. Quinn *et al.*, Astrophys. J. **456**, L83 (1995).

[69] Schubnell *et al.*, *astro-ph/9602068*.

[70] M. J. Rees, Nature **211**, 468 (1966).

[71] M. Sikora, M. C. Begelman, and M. J. Rees, Astrophys. J. Lett. **421**, 153 (1994).

[72] R. J. Protheroe, *astro-ph/9612213*.

[73] K. Mannheim *et al.*, *astro-ph/9605107*.

[74] R. J. Protheroe, ADP-AT-96-4.

[75] T. K. Gaisser, F. Halzen, and T. Stanev, Phys. Reports **258**, 173 (1995).

[76] F. W. Stecker and M. H. Salamon, *astro-ph/9501064*.

[77] A. P. Szabo and R. J. Protheroe, in *Proceedings of High Energy Neutrino Astrophysics Workshop, U.Hawaii, March 1992*, edited by V. J. Stenger, J. L. Learned, S. Pakvasa, and X. Tata, (World Scienctific, 1993), p. 24.

[78] K. Mannheim, Astropart. Phys. **3**, 295 (1995).

[79] F. Halzen and E. Zas, MADPH-97-982; *astro-ph/9702193*.

[80] P. Lipari, Astropart. Phys. **1**, 195 (1993).

[81] L. Wiencke and S. Yoshida, *TA Internal Report*, TA-97-008 (1997).

[82] M. Kobayashi *et al.*, Nucl. Inst. Meth. A **337**, 355 (1992).

[83] M. V. Korzhik *et al.*, Nucl. Inst. Meth. B **B72**, 499 (1992).

[84] S. Baccaro *et al.*, Nucl. Inst. Meth. A **361**, 209 (1995).

[85] N. Tsuchida *et al.*, Nucl. Inst. Meth. A **385**, 290 (1997).

[86] R. M. Baltrisaitis *et al.*, Nucl. Instr. and Meth. A **240**, 410 (1985).

[87] J. Boyer *et al.*, in *Proceedings of the 24th International Cosmic Ray Conference, , 1995*, Vol. 3, p. 429.

[88] CASCADE (1996).

[89] S. Wotton, in Proceedings of CHEP-92, Annecy, France, 1992.

[90] F. Kakimoto *et al.*, Nuclear Instruments and Methods, A **373**, 572 (1996).

[91] R. Gray *et al.*, in *Proceedings of the 26th International Cosmic Ray Conference, Salt Lake City, 1999*, Vol. 5, p. 353.

[92] M. Chikawa *et al.*, in *Proceedings of the 26th International Cosmic Ray Conference, Salt Lake City, 1999*, Vol. 5, p. 404.

[93] G. Martin and J. A. J. Matthews, Pierre Auger Note 99-037 / HiRes Note 10-11-1999 (1999) available at http://www-hep.phys.unm.edu/∼johnm

[94] F. X. Kneiays *et al.*, *Users Guide to Lowtran 7*, Air Force Geophysics Laboratory, AFGL-TR-88-0177, (also see http://www-vsbm.plh.af.mil/soft/modtran.html).

[95] D. R. Longtin, *A Wind Dependent Desert Aerosol Model: Radiative Properties*, Air Force Geophysical Laboratory, AFGL-TR-88-0112, (1988).

[96] Ontar Corporation North Andover MA 01845-2000 USA, www.ontar.com.

[97] L. Wiencke *et al.*, Nucl. Instr. Meth. A **428**, 593 (1999).

[98] L. Wiencke *et al.*, in *Ultraviolet Atmospheric and Space Remote Sensing: Methods and Instrumentation*, edited by R. Huffman and K Dymond, Proc SPIE **3818**, 59 (1999).

[99] N. Hayashida *et al.*, in *Proceedings of the 26th International Cosmic Ray Conference, Salt Lake City, 1999*, Vol. 5, p. 357.

[100] DFM Enginnering Inc., Longmont CO USA. (www.sni.net/ dfm42/)

[101] Big Sky Lasers Inc. Bozeman MT USA. (www.bigskylasers.com)

[102] R. Ghandi, C. Quigg, M. H. Reno, and I. Sarcevic, Astropart. Phys. **5**, 81 (1996); Phys. Rev. D **58**, 093009 (1998).

[103] B. L. Emerson, Ph.D Thesis, University of Utah (unpublished) (1992).

[104] L. D. Landau and I. J. Pomeranchuk, Dokl. Akad. Nauk. SSSR **92**, 535 (1953).

[105] A. B. Migdal, Phys. Rev. **103**, 1811 (1956).

[106] B. McBreen and C. J. Lambert, Phys. Rev. D **24**, 2536 (1981).

[107] T. Stanev, and H. P. Vankov, Phys. Rev. D **55**, 1365 (1997).

[108] S. J. Sciutto, GAP97-029 (1997).

[109] T. Erber, Rev. Mod. Phys. **38**, 626 (1966).

[110] V. H. Bayer, B. M. Katkov, and V. S. Fadin, in *Radiation of relativistic electrons* (Moscow, Atomizdat, 1973).

[111] V. Anguelov and H. Vankov. *No Identification*

[112] R. Gandihi, C. Quigg, M. H. Reno, and I. Sarcevic, Astropart. Phys. **5** 81 (1995).

[113] T. K. Gaisser and A. M. Hillas, in *Proceedings of the 15th International Cosmic Ray Conference, Plovdiv, Bulgaria, 1977*, Vol. 7, p. 353.

[114] R. Gandihi, C. Quigg, M. H. Reno, and I. Sarcevic, Phys. Rev. D **58**, 093009 (1998).

[115] CTEQ Collaboration, H. L. Lai *et al.*, Phys. Rev. D **55** 1280 (1997).

[116] C. Quigg, "Neutrino Interaction Cross Sections", FERMILAB-CONF-97/158-T.

[117] NMC, M. Arneodo *et al.*, Phys. Lett. B **36** 471 (1995).

[118] H1 Collaboration, S. Aid *et al.*, Nucl. Phys. B **439** 471 (1995); Nucl. Phys. B **470** 3 (1996).

[119] ZEUS Collboration, M. Derrick *et al.*, Z. Phys. C **65** 379 (1995).

[120] E665 Collaboration, M. R. Adams *et al.*, Phys. Rev. D **54**, 3006 (1996).

[121] T. K. Gaisser *et al.*, Phys. Rev. D **47**, 1919 (1993).

[122] M. Honda *et al.*, Phys. Rev. Lett., **70**, 525 (1993).

[123] K. Kamata and J. Nishimura, Prog. Theor. Phys. Suppl. **6**, 93 (1958).

[124] K. Greisen, Prog. Cosmic Ray Physics **3**, 1 (1956).